8-2016

Effects of Mean Shear and Scalar Initial Length Scale on Three-Scalar Mixing in Turbulent Coaxial Jets

Wei Li
Clemson University

Effects of mean shear and scalar initial length scale on three-scalar mixing in turbulent coaxial jets

---

A Dissertation
Presented to
the Graduate School of
Clemson University

In Partial Fulfillment
of the Requirements for the Degree
Doctor of Philosophy
Mechanical Engineering

---

by
Wei Li
Aug 2016

Accepted by:
Dr. Chenning Tong, Committee Chair
Dr. Richard Miller
Dr. Jay Ochterbeck
Dr. Xiangchun Xuan

Abstract

The effects of the velocity and length scale ratios of the annular flow to the center jet on three-scalar mixing in turbulent coaxial jets are investigated. In this flow a center jet and an annular flow, consisting of acetone-doped air and ethylene respectively, are mixed with the co-flow air. Simultaneous planar laser-induced fluorescence and Rayleigh scattering are employed to measure the mass fractions of the acetone-doped air and ethylene. The velocity ratio alters the relative mean shear rates in the mixing layers between the center jet and the annular flow and between the annular flow and the co-flow, modifying the scalar fields through mean-flow advection, turbulent transport, and small-scale mixing. The length scale ratio determines the degree of separation between the center jet and the co-flow. The results show that while varying the velocity ratio can alter the mixing characteristics qualitatively, varying the annulus width only has quantitative effects. Increasing the velocity ratio and the annulus width always delays the evolution of the scalar fields. The evolution of the mean scalar profiles are dominated by the mean-flow advection, while the shape of the joint probability density function (JPDF) is largely determined by the turbulent transport and molecular diffusion. The JPDF for the higher velocity ratio cases is bimodal at some locations while it is unimodal for the lower velocity ratio cases. The diffusion velocity streamlines in scalar space representing the conditional diffusion generally converge quickly to a manifold along which they continue at a lower

rate. The curvature of the manifold is significantly larger for the higher velocity ratio cases. Predicting the mixing path along the manifold as well as its dependence on the velocity and length scale ratios presents a challenging test for mixing models.

The three-scalar subgrid-scale (SGS) mixing in the context of large eddy simulation and its dependence on the velocity and length scale ratios are also investigated. The analysis reveals two SGS mixing regimes depending on the SGS variance value of the center jet scalar. For small SGS variance the scalars are well mixed with unimodal filtered joint density function (FJDF) and the three-scalar mixing configuration is lost. For large SGS variance, the scalars are highly segregated with bimodal FJDFs at radial locations near the peak of the mean SGS variance of the center jet scalar. Two competing factors, the SGS variance and the scalar length scale, are important for the bimodal FJDF. For the higher velocity ratio cases, the peak value of the SGS variance is higher, thereby resulting in stronger bimodality. For the lower velocity ratio cases, the wider mean SGS variance profiles and the smaller scalar length scale cause bimodal FJDFs over a wider range of physical locations. The diffusion streamlines first converge to a manifold and continue on it toward a stagnation point. The curvature of the diffusion manifold is larger for the larger velocity ratio cases. The manifold provides a SGS mixing path for the center jet scalar and the co-flow air, and thus the three-scalar mixing configuration characteristics is maintained for the large SGS variance. The SGS mixing characteristics observed present a challenging test for SGS mixing models. The scalar dissipation rate structures have similarities to those of mixture fraction and temperature in turbulent nonpremixed/partially premixed flames. The results in the present work, therefore, also provide a basis for investigating multiscalar SGS mixing in turbulent reactive flows.

Dedication

To my Mom

Acknowledgments

I would first like to thank my advisor, Prof. Chenning Tong, for the guidance and financial support for the past seven years. I would also want to thank the other committee members, Dr. Richard Miller, Dr. Jay Ochterbeck and Dr. Xiangchun Xuan for your comments and suggestions. A special thanks to Dr. Campbell Carter of Air Force Research Laboratory for lots of suggestions on the experimental setup and loaning the equipments, and Mengyuan Yuan for the assistance in running the experiments. Thanks also to Dr. Jian Cai for lots of help in my first year, and to Dr. Shuaishuai Liu and Dr. Khuong Nguyen for the valuable discussions.

Table of Contents

List of Tables

List of Figures

Chapter 1

Introduction

Fossil fuels has been the major energy source for human beings for transportation and power generation for a long time, and this fact is not going to change in the foreseeable future [27]. Combustion is a fast and also an efficient way to extract energy from fossil fuels. It is usually turbulent combustion rather than laminar flame taking place in engineering applications such as power plant, gas turbine, internal combustion engine and furnace. There are two reasons for turbulent combustion, one is that the mixing between fuel and oxidizer is orders of magnitude faster, resulting in quicker heat release so that combustion devices can achieve high power density; another reason is the flow instability generated by heat release can induce large gas expansion, which induce a laminar flow transition into turbulent flow [40].

In applications such as diesel engine, fuel and oxidizer usually are introduced into the combustion chamber separately [40]. Combustion starts at the premixed fraction of the gas (flammable) that is prepared when diesel spray entrain air, then it is non-premixed (diffusion) flame ensued. Turbulent mixing plays an important role in non-premixed flame, the combustion rate of which is controlled by the mixing between the fuel and the oxidizer at reaction zone. Heat and radicals generated by

chemical reactions also needs to mix with unreacted mixtures and extinction would occur when there are large thermal runaway (heat loss). Turbulence-chemistry interaction, such as ignition and extinction, is one of the biggest challenges in turbulent combustion research. More knowledge about turbulence-chemistry interaction are needed as Reynolds number keep increasing in practical combustion devices. Investigation of turbulent mixing is important for the understanding of turbulence-chemistry interaction.

Mixing terms such as dissipation rate and diffusion are important in advanced numerical simulation methods of turbulent combustion. Laminar flamelet method treat turbulent flame as stretched laminar flame, and the flame structure is determined by two parameters: the mixture fraction and its dissipation rate [39, 40]. The flamelet equation for nonpremixed combustion is parameterized by mixture fraction dissipation rate, the functional dependence of which on mixture fraction is needed. The dependence of conditional scalar dissipation on scalar are very complex even in homogeneous flow fields [15, 17, 23, 24, 35, 36]. There are attempts to find the relation between conditional dissipation and the scalar probability density function (PDF) (e.g. [35, 36, 43, 52, 53, 57]). In inhomogeneous flow field, the dependence are different for different flow configurations and vary with physical locations (e.g. [26, 33, 65]). Chemical reaction (source term) is been treated exactly in the PDF method, however, conditional diffusion show up as a unclosed term and mixing models are needed. In homogeneous scalar field, the conditional scalar diffusion is linearly dependent on scalar [22, 28, 35, 37, 52, 75]. The dependence becomes a little complex, approximately linear or piecewise linear, in inhomogeneous flow field [26, 65].

Binary (two-scalar) mixing has been extensively investigated due to its simplicity and its applications in pollutant dispersions. Basic statistics such as the scalar mean, the scalar root-mean-square or variance, scalar dissipation rate and

scalar dissipation time scale has been studied in different flow configurations (e.g. [1, 15, 24, 31, 37, 59, 74]). The scalar probability density function has also been studied in a lot of previous works (e.g. [15, 65]). Different shapes of PDF, including bimodal, quasi-Gaussian and exponential tails has been found for passive scalars. Three mixing regimes has been identified for a single scalar dispersion in isotropic turbulence: molecular diffusion dominates at small times; turbulent convection dominates at intermediate times; turbulent diffusion dominates at very large times [45, 73].

However, scalar mixing in turbulent non-premixed flame is a multiscalar mixing problem, and studies on multiscalar mixing are very limited. As the simplest case of multiscalar mixing, three scalar mixing has been investigated in a few studies (e.g. [25, 58, 65, 72, 73]). The correlation coefficient of two scalars (thermal fluctuations), which are generated by two mandolines that are placed at different downstream locations of a grid turbulence, was found to decay going downstream [72]. Sirivat et al [58] found that the decay rate of correlation coefficient dependent on the downstream locations at which the scalars been introduced into the grid turbulence. The decay rate become much slower when scalars are introduced very close to the grid. The evolution of correlation coefficient become different for different scalar separation distance [73]. The correlation coefficient of two scalars that were introduced into a jet is similar to that in grid turbulence [65]. There are also studies on the evolution of the joint probability density function (JPDF) and the conditional diffusion of three-scalar mixing in isotropic homogenous turbulence through direct numerical simulation (DNS) [25]. In order to mimic flow configuration of Sandia flames, Cha et al investigated a double scalar mixing layer problem with DNS [10].

The initial arrangement of scalars in physical space is important for three-scalar mixing. There were three scalar mixing studies have two scalars issued into a background scalar (air) (e.g. [58, 65, 73]). The three scalars were symmetrical in

scalar space and have direct contact with each other in physical space in the DNS simulation of Juneja and Pope [25], thus the JPDF at the initial stage of mixing was essentially three mixing lines that connecting the three scalars in the scalar space. The double scalar mixing layer problem investigated by Cha et al [10] mimic the flow configuration of Sandia flame very well, however, it does not represent good enough the mixing scenarios in turbulent partially premixed flame because its pilot is essentially the same scalar as the center stream only with a different initial value. To understand better the multiscalar mixing processes in turbulent nonpremixed reactive flows, Cai et al [6] studied three-scalar mixing in a coaxial jet emanating into co-flow air. In this flow the scalar from the center jet (ϕ_1) and the co-flow air (ϕ_3) at the jet exit plane are separated by the scalar from the annulus (ϕ_2). As a result, initially there is direct mixing between ϕ_1 and ϕ_2 and between ϕ_2 and ϕ_3, but not between ϕ_1 and ϕ_3. Mixing between ϕ_1 and ϕ_3 must involve ϕ_2. This mixing configuration better represents the mixing process in turbulent non-premixed reactive flows where mixing between reactants generally must involve the product.

Cai et al [6] analyzed in detail the mixing process in the near field of the flow. In addition to the scalar means, the root-mean-square (rms) fluctuations, the correlation coefficient, the segregation parameter, the mean scalar dissipation and the mean cross-dissipation. They also investigated the scalar JPDF and the mixing terms in the JPDF transport equation: the conditional diffusion, conditional dissipation, and conditional cross-dissipation, which are important for PDF methods for modeling reactive flows. The results show that the diffusion velocity streamlines in scalar space representing the conditional diffusion generally converge quickly to a manifold, along which they continue at a lower rate. While the three scalars in this flow initially have similar distances in scalar space, mixing between two of the scalars can occur only through the third, forcing a detour of the manifold (mixing path) in scalar space.

This mixing path presents a challenging test for mixing models since most mixing models use only scalar-space variables and do not take into account spatial (physical-space) scalar structures. In addition, the approach to the manifold is generally in the direction of ϕ_2. The difference in the magnitudes of the diffusion velocity components for the two scalars cannot be accounted for by the difference in their dissipation time scales. The mixing process during the approach to the manifold, therefore, cannot be modelled by using different dissipation time scales alone.

The three-scalar mixing in the coaxial jet has been simulated with hybrid LES/FMDF by Shetty et al [56]. While the mean profiles were in good agreement with the experimental data, they failed to capture some key features of the rms profiles such as the two off-centerline peaks of the ϕ_2 rms profile. Rowinski & Pope [50] used both RANS-PDF and LES-PDF to simulate this three-scalar mixing problem. While the basic statistics such as mean and rms show excellent agreement with the measurements, different mixing models show their limitations in capturing some of the key features such as the bimodal JPDF and the diffusion manifold.

While Cai et al [6] revealed important characteristics of the three-scalar mixing process, the velocity ratio between the annular flow and the center jet was fixed (close to unity). So was the geometry of the coaxial jet. The velocity ratio determines the relative magnitudes of the velocity differences (shear strength) between the center jet and the annular flow and between the annular flow and the co-flow, and therefore is an important parameter governing the mixing process. Its influence on the mixing process can also help understanding the effects of the stoichiometric mixture fraction on the mixing process in turbulent non-premixed flames. Since ϕ_2 is analogous to a combustion product in a flame, which generally has the maximum mass fraction near the stoichiometric mixture fraction, varying the velocity ratio is, as far as mixing is concerned, analogous to shifting the location of the product (the stoichiometric

mixture fraction) relative to the velocity profile (shear layer). Present study will investigate the effects of the velocity ratio on the three-scalar mixing process.

The ratio between the annulus width and the center jet diameter also has important effects on the mixing process. The velocity and scalar length scales depend on the sizes of the center jet and the width of the annulus. The dependence of the mixing process on the ratio of the length scale is also useful for understanding the effects of the reaction zone width on the mixing process in flames. Due to the similar role in mixing played by ϕ_2 to that by a combustion product (or the temperature), the width of the peak ϕ_2 region in the three-scalar mixing is analogous to the reaction zone width in a non-premixed flame. Varying the width of the annulus (degree of separation between ϕ_1 and ϕ_3) will alter the shape of of the JPDF at the peak ϕ_2 region in the scalar space. Investigating the effects of the length-scale ratio, therefore, is also important for understanding the influence of the reaction zone width on multiscalar mixing in flames.

Present study would investigate experimentally the effects of the velocity ratio (mean shear) and the length scale ratio between the annular flow and the center jet on the three-scalar mixing process. The dependence of the important scalar statistics characterizing the mixing on these ratios will be analyzed. These include the mean, the rms fluctuations, the correlation coefficient, the segregation parameters, the scalar JPDF, and the mixing terms in the JPDF transport equation. The transport equation for the scalar JPDF, f, is [41]

$$\begin{aligned}\frac{\partial f}{\partial t}+\frac{\partial}{\partial x_i}\left[f(U_i+\langle u_i|\,\hat{\phi}_1,\hat{\phi}_2\rangle)\right] &= -\frac{\partial}{\partial \hat{\phi}_1}\left[f\,\langle D_1\nabla^2\phi_1|\,\hat{\phi}_1,\hat{\phi}_2\rangle\right]-\frac{\partial}{\partial \hat{\phi}_2}\left[f\,\langle D_2\nabla^2\phi_2|\,\hat{\phi}_1,\hat{\phi}_2\rangle\right]\\ &= (D_1+D_2)\nabla^2 f-\frac{1}{2}\frac{\partial^2}{\partial \hat{\phi}_1^2}\left[f\,\langle\chi_1|\,\hat{\phi}_1,\hat{\phi}_2\rangle\right]-\frac{1}{2}\frac{\partial^2}{\partial \hat{\phi}_2^2}\left[f\,\langle\chi_2|\,\hat{\phi}_1,\hat{\phi}_2\rangle\right]-\frac{\partial^2}{\partial \hat{\phi}_1\partial \hat{\phi}_2}\left[f\,\langle\chi_{12}|\,\hat{\phi}_1,\hat{\phi}_2\rangle\right], \qquad (1.1)\end{aligned}$$

where U_i, u_i are the mean and fluctuating velocities respectively. The diffusion

coefficients for ϕ_1 and ϕ_2, D_1 and D_2, have values of 0.1039 cm^2/s and 0.1469 cm^2/s, respectively [49]. The left-hand side (LHS) of the equation is the time rate of change of the JPDF and the transport of the JPDF in physical space by the mean velocity and the conditional mean of the fluctuating velocity. The right-hand side (RHS) gives two forms of the mixing terms. The first involves the conditional scalar diffusion, $\langle D_1 \nabla^2 \phi_1 | \hat{\phi}_1, \hat{\phi}_2 \rangle$ and $\langle D_2 \nabla^2 \phi_2 | \hat{\phi}_1, \hat{\phi}_2 \rangle$, whereas the second involves the conditional scalar dissipation, $\langle \chi | \hat{\phi}_1, \hat{\phi}_2 \rangle = \langle 2D \frac{\partial \phi}{\partial x_i} \frac{\partial \phi}{\partial x_i} | \hat{\phi}_1, \hat{\phi}_2 \rangle$, and the conditional scalar cross-dissipation, $\langle \chi_{12} | \hat{\phi}_1, \hat{\phi}_2 \rangle = \langle (D_1 + D_2) \frac{\partial \phi_1}{\partial x_i} \frac{\partial \phi_2}{\partial x_i} | \hat{\phi}_1, \hat{\phi}_2 \rangle$, respectively, where the angle brackets denote an ensemble average. For convenience the sample space variable, $\hat{\phi}$, are omitted hereafter. While transport by the mean and conditional velocities are essentially the mean-flow advection and the turbulent convection of the JPDF in physical space, respectively, the mixing terms transport the JPDF in scalar space, and represent the effects of molecular mixing on the evolution of the scalar JPDF.

The three-scalar subgrid-scale (SGS) mixing in the context of large eddy simulation (LES) of turbulent velocity and scalar fields would also be studied. In LES the resolvable-scale velocity and scalar are computed while the effects of the subgrid scales, such as the SGS stress and the SGS scalar fluxes, are modeled. In LES of turbulent reactive flows, the (joint) distribution of SGS scalars, i.e., the scalar filtered joint density function (FJDF), is also needed in order to obtain the filtered reaction rates because of their nonlinear dependencies on the scalars. LES based on the filtered density function method has become a very promising approach [12, 18, 21, 48, 54, 55, 56]. Much improvement in its capability to predict three-scalar mixing, however, is still needed [56]. Because the evolution of the FJDF depends strongly on the small-scale SGS mixing process, investigation of multiscalar SGS mixing is of importance.

Previous works ([8, 47, 63, 67, 68, 69]) have studied the SGS (binary) mixing of mixture fraction in turbulent jets and turbulent partially premixed flames. The

filtered density function (FDF) of mixture fraction (a conserved scalar) in the jets and the filtered mass density function (FMDF) in the flames were analyzed using their means conditioned on the resolvable-scale scalar and the SGS scalar variance. The results show that the SGS scalar mixing has two limiting regimes. For instantaneous SGS variance values small compared to its mean, the conditional FDF is close to Gaussian. The conditionally filtered scalar dissipation depends weakly on the SGS scalar, suggesting that the SGS scalar is well mixed. The SGS scalar time scale is small and the SGS mechanical-to-scalar time scale ratio is large. For large values of the SGS variance the conditional FDF becomes bimodal. The conditionally filtered scalar dissipation is bell-shaped, indicating a strong dependence on the SGS scalar. These results suggest that on average the scalar within a grid cell consists of portions of well-mixed fluid that carry two distinct scalar values, and are separated by a sharp interface (cliff). The SGS scalar time scale is large and the SGS mechanical-to-scalar time scale ratio is small. The bimodal conditional FDF is similar to the PDF in early stages of initially binary mixing, but is in contrast with PDFs in fully developed flows, which are generally unimodal. It is also found that the SGS scalar with very large variance (more than ten times its mean value) almost always contain the ramp-cliff structure, which is associated with large-scale velocity structures, while the SGS scalar with moderate variance can contain ramp-cliffs and other diffusion-layer-like structures. The results for the FMDF in turbulent flames also show similar trends [69]. These results are important for utilizing the resolvable scale variables in modeling the FDF/FMDF. The qualitatively different SGS mixing fields in the two limiting regimes also have strong implications for studying multiscalar SGS mixing.

The rest of the dissertation is organized as follows. Chapter 2 describes the experimental setup and the data reduction procedures. Chapter 3 provides an estimate of the measurement resolution of scalar dissipation rates for the Rayleigh scattering

and acetone LIF techniques. The effects of the mean shear and the scalar initial length scale on three-scalar mixing in the context of RANS are shown in Chapter 4, while the three-scalar SGS mixing in the context of LES and also its dependence on the mean shear and the scalar initial length scale are shown in Chapter 5. Then conclusions follows in Chapter 6.

Chapter 2

Experimental facilities and data reduction procedures

2.1 Experimental methodology

Simultaneous planar laser induced fluorescence (LIF) of acetone and planar laser Rayleigh scattering are employed to measure the mass fractions of the center stream and the annular stream in coaxial jets in this work. Both LIF and Rayleigh scattering are well established techniques for scalar measurments in both cold flows and reactive flows. Only a brief introduction of the theory and issues related to the measurement in this work are given here, further detail about the theory and their applications can be found in [13, 14, 32, 34].

2.1.1 Acetone laser induced fluorescence

Molecules (atoms) are resonantly stimulated by laser radiation in LIF, thus the laser wavelength is corresponding to a specific absorption line of the molecules (atoms) and LIF is a species selective technique [13, 14]. The molecules are stimulated

from the ground state to an excited electric-vibrational state after the absorption of a photon. Usually the excited state is unstable and will transfer to a lower vibrational state immediately through vibrational relaxation, then a photon will be emitted when the lower vibrational level state molecule goes back to the ground state. The emitted light usually has a smaller photon energy than the laser source, or the wavelength of the LIF emission is larger than the laser wavelength. The spontaneous emission from the excited state can be observed at 90 degrees to the collimated laser sheet.

After evaluating a few candidates, Lozano [30] consider acetone as an excellent tracer for scalar measurements in turbulent flows. Thurber [62] summarized the advantages of acetone LIF including:

(1) High vapor pressure (over 30% by volume at room temperature) and can be easily seeded into gaseous flow by bubbling the gas through liquid acetone containers.

(2) Large absorption cross section: $\sigma_{abs} = 4.2 \times 10^{-20}\ cm^2$ at the laser wavelength (266 nm) used in this work.

(3) Broadband absorption spectrum (extends from 225 nm to 320 nm) and easily accessible from commercially available high energy pulse lasers.

(4) Visible fluorescence emission (between 350 nm and 550 nm), at which range CCD cameras usually have very high quantum efficiency.

(5) Short lifetime of the excited state so that acetone LIF a spontaneous technique that can "freeze" high speed flows.

(6) Large quantum yield to achieve higher signal-to-noise ratio (SNR).

(7) Linearity of the LIF signal, which is linearly proportional to the acetone concentration and the laser intensity when the laser energy is not extremely high.

2.1.2 Laser rayleigh scattering

Rayleigh scattering is the elastic scattering of light from molecules [14]. The Rayleigh scattering signal is linearly proportional to the number density of molecules, the laser intensity and the Rayleigh scattering cross section (σ) of the molecule. Rayleigh scattering cross section is a physical property of the molecule. Rayleigh scattering is not a species selective technique because the wavelength of the laser source does not have to be tuned to a absorption line of the molecules like that in LIF, or arbitrary laser wavelength can be used. However, shorter wavelengths are usually preferred due to the λ^{-4} dependence of the Rayleigh cross section, $\sigma \propto \lambda^{-4}$, where λ is the light wavelength. Another difference between Rayleigh scattering and LIF is the wavelength of the scattering light is the same as the laser source whereas the fluorescence wavelength is usually larger than the laser wavelength in LIF. All molecules in the probe volume would scattering at the same wavelength, although they are different in the signal intensity due to different Rayleigh cross sections. Application of Rayleigh scattering in reactive flow for temperature or density measurements are limited, because too many species show up and information about the local composition is required to obtain temperature or density. It would be possible to measure temperature only when the fuel mixture is carefully selected to make the variation of the effective Rayleigh cross section (σ_{eff}) across the scalar space small (even negligible). The variation of the ratio between the effective Rayleigh cross section (σ_{eff}) and molecular weight needs to be negligible in order to measure density [32].

Three molecules are involved in Rayleigh scattering in this work: air, acetone and ethylene. Ethylene is chosen because of its high Rayleigh cross section, $\frac{\sigma_{Eth}}{\sigma_{Air}} = 7$ (measured in the present work), and its density is close to that of air so that buoyancy

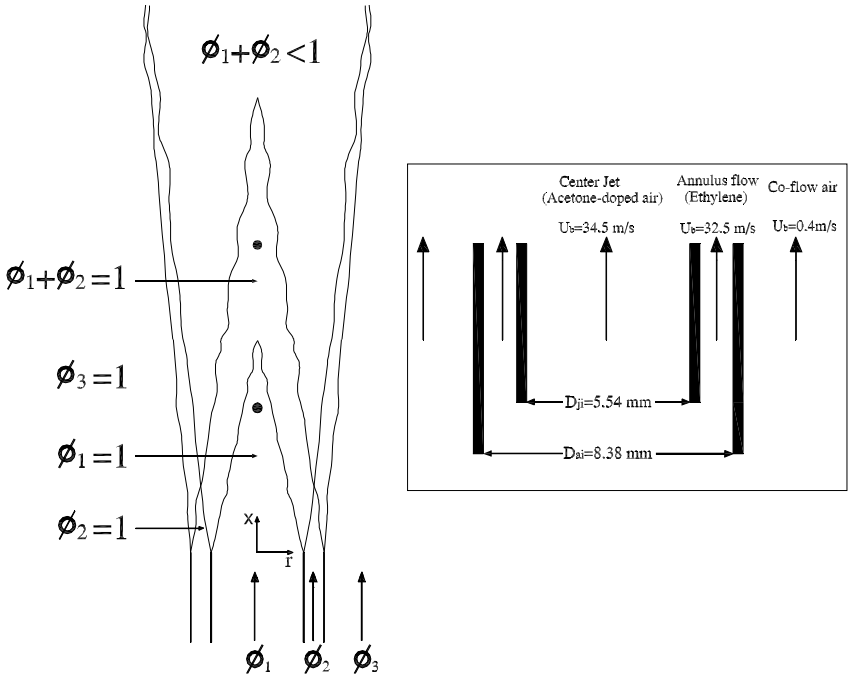

Figure 2.1: Schematic of the coaxial jet for Case I [6]. The dimensions of jet tubes and the bulk velocities for other cases are listed in Table 2.1 and 2.2. The two solid circles represent the approximate downstream locations that the cross-stream results are shown in the following Chapters.

does not play a role in the flow. The ratio of the Rayleigh cross section of acetone vapor and that of air is 15.5, $\frac{\sigma_{Ace}}{\sigma_{Air}} = 15.5$ (measured in the present work). The large separation of the Rayleigh cross sections would reduce measurement uncertainties and increase the signal intensity. The second harmonic of a Nd:YAG laser (output: 532 nm) is used for Rayleigh scattering in this work, so that the wavelength of Rayleigh scattering signal and LIF signal are close and they can be recorded with the same camera.

2.2 Flow facilities and measurement system

The coaxial jets in this study are similar to that in [6], which consists of two round tubes of different diameters placed concentrically (figure 2.1), resulting in a three-stream configuration. The mass fractions of the scalars emanating from the three streams are denoted as, ϕ_1, ϕ_2 and ϕ_3, respectively, the summation of which is therefore unity. The center stream, ϕ_1, is unity at the center jet exit, while the annular stream, ϕ_2, is unity at the annular flow exit. The co-flow air represents the third scalar, ϕ_3.

Two coaxial jets with the same center tube but different outer tubes were constructed for this work (the jet dimensions are listed in Table 2.1), with the smaller one having identical dimensions to those used in [6]. A shape cut generate 90° corners at the ends of the jet tubes. The length of the tubes are 500 mm and 570 mm for the center jet and the annulus, respectively, which are sufficiently long to guarantee fully developed flows at the jet exit, and that the flow field is expected to be insensitive to the fine details of the geometry of the jet tubes. The center stream was air seeded with approximately 9% of acetone by volume, while the annular stream was pure ethylene. The densities of the center stream and the annular stream were approximately 1.09 and 0.966 times the air density. The difference is sufficiently small for the scalars to be considered as dynamically passive.

For each coaxial jet, measurements were made for the same center jet (bulk) velocity with two annular flow (bulk) velocities, result in a total of four coaxial jet flows (Table 2.2). The velocity ratio of the annular flow to the center jet is close to unity for Cases I and III while it is approximately 0.5 for Cases II and IV. The velocities and Reynolds numbers of the four cases are listed in Table 2.2. Note that Case I is identical to the flow studied in [6]. The Reynolds numbers are calculated

	Inner tube		Annulus (outer) tube	
	D_{ji} (mm)	δ_j (mm)	D_{ai}(mm)	δ_a (mm)
Coaxial Jet I	5.54	0.406	8.38	0.559
Coaxial Jet II	5.54	0.406	10.92	0.889

Table 2.1: Dimensions of the coaxial jets. Here D_{ji}, δ_j, D_{ai} and δ_a are the inner diameter and the wall thickness of the inner tube and the annulus tube, respectively.

	Jet	U_{jb} (m/s)	Re_j	U_{ab} (m/s)	Re_a	Velocity ratio $\frac{U_{ab}}{U_{jb}}$
Case I	Jet I	34.5	12,190	32.5	7,636	0.94
Case II	Jet I	34.5	12,190	16.3	3,818	0.47
Case III	Jet II	34.5	12,190	32.5	17,263	0.94
Case IV	Jet II	34.5	12,190	16.3	8,631	0.47

Table 2.2: Characteristics of the coaxial jets. Here U_{jb} and U_{ab} are the bulk velocities of the center stream and the annular stream, respectively. The Reynolds numbers are calculated using the tube diameter D_{ji} and the hydraulic diameter of the annulus D_{ai}-(D_{ji}+2δ_j), respectively.

as $Re_j = U_{jb}D_{ji}/\nu_{air}$ and $Re_a = U_{ab}(D_{ai} - (D_{ji} + 2\delta_j))/\nu_{eth}$, where $\nu_{air} = 1.56 \times 10^{-5}\ \ m^2/s$ and $\nu_{eth} = 0.86 \times 10^{-5}\ \ m^2/s$ [46] are the kinematic viscosities of air and ethylene respectively.

The coaxial jets are placed in the center of a wind tunnel (figure 2.2) producing a air co-flow with velocity at approximately 1 m/s. The dimension of the wind tunnel is approximately 200 mm-by- 200 mm, which is large enough to isolate the coaxial jet from the influence of the ambient air, at least for the downstream locations studied in this work. The wind tunnel, with the coaxial jet mounted on it, was placed on a two-axis translation system so that measurement at different jet downstream locations can be easily accessed. The central chord of the round tube was aligned with the laser sheets through fine adjustment of the wind tunnel location in the direction perpendicular to the laser sheets. The exhaust hood that collecting exhausted gas was placed approximately 1.5 m downstream of the coaxial jet.

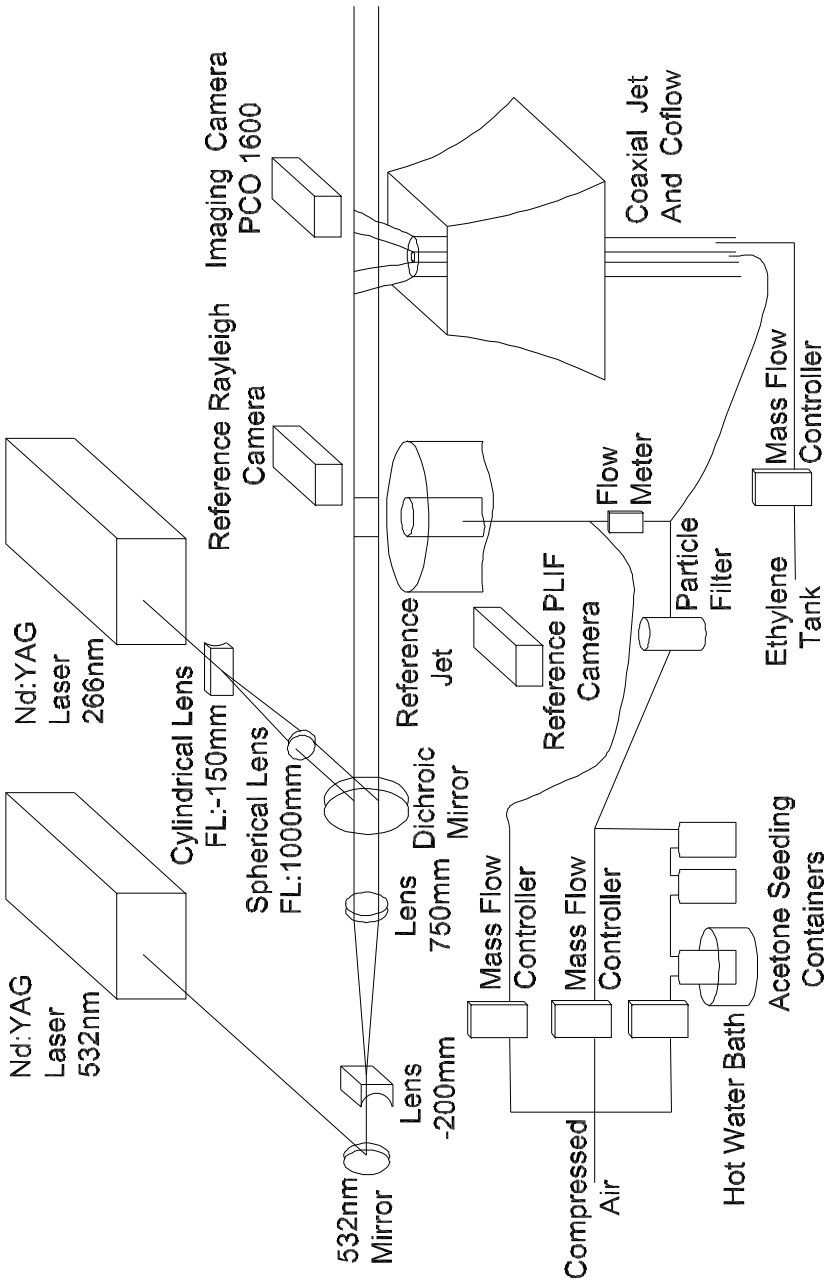

Figure 2.2: Schematic of the experimental setup.

The source of the center jet air was a facility compressor, while ethylene came from a high pressure gas cylinder with chemically pure ethylene. Alicat mass flow controllers were used to control the air and ethylene flow rates. All controllers had been calibrated by the manufacturer. Particles were removed for both streams before the gases enter the flow controllers. Three acetone containers in a series were used for seeding spectroscopic grade acetone into air through bubbling (figure 2.2). Each acetone container has a volume of 1 liter, and was approximately 70% full. Large amount of acetone are needed considering the large flow rate of air, and the heat for the evaporation have to come from the liquid acetone. Then liquid temperature would drop quickly and the seeding concentration also keep decreasing during the period of measurement if only one acetone container is used. This difficulty can be overcome with the arrangement of the three-stage bubbling containers. Most of the seeded acetone came from the first container, which was placed in a hot water bath maintained at approximately 35^oC. It is possible that excessive acetone are evaporated in the first container, however, the excess acetone will condense in the second and the third container [2]. Only little amount of acetone are needed in the second container if evaporation is not enough in the first one, which would only result in a minor change of liquid temperature in the second and the third container. Thus the second and third container ensured that the acetone vapor pressure reached the saturation level at the room temperature. As a result there was no observable variations of the seeding level during the course of the experiment, which was confirmed by monitoring the LIF and Rayleigh signal intensities of a flatfield for a long period. Approximately 30% of the center jet air flow bubbled through the three acetone containers. The acetone-doped air stream mixed with the rest of the air flow before entering the center tube. A very fine particle filter (0.01 μm) was placed in the path of the acetone-seeded air flow to remove the acetone mist, which would interfere with Rayleigh scattering imaging. In

order to monitor the pulse-to-pulse fluctuations of the laser energy, the laser intensity profile across the image height and the acetone seeding concentration for normalization, a laminar flow reference jet was placed at approximately 0.5 m upstream of the coaixal jet along the laser beam path. Approximately 5% of the center jet acetone doped air was teed off from the coaxial jet to the reference jet. Additional air (also controlled by a Alicat flow controller) was added to the reference jet to increase the velocity to maintain a steady laminar jet flow.

Simultaneous planar laser-induced fluorescence (PLIF) and planar laser Rayleigh scattering were employed to measure the mass fractions of the acetone-doped air (ϕ_1) and ethylene (ϕ_2). The experimental setup (figure 2.2) is similar to that in [6], with improvements on camera lens resolution and different optics are used to reduce the laser sheet thickness. The second harmonic (532 nm) of a Q-switched Nd:YAG laser (Quanta-Ray LAB-170 operated at 10 pulses/s) having a pulse energy of approximately 325 mJ was used for Rayleigh scattering. The fourth harmonic (266 nm) of another Q-switched Nd:YAG laser (Quanta-Ray PRO-350 also operated at 10 pulses/s) was used for acetone PLIF, with a pulse energy of approximately 80 mJ/pulse. A telescope consisted of a planar-concave cylindrical lens (-200 mm focal length) followed by a spherical lens (750 mm focal length) was placed in the beam path of the 532 nm beam to form a collimated laser sheet above the coaxial jets. The telescope in the 266 nm beam path also consisted of a planar-concave cylindrical lens and a spherical lens with focal lengths of -150 mm and 1000 mm, respectively. A dichroic mirror reflecting 266 nm wavelength and transmitting 532 nm was employed to combine the two beam paths into a single one. The focal points of the two spherical lens were located approximately above the jet centerline. The height of the laser sheets were approximately 40 mm and 60 mm, respectively for the 532 nm beam and the 266 nm beam. However, only the center 12 mm portion having a relative uniform

intensity was imaged.

A Cooke Corp. PCO-1600 interline-transfer CCD camera was used to collect both LIF and Rayleigh signals. The camera is 14-bit with two ADCs, with a interframe transfer time of 150 ns. Its quantum efficiency is over 50% for green light and the readout noise is only 11 e^- at 10MHz readout rate. Each 532 nm pulse for Rayleigh scattering was placed 210 ns before a 266 nm pulse for LIF. With the jet velocity less than 35 m/s, the time lag between the beams was sufficiently short to be considered as simultaneous. It was however longer than the interframe transfer time of the camera to ensure that the Rayleigh image was transfered before the exposure for the LIF image begins. To operate the camera with frame rate at 20 frames/s with two ADCs, the imaging array of the camera was cropped and the pixels binned 2×2 before readout, resulting in an image of 800 pixels wide by 500 pixels high. The timing of lasers and cameras were controlled by a delay generator (Stanford Research System DG535). A custom lens arrangement consisting of a Zeiss 135mm f/2 Apo lens followed by a Zeiss planar 85mm f/1.4 lens was used for the PCO-1600 camera. The lenses, both focused at infinity, were connected face to face with the 85mm lens mounted on the camera. The pixel size of the camera is 7.4 μm (square), corresponding to 22.9 μm in the image plane after binning 2×2. The field of view was 11.45 mm (high) by 18.3 mm (wide). The LIF and Rayleigh images of the reference jet were recorded with two Andor ICCDs (Both are iStar 334T), respectively. They were placed face to face on either sides of the laser sheet and the images were not intensified. Background light was suppressed using a series of hard blackboards to enclose the wind tunnel, cameras and the reference jet.

The registration between the reference jet cameras and the main jet camera is needed for the data reduction when the reference jet was used to monitor the laser profile across the image height. It was done with the help of a fine metal wire

(about 0.3 mm in diameter) that was placed between the dichroic mirror and the reference jet along the beam path. The coaxial jet was replaced by a McKenna burner, above which a uniform scalar field (flatfield) larger than the field of view of the camera is sustained. Part of the laser sheet was blocked after it passed the fine wire, then a shadow show up in both the reference jet cameras and the main jet camera. The registration between cameras can be obtained by calculating the correlation coefficient of the signal intensity profiles from the two cameras in the neighborhood of the shadows. The exact pixel shift of the two cameras is at the peak of the correlation coefficient between the two vertical profiles. The difference in the pixel size needs to be adjusted before calculating the correlation coefficients, and it was done by resampling the reference images in the vertical direction.

An indirect way has to be used to check the collimation of the laser sheet because the laser heights are much larger than the field of view of the cameras. Two fine metal wires with a separation about 7 mm were placed along the laser path the same way as that for registration. The distance between the two shadows in reference jet camera images and the main jet camera image should be the same when the laser sheet is perfectly collimated. The fine adjustment of the laser sheet collimation is a trial and error process. The travel path of the laser sheet also needs to be horizontal relative to the cameras to make the data reduction process easier. We can easily tell whether the laser sheet travel horizontally or not from the shadow of wire in the images. Some adjustment of the camera or the beam reflecting optics are needed if the shadows are not horizontal in the images.

The camera lens focus can be roughly found by letting the laser sheet skip the surface of a grid target, which is imaged by the camera. However, the accuracy would be only on the order of mini-meter. The camera lens resolution is very sensitive to the camera lens focus due to the small depth of field resulting from the large magnification

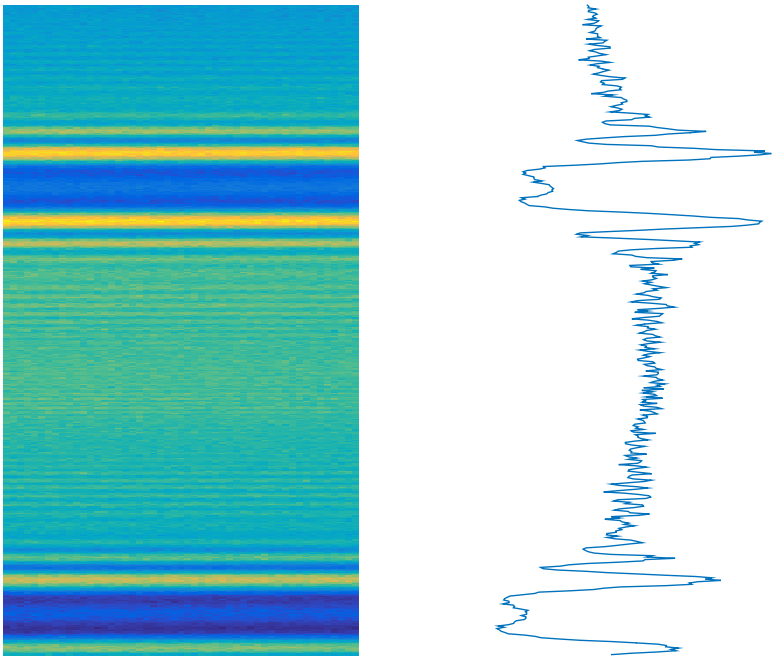

Figure 2.3: A sample image of fringes generated by the fine wire blocking part of the 532 nm laser sheet at the upstream when the camera lens focus is good. The right part is a profile of a single column in the left image.

ratio and the large aperture (small f-number) of the camera lens. Thus the camera lens focus needs be fine tuned for better scalar dissipation resolution. The camera lens focus can be found with the help of the shadow in the main jet camera images generated by the fine wire. The shadow in the main camera image, or at the laser sheet focus, is not a simple dark stripe with the edge similar to an error function that have a smooth transition to bright stripes. Some fine fringes show up due to the interference between the two parts of the laser sheet that was separated by the fine wire. The fringes would be blurred or even disappear when the camera lens focus is not good. The fringes at good camera focus is shown in figure 2.3. A good camera lens focus is that when the fringes in the cameras show most details. Fine adjustment of the camera lens focus can be done by adjusting the focus of the Zeiss planar 85mm f/1.4 lens while real time images of the fringes are taken.

2.3 Data reduction procedures

The data reduction procedures in this work are in general similar to that described in [9], however, with some modifications due to different (and better) calibration process.

2.3.1 Rayleigh scattering

Rayleigh signal is proportional to the laser intensity, the effective Rayleigh cross section and it can be modeled as [60]:

$$S_{\mathrm{Ray}}(i,j,k) = \mathrm{Res}_{\mathrm{Ray}}(i,j) \cdot I(i,k) \cdot \sigma_{\mathrm{eff}}(i,j,k) + \mathrm{BG}_{\mathrm{Ray}}(i,j) \tag{2.1}$$

where S_{Ray} is the Rayleigh signal intensity, I is the laser intensity, σ_{eff} is the effective Rayleigh cross section. The symbol i, j and k are the pixel numbering in vertical direction, the pixel numbering in the horizontal direction and the frame number. The laser intensity varies across the beam height direction (i) and have pulse to pulse variations (k). The system response, $\mathrm{Res}_{\mathrm{Ray}}$, is consisted of all factors that are independent of the laser intensity and the scalar values, including the absorption cross section, the quantum yield, the solid angle of the collection optics, the quantum efficiency of the camera and the lens vignetting et al. Lens vignetting is the main contributor to the pixel-to-pixel variation of $\mathrm{Res}_{\mathrm{Ray}}$, especially in the case of the face to face connection of two camera lens that have large magnification ratio in this work. The non-uniformity of pixels can also be a major contributor to the pixel-to-pixel variation of $\mathrm{Res}_{\mathrm{Ray}}$ and cause the dependence of $\mathrm{Res}_{\mathrm{Ray}}$ on i and j. $\mathrm{BG}_{\mathrm{Ray}}$ represents the background light signal and the dark current. The Rayleigh scattering background was measured with helium flatfield while keeping the lasers operating the

same way as recording normal images, because the Rayleigh cross section of helium is negligible compared to that of air. The effective Rayleigh cross section is the mole weighted average of the Rayleigh cross sections of all three species,

$$\sigma_{\text{eff}} = \sigma_1\phi_1 + \sigma_2\phi_2 + \sigma_3\phi_3, \tag{2.2}$$

where ϕ_is represent the mole fractions of each stream and satisfy the constraint

$$\phi_1 + \phi_2 + \phi_3 = 1. \tag{2.3}$$

and σ_is are the corresponding Rayleigh cross section:

$$\begin{aligned} \sigma_1 &= (1-c)\sigma_{\text{air}} + c\sigma_{\text{ace}}, & (2.4)\\ \sigma_2 &= \sigma_{\text{eth}}, & (2.5)\\ \sigma_3 &= \sigma_{\text{air}} & (2.6) \end{aligned}$$

where c is the acetone concentration in the center stream (ϕ_1), and σ_{ace}, σ_{eth} and σ_{air} are the Rayleigh cross section of acetone, ethylene and air, respectively.

The model equation can be applied to both reference and main jet images:

$$S_{\text{Ray}}(i,j,k) = \text{Res}_{\text{Ray}}(i,j)\cdot I(i,k)\cdot\sigma_{\text{eff}}(i,j,k) + \text{BG}_{\text{Ray}}(i,j) \tag{2.7}$$

$$S^r_{\text{Ray}}(i,j,k) = \text{Res}^r_{\text{Ray}}(i,j)\cdot I(i,k)\cdot\sigma^r_{\text{eff}} + \text{BG}^r_{\text{Ray}}(i,j) \tag{2.8}$$

The laser intensity term can be cancelled if we take the ratio of the two equations with the background terms been subtracted from the signal intensities at first,

and we can get

$$\frac{S_{\mathrm{Ray}}(i,j,k)}{(1/N)\sum_{l=1}^{N} S^{r}_{\mathrm{Ray}}(i,j_0+l,k)} \cdot \frac{(1/N)\sum_{l=1}^{N} \mathrm{Res}^{r}_{\mathrm{Ray}}(i,j_0+l)}{\mathrm{Res}_{\mathrm{Ray}}(i,j)} = \frac{\sigma_{\mathrm{eff}}(i,j,k)}{\sigma^{r}_{\mathrm{eff}}} \tag{2.9}$$

where S_{Ray} and S^{r}_{Ray} represent the main and reference rayleigh signals with background signals been subtracted hereafter. The signal intensity of the reference image is averaged along the beam propagation direction to reduce shot noise effects.

The relative response

$$\frac{(1/N)\sum_{l=1}^{N} \mathrm{Res}^{r}_{\mathrm{Ray}}(i,j_0+l)}{\mathrm{Res}_{\mathrm{Ray}}(i,j)} \tag{2.10}$$

needs to be found with calibration. The calibration measurement was done by replacing the coaxial jet flow with a flatfield flow generated by the McKenna burner, while the reference flow, cameras and lasers are operating in the the same way as normal measurements. The McKenna burner with a diameter of 60 mm generate a uniform scalar field at the focus of the main camera. With a known and uniform gas (Ethylene, acetone doped air or pure air) filling the image field, the relative response (equation 2.10) can be found when applying equation 2.9 to the calibration measurements because the ratio between the Rayleigh cross sections (the right side of equation 2.9) is known.

With the relative response accounted, the rayleigh signal is reduced to a normalized Rayleigh cross section (the right hand side of equation 2.9). The normalized Rayleigh cross section is the ratio between the effective Rayleigh cross section in the flow field and the Rayleigh cross section of the mixture for calibration (air). After a

few steps of derivations, the equation becomes:

$$\sigma_{\text{norm}} = \frac{\sigma_{\text{eff}}}{\sigma_{\text{air}}} = 1 - \phi_2 - c\phi_1 + c\frac{\sigma_{\text{ace}}}{\sigma_{\text{air}}}\phi_1 + \frac{\sigma_{\text{eth}}}{\sigma_{\text{air}}}\phi_2 \tag{2.11}$$

which can be rearranged as:

$$\sigma_{\text{norm}} - 1 = c\phi_1\left(\frac{\sigma_{\text{ace}}}{\sigma_{\text{air}}} - 1\right) + \phi_2\left(\frac{\sigma_{\text{eth}}}{\sigma_{\text{air}}} - 1\right) \tag{2.12}$$

where $\frac{\sigma_{Eth}}{\sigma_{Air}} = 7$ and $\frac{\sigma_{ace}}{\sigma_{Air}} = 15.5$.

2.3.2 PLIF

The laser intensity for PLIF in this work is in the linear regime, and the LIF signal can be modeled as:

$$\begin{aligned} S_{\text{PLIF}}(i,j,k) &= \text{Res}_{\text{PLIF}}(i,j) \cdot I(i,j,k) \cdot \phi_1 \cdot c \cdot \frac{A_{21}}{Q_{21} + A_{21}} \\ &+ \text{BG}_{\text{PLIF}}(i,j) \end{aligned} \tag{2.13}$$

where Res_{PLIF} is similar to Res_{Ray} for Rayleigh signal and includes all factors that are independent of laser intensity and scalar values; $I(i,j,k)$ is the laser intensity and its dependence on j is due to laser intensity attenuation because of the large absorption; A_{21} represents Einstein's constant; Q_{21} represents quenching, and $Q_{21} = q_1\phi_1 + q_2\phi_2 + q_3\phi_3$, and

$$q_1 = (1-c)q_{\text{air}} + cq_{\text{ace}} \approx (1-c)q_{\text{air}}, \tag{2.14}$$

$$q_2 = q_{\text{eth}}, \tag{2.15}$$

$$q_3 = q_{\text{air}} \tag{2.16}$$

where q_{air}, q_{ace} and q_{eth} are the quenching coefficients of air, acetone and ethylene, respectively to acetone LIF. Quenching of acetone to itself is negligible compared to that of air, so it is deleted from equation 2.14.

When $Q_{21} >> A_{21}$ [9], the model equation can be simplified to

$$S_{\text{PLIF}}(i,j,k) = \text{Res}_{\text{PLIF}}(i,j) \cdot I(i,j,k) \cdot \phi_1 \cdot c \cdot \frac{A_{21}}{q_1\phi_1 + q_2\phi_2 + q_3\phi_3} \quad (2.17)$$

where S_{PLIF} represents signal intensity with Background signal been subtracted.

One big difference between the model equation of PLIF and Rayleigh is the variation of laser intensity along its propagation direction. Acetone has very large absorption cross section for the 266 nm wavelength. The variation of the laser intensity follows Beer's law. It drops by about 4% after passing the jet. However, we can neglect the variation of laser intensity in the first place, and compensate it in the last step of data reduction. The PLIF equation becomes similar to the Rayleigh equation after ignoring laser intensity attenuation, and again the relative response needs to be found from calibration. When the flatfield is used for calibration, the whole imaging field would be filled with acetone doped air, which would cause a large drop (about 15%) of laser intensity across the width of the image. So the calculated relative response was the actual relative response times the laser intensity attenuation percentile. The laser attenuation effect has to be corrected before the relative response been used as actual relative response.

With the relative response accounted, the PLIF signal is reduced to (after a few steps of derivations):

$$k_{\text{norm}} = \frac{k_{\text{eff}}}{k_{\text{Ref}}} = \frac{(1-c)\phi_1}{1 - c\phi_1 + \left(\frac{q_{\text{eth}}}{q_{\text{air}}} - 1\right)\phi_2} \quad (2.18)$$

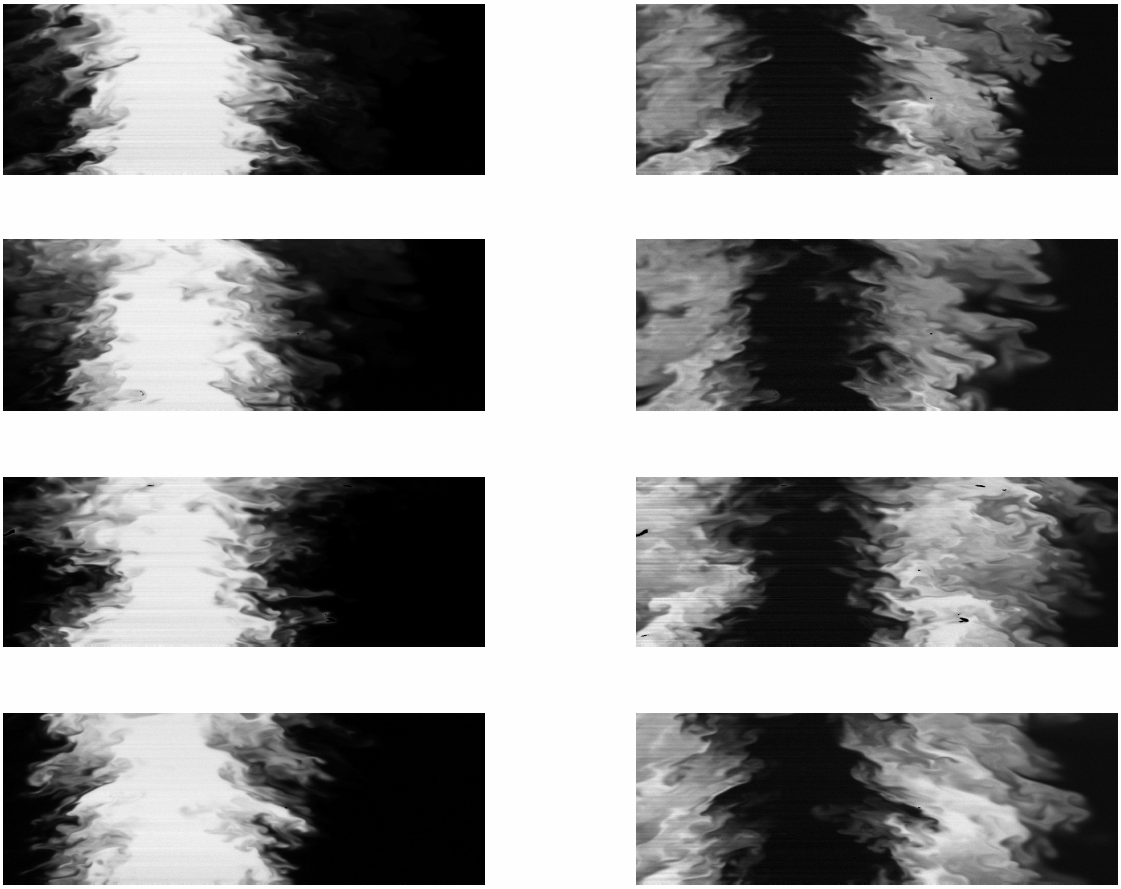

Figure 2.4: Instantaneous (Sample) images of the center stream (Left) and the annular stream (Right) at the near field. The first, second, third and fourth row are for Cases I, II, III and IV, respectively. The top and the bottom of the images are at 25.45mm and 14mm downstream of the jet exit, respectively.

The scalar values can be obtained from equation 2.12 and equation 2.18. Sample (instantaneous) images of the center stream and the annular stream at the near field are shown in figure 2.4. A total of 7200-7600 images were taken for each cases at the two near field downstream locations, where cross-stream results are shown in the following Chapters. About 2400-3000 images were taken for the other three downstream locations, for which only the centerline results are shown.

Chapter 3

Measurement resolution of the scalar dissipation rate

3.1 Measurement resolution of the scalar dissipation rate

Scalar dissipation rate, $\chi = 2D\frac{\partial\phi}{\partial x_i}\frac{\partial\phi}{\partial x_i}$, is an important turbulent mixing quantity and a measure of the speed at which scalar inhomogeneities decay. It shows up directly in laminar flamelet modeling equation and serves as a parameter characterizing the flame structure in turbulent non-premixed flames. Accurate measurement of scalar dissipation rate (or scalar gradient) is more challenging than measuring scalar itself due to smaller length scale. The smallest spatial length scale for this work is close to the Kolmogorov scale, because Schmidt number ($Sc = \nu/D$) is close to unity.

To assess the measurement resolution, we used both Rayleigh scattering and LIF to measure ϕ_1 by feeding the annular stream with an air flow. The ϕ_1 mean profiles from both techniques at $x/d = 3.29$ (where d is the diameter of the inner

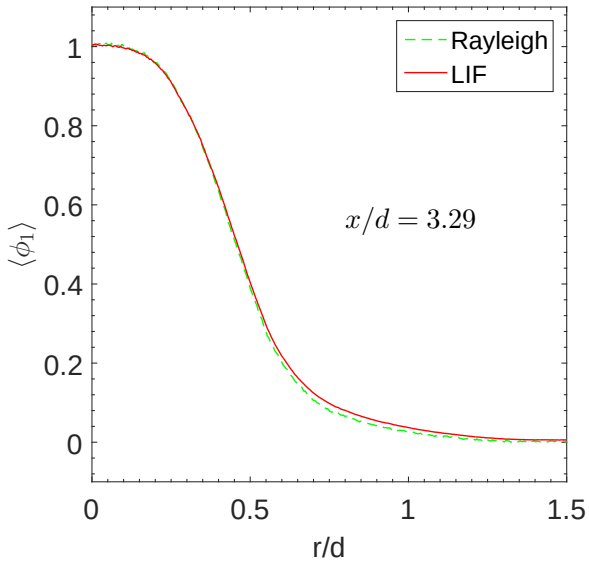

Figure 3.1: Cross stream mean profiles of the center stream at $x/d = 3.29$. The annular stream is air flow with the same flow rate of ethylene for Case I.

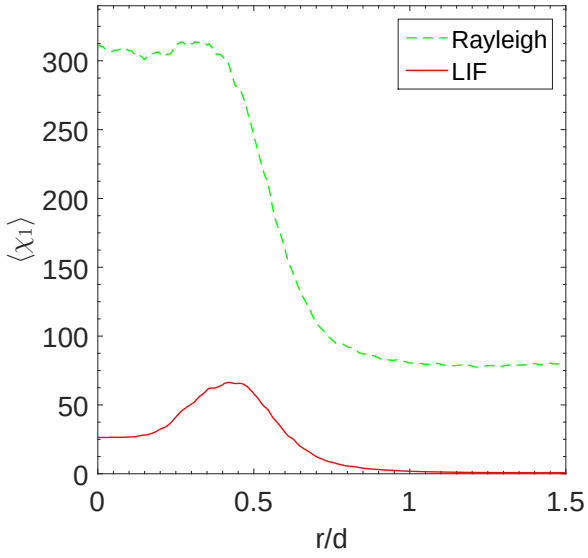

(a)

Figure 3.2: Cross stream profiles of the mean scalar dissipation rate before noise correction at $x/d = 3.29$ using 10th order central finite difference scheme. The annular stream is air flow with the same flow rate of ethylene of Case I.

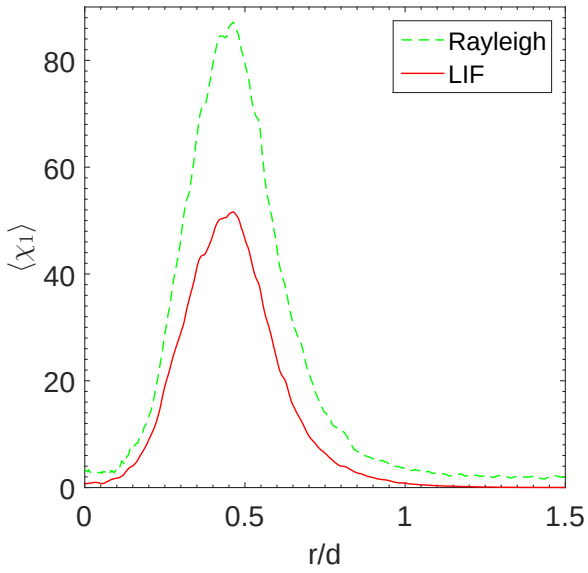

Figure 3.3: Same as figure 3.2 but after noise correction.

tube) are shown in figure 3.1. The annular stream was air flow with the same flow rate as ethylene for Case I. All results shown in this Chapter are using this set of data. The two mean profiles are essentially the same except little difference at the tail, which might be due to effects such as beam steering or nonlinearity of camera at low signal levels. Figure 3.2 shows the mean dissipation rate (before noise correction) profiles at $x/d = 3.29$. The 10th Order central finite difference scheme is used to calculate the derivatives. The mean dissipation rate should be small close to the centerline ($r/d < 0.1$) because only pure ϕ_1 exist there. However, the uncorrected mean dissipation rate is very large at centerline, which is due to large noise contribution. Shot noise add to the signal value when reading out, and it tends to result in a larger calculated dissipation rate. The uncorrected mean dissipation rate at the centerline of Rayleigh scattering measurement is much larger than LIF is a result of smaller signal intensity and thus smaller signal to noise ratio (SNR) for Rayleigh scattering. The Rayleigh scattering signal intensity of pure ϕ_1 mixture is less than half of the LIF signal intensity at the seeding level and laser energy of the present work. Moving

away from the centerline to $x/d > 1$, there is no ϕ_1 and the dissipation rate should also be zero. However, the uncorrected dissipation rate from Rayleigh measurement is also very large whereas LIF measurement have a close to zero mean dissipation rate. The reason is that air have Rayleigh scattering signal while it does not have LIF emission at all. Thus the non-zero mean dissipation rate from Rayleigh scattering is again due to measurement noise.

The shot noise contribution to the mean dissipation rate can be removed using the method developed by Cai and Tong [7]. Figure 3.3 shows the noise corrected ϕ_1 mean dissipation rates. The corrected dissipation profiles have very small values at both the centerline and the tail, suggesting that the noise correction method is effective. The small but non-zero mean dissipation rate close to the centerline and at the tail for Rayleigh scattering is a result of not good statistical convergence since only 600 images were taken for these test cases. Figure 3.4 shows the calculated dissipation rate using different orders of central finite difference scheme VS C_N, which is dependent on the orders of the finite difference scheme. The C_N value is larger for higher orders of finite difference scheme. Details about the noise correction method and C_N can be found in [7]. The straight line in the figure is a linear fit of the calculated dissipation rates using the 6th, 8th and 10th order finite difference scheme (the last three circles in the figures). The dissipation rate is fully resolved when the three circles stay exactly on the straight line, the intercept of which on the ordinate ($C_N = 0$) is the noise corrected mean dissipation rate. Lower orders difference scheme would also fully resolve the dissipation rate if that circle also stays exactly on the straight line. All the circles stay right on the line for $r/d = 0$, and the intercept is basically zero. From these figures, we can see that the small non-zero noise-corrected mean dissipation for Rayleigh scattering (figure 3.3) is due to the statistical convergence. Move to $r/d = 0.447$, only the second order finite difference cannot resolve the dissi-

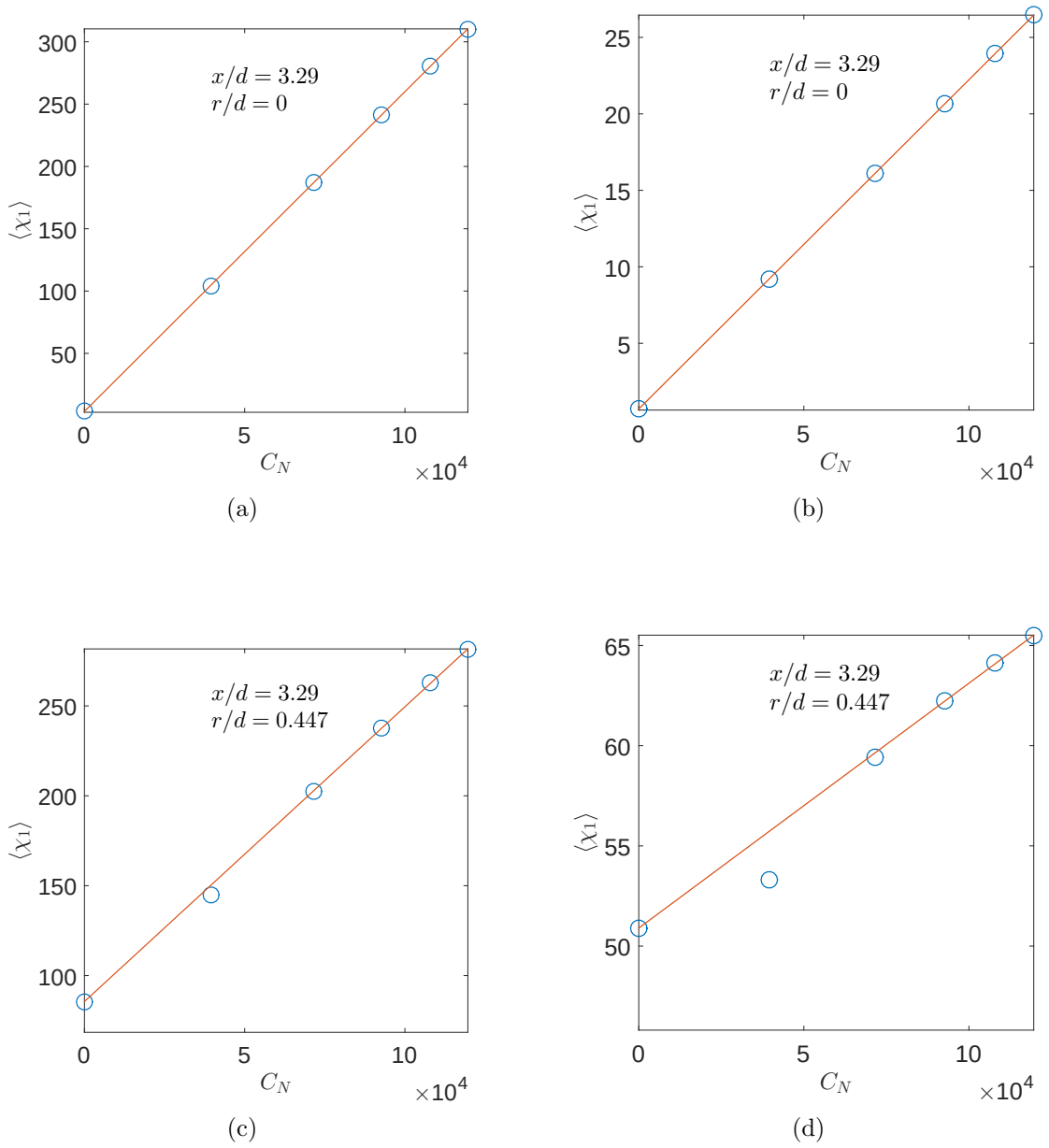

Figure 3.4: Calculated mean dissipation rate VS C_N. C_N is a scheme dependent factor, the five non-zero C_N are corresponding to the 2nd, 4th, 6th, 8th and 10th order central finite difference scheme. The straight line is a linear fit of the last three circles. The circle with $C_N = 0$ is the intercept of the line on the ordinate. The left column is for Rayleigh scattering measurement while the right is for LIF measurement.

pation rate for Rayleigh scattering. For LIF measurement, the 4th order circle stays a little below the line, suggesting it does not fully resolve the mean dissipation rate. Results at other radial locations are similar. The noise contribution has been successfully removed from mean dissipation rate for both techniques. The noise corrected mean dissipation rate for Rayleigh scattering is much larger than for LIF (figure 3.2). The peak value from Rayleigh scattering is approximately 40% higher than from LIF, thus the resolution of the two techniques are different. The measurement resolution is affected by several factors including the camera lens resolution, the image pixel size, the finite difference scheme and the laser sheet thickness.

Camera lens resolution (optical blurring) plays an important role in the dissipation resolution. Line-spread function (LSF) is a good measure for imaging blurring [70]. The Line-spread function was measured by translating a razor blade across the imaging plane, the setup of the measurement is the same as in [11]. The knife edge is placed at the focal plane and been back-illuminated, then the step jump profile of the knife edge is an error function like profile at the image plane due to optical blurring, the length scale of which is the LSF of the camera lens. The signal intensity of a single pixel is monitored as the knife-edge is translated across the imaging plane, since this way of measuring LSF is independent of camera pixel size or the resolution of camera itself. The full width at half maximum (FWHM) of the error function profile, or LSF, is approximately 38 μm for the lens arrangement.

The measurement system resolution is very sensitive to the camera lens focus, due to the small depth of field resulting from the large magnification ratio and the large aperture (small f-number) of the camera lens. We note that the wavelength of the Rayleigh scattering signal is the same as the laser light (532 nm), with an extremely small linewidth. By contrast, the LIF emission from acetone excited at 266 nm is broadband, from 320 nm to 550 nm with the peak at approximately 410

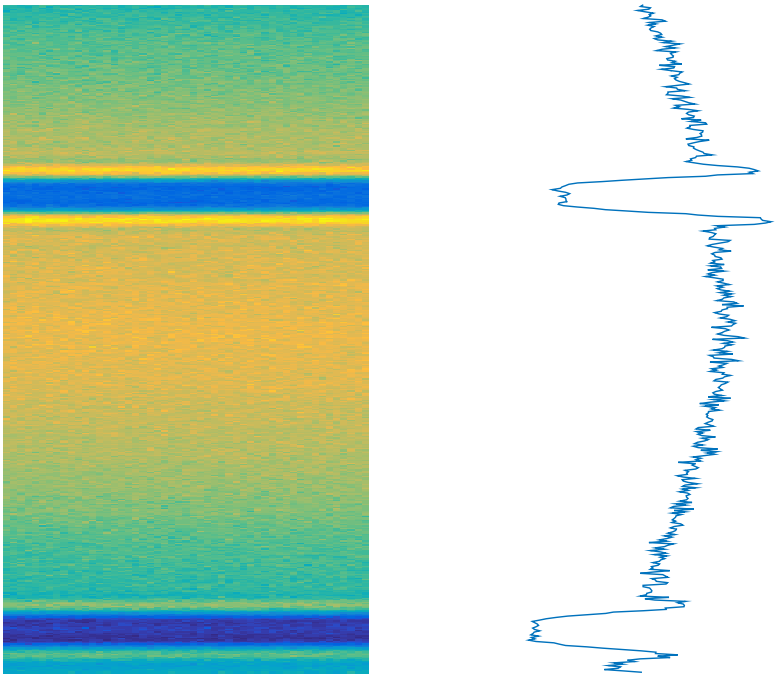

Figure 3.5: A sample image of fringes generated by the fine wire blocking part of the 266 nm laser sheet at the upstream. The right part is a profile of a single column in the left image.

nm [3]. The focal length of the camera lens vary with different light wavelength considering that they are usually achromat, for which the variation of focal length should be on the order of hundreds of micro-meter. This variation of focal length would cause a less well focused camera lens for imaging acetone LIF because its emission is broadband. Although we do not have a model to quantify its effects on the resolution of the scalar dissipation, the difference in the quality of the camera lens focus for the two techniques is obvious, with the image of the fringe produced by the fine wire having much less detail for the 266 nm beam. Figure 3.5 shows the fringes generated by blocking part of the 266 nm beam with a fine wire at the upstream. It shows much less details compared to that of the 532 nm (figure 2.3), although shorter wavelength tends to generate finer fringes. The camera lens focus for LIF is worse compared to Rayleigh scattering.

Non-zero sheet thickness average the scalar in the direction perpendicular to the imaging plane. In order to measure the sheet thickness, we design a simple beam profile measurement system in the lab. The laser beam was sampled by a few beam splitters, then passing the cylindrical lens and the spherical lens, at the focus of which the laser sheet hit a filter. It was a long pass filter with cut-off wavelength at 570 nm for the 532 nm beam, and a uv absorption glass for the 266nm beam. The filters absorb the laser light and have fluorescence emission, the signal intensity of which are linear to the laser intensity. A CCD camera was used to record the emitted light signal to obtain the sheet thickness. The beam profile would be Gaussian like if the beam quality is good. The sheet thicknesses (FWHM) were about 110 and 90 μm, respectively, for the 226 and 532 nm beams.

The effects of pixel size on measurement resolution is twofold. First, light collected by each pixel is a sum (average) of signal from the corresponding probe volume. To some extent, pixel averaging is like apply a top-hat filter to the scalar field with the filter size equals the pixel size. Second, different pixel size corresponding to different sampling rate of the scalar field. Sampling rate has to be high enough to fully resolve scalar gradient. Apart from sampling rate, the system resolution is also affected by the differential schemes being used. Central finite difference schemes are employed in this work. With higher orders of difference scheme, the calculated dissipation rate would be higher if lower orders of difference scheme can not fully resolve the gradient, because higher orders of finite difference scheme have higher resolution power. We use the same camera and camera lens for both LIF and Rayleigh scattering, thus LSF and pixel size are the same for the two techniques and not the source of different resolution.

The combined resolution can be estimated by comparing the measured scalar dissipation rate to the prediction using a scalar energy spectral model, which is filtered

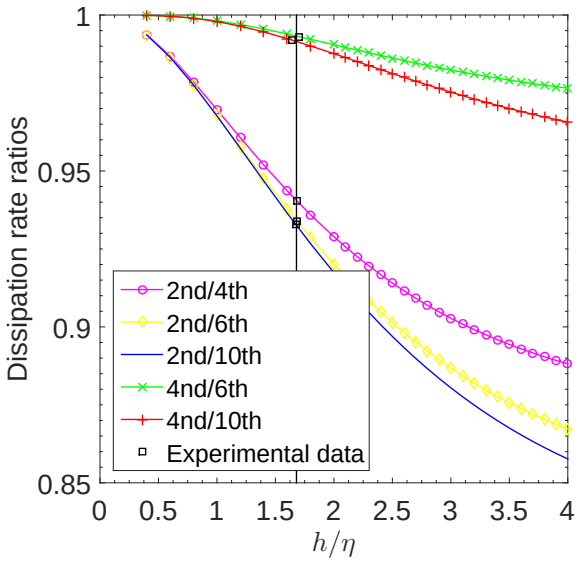

Figure 3.6: Estimation of the scalar length scale by matching the ratio of the dissipation rates using finite difference scheme of different orders from the experimental data to those from the model spectrum, where h and η represent the pixel size and the scalar length scale, respectively.

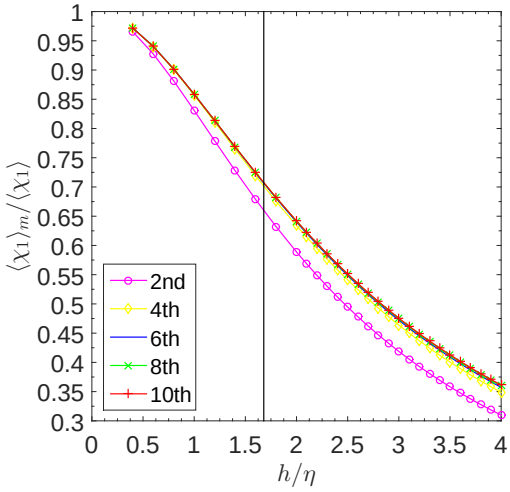

Figure 3.7: Estimation of the system resolution of the mean dissipation rate, where $\langle\chi_1\rangle$ is the true mean dissipation rate for the model spectrum, while $\langle\chi_1\rangle_m$ is that for filtering the model spectrum by accounting all the effects.

in the spectral domain taking into account all the above mentioned effects except the effects of the broad-band LIF signal on the camera lens focus. The three-dimensional model spectrum of Pope [42] for a homogenous isotropic turbulent scalar field is used. The model for the effects of LSF, pixel averaging, laser sheet thickness and differential scheme are the same as that in [71], with the parameters using values given above. The scalar dissipation length scale can be inferred by matching the ratios of the dissipation rates calculated with finite difference schemes of different orders using the experimental data (all noise corrected) to those using the scalar energy spectrum [5]. The results show that the scalar dissipation length scale is approximately 14 μm (figure 3.6), and that the Rayleigh scattering and LIF techniques resolve approximately 72% (figure 3.7) and 68%, respectively, of the mean scalar dissipation rate. Thus, the difference in the laser sheet thickness account for only 4% difference in the peak mean dissipation rate, since the other parameters accounted are the same for the two techniques. The effects of averaging in the imaging depth direction is expected to be small when we only calculate the two in plane dissipation components. Thus measurement resolution should not be sensitive to the sheet thickness considering that the sheet thickness are large compared to the length scale of other factors and the smallest scalar length scale. Then the large difference in the peak mean dissipation rate (40%) must be due to the camera lens focus. The resolved mean dissipation rate of acetone LIF is corresponding to approximately 43% of the "true" mean dissipation rate, which is inferred from Rayleigh scattering measurement.

The peak of the mean dissipation rate is at $r/d = 0.46$ for both LIF and Rayleigh measurement, although their magnitudes are different. The worse resolution for LIF does not change the shape of the mean dissipation rate profile. Figure 3.8 shows the noise corrected conditional scalar dissipation rate at three radial locations at $x/d = 3.29$. Close to the centerline ($r/d = 0.207$), the dissipation rate increase when

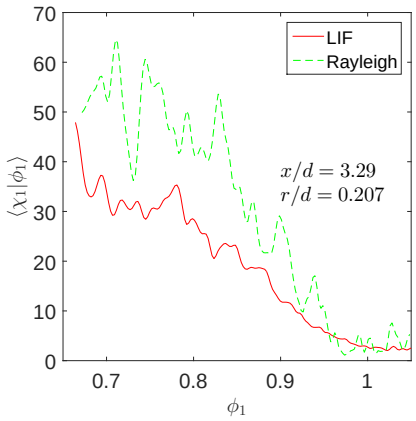

(a)

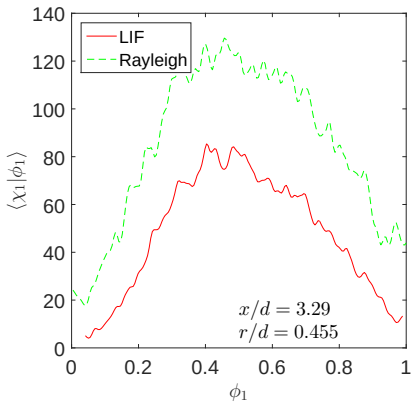

(b)

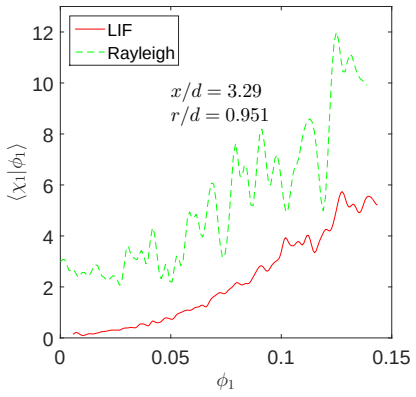

(c)

Figure 3.8: Noise-corrected conditional scalar dissipation rate. The physical locations are given in the legend.

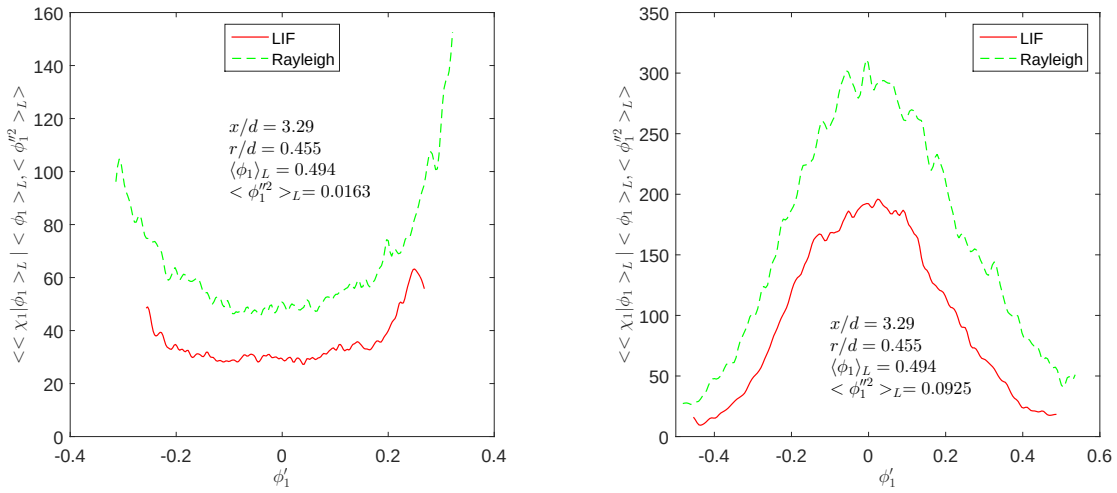

(a) (b)

Figure 3.9: Noise-corrected filtered conditional scalar dissipation rate. The physical locations are given in the legend. The conditional scalar mean and SGS variance are also shown in the legend.

the scalar value is away from $\phi_1 = 1$. The dissipation rate is very small near $\phi_1 = 1$ in scalar space, and both LIF and Rayleigh give similar values. Moving away from $\phi_1 = 1$, the conditional dissipation rate from Rayleigh scattering is larger by approximately 30% than LIF, however, the general trend of the two profiles does not show much difference. The large fluctuations is due to not good statistical convergence. Moving to $r/d = 0.455$, the conditional dissipation rate peak near $\phi_1 = 0.4$ for both LIF and Rayleigh. Again, the shapes are similar but with different magnitudes. The maximum value from Rayleigh scattering is larger than LIF by approximately 38%. Moving further away from the centerline to $r/d = 0.951$, the conditional dissipation rate is very small near $\phi_1 = 0$ and increases away from $\phi_1 = 0$. The dissipation rates are small at this radial location, with Rayleigh scattering gives a higher value than LIF in the whole scalar space, which is due to uncertainties in noise correction because the Rayleigh signal of air is non-zero while the LIF signal of pure air is zero.

Figure 3.9 shows the filtered conditional scalar dissipation rate at $x/d = 3.29$

and $r/d = 0.455$. The conditional variables are the filtered mean and the SGS variance. The square "top-hat" (or box) filter is used here, and the filter size was 0.69mm. The left column is for the small SGS variance, in which case ϕ_1 is well mixed with air. The filtered conditional dissipation rate is small when ϕ_1 is close to the filtered mean, $\langle\phi_1\rangle_L$, or $\phi_1' = \phi_1 - \langle\phi_1\rangle_L$ close to zero. The filtered conditional dissipation rate increases as ϕ_1' go away from zero. The noise corrected filtered conditional dissipation rate is larger for Rayleigh measurement than LIF at the whole scalar space, however, their shapes are again similar. The mixtures are segregated when the SGS variance is large (figure 3.9b), and the filtered conditional dissipation rate peak near $\phi_1' = 0$ for both Rayleigh and LIF. The peak dissipation rate is approximately 35% higher for Rayleigh measurement, however, their shape does not show much difference. Results at other locations show similar trends.

The resolved dissipation rates (mean dissipation rate, conditional dissipation rate and filtered conditional dissipation rate) from Rayleigh scattering measurement are generally much larger than from LIF measurement due to better resolution (Camera lens focus). However, the shape of the profiles does not show much difference between them. The profiles peak at the same location in both physical and sample space. They start to increase at similar locations. These similarities are likely because the scale corresponding to the peak of the dissipation spectrum is still resolved as our resolution is equivalent to $\kappa\eta \approx 0.3$ using Pope's model dissipation spectrum [42]. Thus, the spatial resolution of the measurement system is sufficient to support the results obtained and the conclusions drawn from the measured dissipation rate when normalized by the peak measured dissipation.

3.2 Data analysis procedures

In the following Chapters, the first and second order derivatives of the scalars are needed to calculate the dissipation rate and diffusion, respectively. The 10th-order central finite difference scheme are used throughout the rest of this work. The first and second order derivatives are as follows:

$$\begin{aligned} hX_i' = &\frac{2100}{2520}(X_{i+1} - X_{i-1}) - \frac{600}{2520}(X_{i+2} - X_{i-2}) + \frac{150}{2520}(X_{i+3} - X_{i-3}) \\ &- \frac{25}{2520}(X_{i+4} - X_{i-4}) + \frac{2}{2520}(X_{i+5} - X_{i-5}) \end{aligned} \tag{3.1}$$

$$\begin{aligned} h^2X_i'' = &\frac{42000}{25200}(X_{i-1} - 2X_i + X_{i+1}) - \frac{6000}{25200}(X_{i-2} - 2X_i + X_{i+2}) + \frac{1000}{25200}(X_{i-3} - 2X_i + X_{i+3}) \\ &- \frac{125}{25200}(X_{i-4} - 2X_i + X_{i+4}) + \frac{8}{25200}(X_{i-5} - 2X_i + X_{i+5}) \end{aligned} \tag{3.2}$$

where X, i, h represent the scalars, pixel number and pixel size respectively. Two in-plane components of the dissipation rate and the diffusion are calculated and the final value is the summation of the two components. For example, the dissipation rate and the diffusion for ϕ_1 are $\chi_1 = 2D_1\big(\frac{\partial\phi_1}{\partial x}\frac{\partial\phi_1}{\partial x} + \frac{\partial\phi_1}{\partial r}\frac{\partial\phi_1}{\partial r}\big)$ and $D_1\nabla^2\phi_1 = D_1\big(\frac{\partial^2\phi_1}{\partial x^2} + \frac{\partial^2\phi_1}{\partial r^2}\big)$, where x and r represent the streamwise and cross-stream direction, respectively.

Typically 7200-7600 images were used to calculate the statistics for the two near field downstream locations, for which the cross-stream results are also shown. And approximately 2400-3000 images were used for the other three downstream locations, for which only the centerline results are shown. Noise corrections were performed in the following chapters for the rms fluctuations, the correlation coefficient, the segregation parameter, the mean and conditional dissipation and cross-dissipation, the SGS variance and the conditionally filtered dissipation and cross-dissipation. The noise correction procedures are the same as in [6]. The JPDF, conditional diffusion, conditional dissipation rates, FJDF, conditionally filtered diffusion and the conditionally filtered dissipation rates were calculated using Kernel Density Estimation (KDE)

[66] in two dimensions with a resolution of 400 by 400 in the scalar sample space with an oversmooth parameter of 1.3. The statistical uncertainties and bias for JPDF and FJDF were estimated using the bootstrap method [19], while the uncertainties for the conditional dissipation rates and the conditionally filtered dissipation rates were estimated using the method given by [51]. The magnitudes of the statistical uncertainties are similar to those in [6].

Chapter 4

Effects of mean shear and scalar initial length scale on three-scalar mixing in the context of RANS

In this Chapter analyses of the scalar means, rms fluctuations, fluctuation intensities, correlation coefficient, segregation parameter, JPDF, mean and conditional dissipation rates, and conditional scalar diffusion computed from the two-dimensional images are presented.

4.1 Evolution on the jet centerline

The scalar mean profiles on the jet centerline are shown in figure 4.1. For $x/d < 6$ (Here d denotes the inner diameter of the inner tube), the profiles for both $\langle\phi_1\rangle$ and $\langle\phi_2\rangle$ overlap for Cases I and II and for Cases III and IV and the sum of $\langle\phi_1\rangle$ and $\langle\phi_2\rangle$ is close to unity. Further downstream, the co-flow air (ϕ_3) as well as more ϕ_2 reach the centerline, and $\langle\phi_1\rangle$ decreases monotonically, while $\langle\phi_2\rangle$ increases and reach

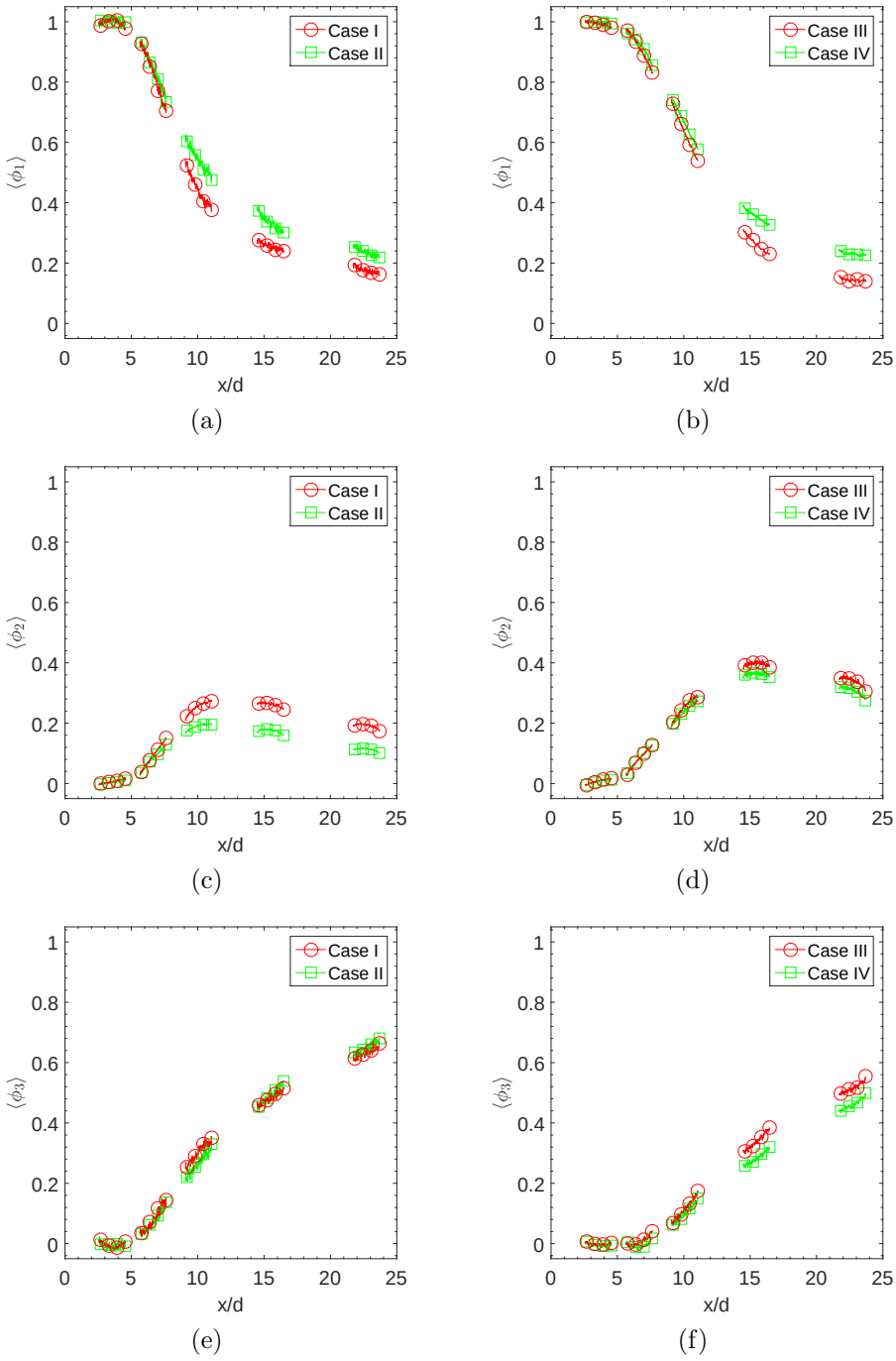

Figure 4.1: Evolution of the mean scalars on the jet centerline.

a maximum before decreasing further downstream. The profiles of Case I and Case II also begin to depart from each other, with Case I having smaller $\langle\phi_1\rangle$ values but larger $\langle\phi_2\rangle$ values. The smaller $\langle\phi_1\rangle$ values for Case I might seem surprising as one might have expected that the mean shear between the center jet and the annular flow in Case II would result in a larger cross-stream turbulent flux, and therefore faster decrease of $\langle\phi_1\rangle$. To understand this trend, we note that the total streamwise flux of the mean scalar across a cross-stream plane at any downstream location is conserved [61]. For $\langle\phi_1\rangle$ the total mean flux is identical for both cases. Therefore, a lower mean velocity generally will result in higher mean scalar values. The cross-stream mean velocity profile at the jet exit is wider (inferred from the jet exit profiles) for Case I, resulting in a slower decay of the centerline mean velocity. As a result, the mean scalar decreases faster than Case II in order to maintain the total streamwise mean flux. Therefore, at the local level although the mean shear between the center jet and the annular flow may result in larger turbulent advection (loss of $\langle\phi_1\rangle$) for Case II, it is more than compensated by the mean-flow advection, resulting in higher $\langle\phi_1\rangle$ values. The higher $\langle\phi_2\rangle$ values for Case I is likely due to larger turbulent advection. We will discuss this issue further along with the cross-stream profiles.

The scalar mean profiles on the jet centerline for the larger annulus show that ϕ_3 begins to reach the centerline at approximately $x/d = 7$, later than for the smaller annulus cases. Similarly to Cases I and II, $\langle\phi_1\rangle$ decreases faster for Case III than for Case IV. Here $\langle\phi_2\rangle$ reaches a maximum at approximately $x/d = 15$ for both larger annulus cases, again later than for the smaller annulus cases. There is more ϕ_3 (smaller $\langle\phi_1\rangle + \langle\phi_2\rangle$) on the centerline for Case III than for Case IV. The lower $\langle\phi_1\rangle + \langle\phi_2\rangle$ values are similar to those of $\langle\phi_1\rangle$, again due to the slower decay of the centerline velocity resulting in smaller mean-flow advection.

To examine the effects of the annulus width (the ϕ_2 length scale), we compare

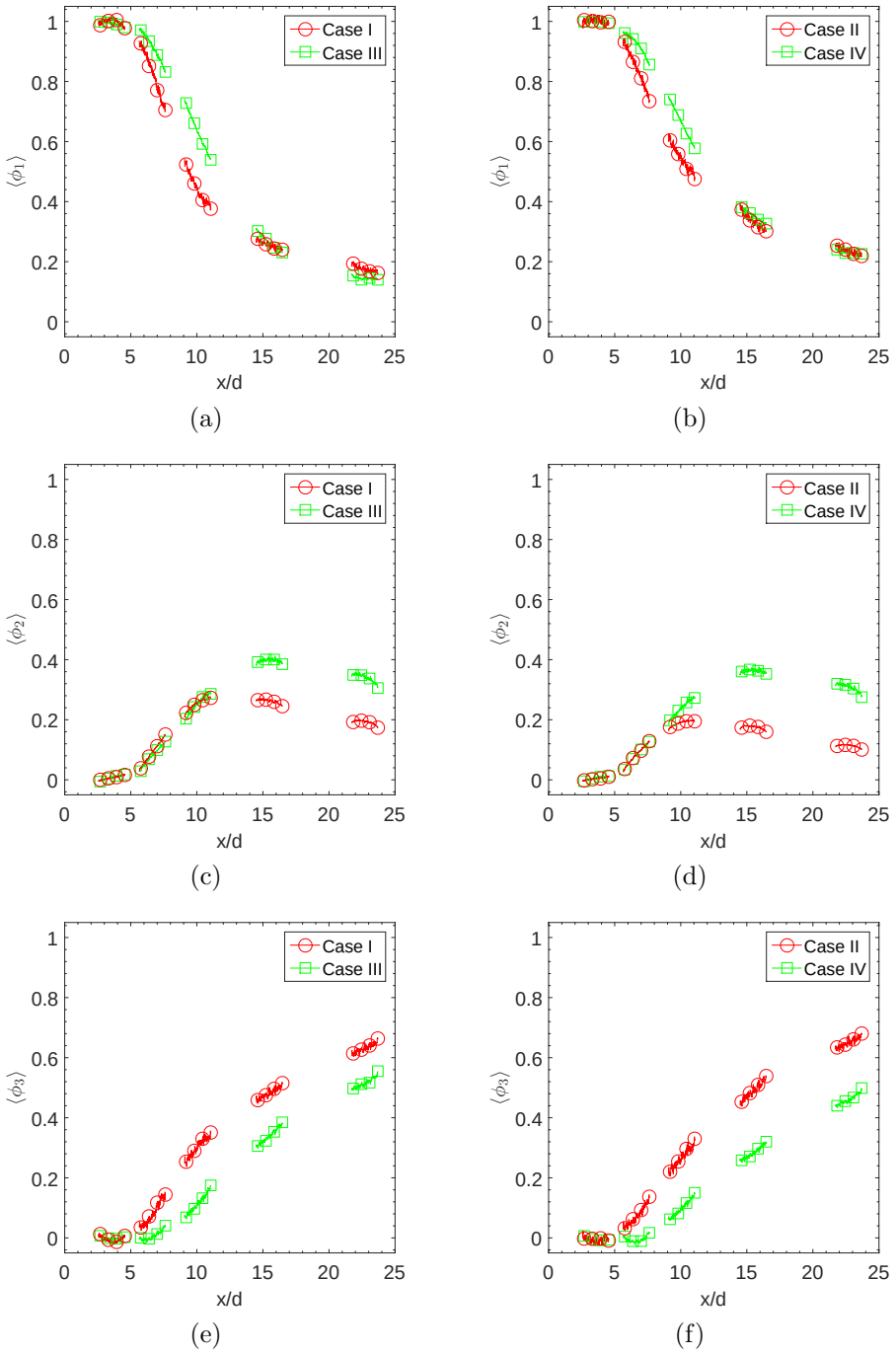

Figure 4.2: Comparisons of the centerline mean scalars between the smaller annulus and the larger annulus.

profiles for Cases I and III and for Cases II and IV (figure 4.2). The $\langle\phi_1\rangle$ values are larger for Case III than for Case I (figure 4.2a), probably because the shear layer between the annular flow and the co-flow is farther from the centerline, resulting in smaller cross-stream turbulent advection, although the mean advection is smaller for Case III. The $\langle\phi_2\rangle$ values are essentially the same for Cases I and III for $x/d < 12$ (figure 4.2c), likely a result of the competition between the opposite effects of the weaker velocity fluctuations, which tends to bring less ϕ_2 to the centerline, and the wider ϕ_2 stream, which tends to result in more ϕ_2 reaching the centerline. Further downstream ($x/d = 24$), $\langle\phi_1\rangle$ values are very close for Case I and Case III, and also for Case II and Case IV. However, $\langle\phi_2\rangle$ for the larger annulus are higher than for the smaller annulus, because the total $\langle\phi_2\rangle$ flux is larger for the larger annulus flows. Another effect of the larger annulus is that there is more ϕ_3 (smaller $\langle\phi_1\rangle + \langle\phi_2\rangle$) on the centerline for Case III than for Case IV, whereas the difference is much smaller between Case I and Case II.

The scalar rms profiles on the jet centerline for the smaller annulus are shown in figure 4.3a,b. The ϕ_1 rms fluctuations, $\sigma_1 = \langle\phi_1'^2\rangle^{\frac{1}{2}}$, reach the maximum values near $x/d = 7.5$ for both cases. The ϕ_2 rms fluctuations, $\sigma_2 = \langle\phi_2'^2\rangle^{\frac{1}{2}}$, reach the maximum values at a larger x/d value for Case I than Case II. The maximum values of both σ_1 and σ_2 are larger for Case I than for Case II. This might be a result of the larger production rates for Case I, in which the cross-stream scalar mean gradients are larger for both scalars (figure 4.13). At $x/d = 21$, σ_1 is slightly smaller while σ_2 is slightly larger for Case I. This trend is also consistent with the relative magnitudes of the scalar mean profiles (and gradients). At this downstream location ϕ_1 and ϕ_2 are already very well mixed; therefore, the relative magnitudes of the rms fluctuations should be consistent with those of the relative values of the mean scalars.

The scalar rms fluctuations for the larger annulus reach the maximum values

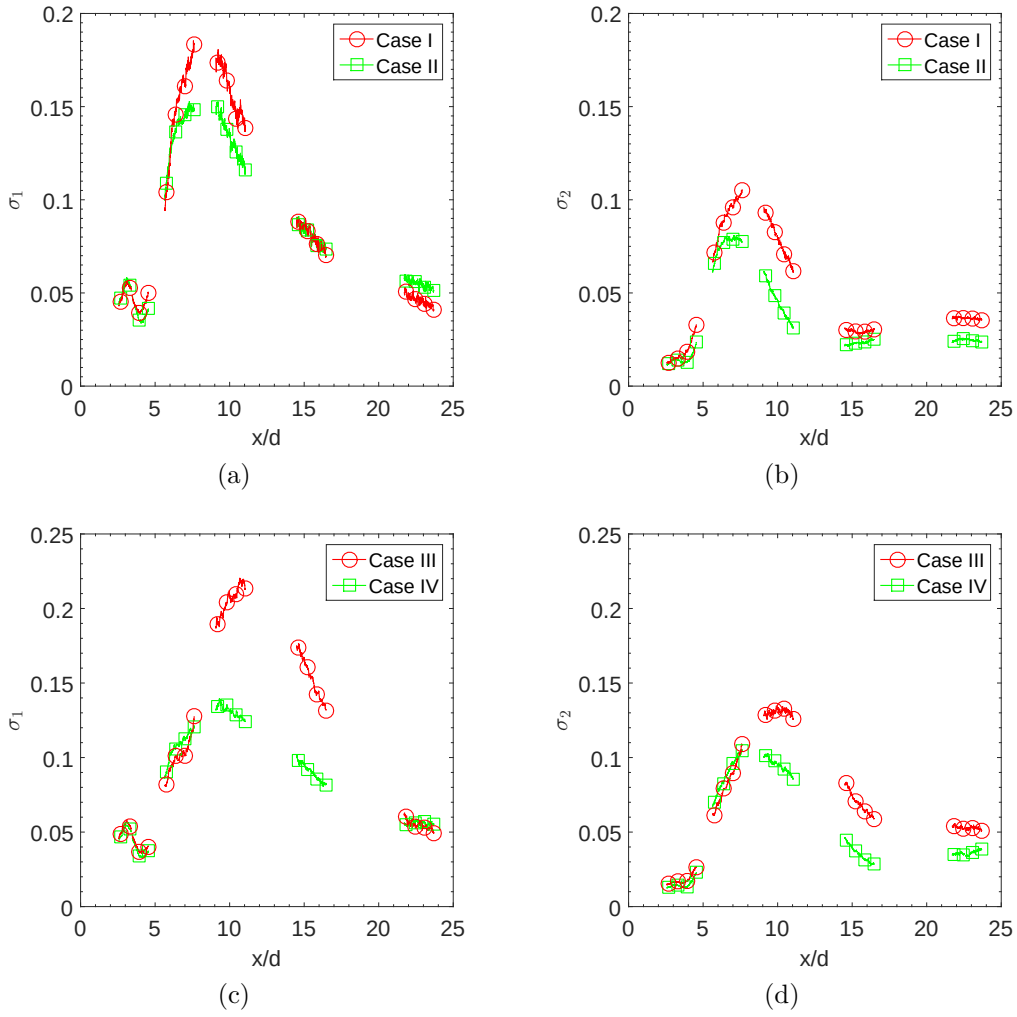

Figure 4.3: Evolution of the rms fluctuations on the jet centerline.

at larger x/d values for Case III than for Case IV (figure 4.3c,d), since there is no mean shear between the center stream and the annular stream for Case III. Similar to the relative magnitudes between Case I and Case II, the maximum values of both σ_1 and σ_2 are larger for Case III than for Case IV, again a result of larger production for Case III. The ϕ_2 rms profiles appear to have minimum values near $x/d = 18$, after which the values increase slightly, due to the inward shifting of the two off-centerline peaks of the cross-stream ϕ_2 rms profiles (figure 4.15). We will further discuss these results along with cross-stream rms profiles.

Comparisons between Cases I and III, and between Cases II and IV show that an increased annulus width generally pushes the locations of the peak rms values further downstream (figure 4.4). This trend is expected because it takes longer for the scalars to mix for the larger annulus width. The maximum values for both σ_1 and σ_2 are generally larger for the larger annulus cases except that the peak value of σ_1 is slightly smaller for Case IV compared to Case II. The increased length scale of annulus also reduces the decay rate of the scalar fluctuations beyond the peak locations, a trend similar to that of Sirivat & Warhaft [58].

The fluctuation intensities, $\frac{\sigma_1}{\langle\phi_1\rangle}$ and $\frac{\sigma_2}{\langle\phi_2\rangle}$, on the jet centerline for the smaller annulus are shown in figure 4.5a,b. The evolution of the fluctuation intensity of ϕ_1 is quite different for the two cases. It reaches a peak before decreasing toward an asymptotic value for Case I, whereas it appears to have reached the asymptotic value at approximately $x/d = 9$ for Case II. The asymptotic values for both cases appear to be the same, however. The faster approach to the asymptotic value for Case II suggests faster ϕ_1 mixing, due to the presence of mean shear between the center stream and the annular stream. The ϕ_2 fluctuation intensity decreases rapidly for $x/d < 14$, after which it appears to increase slightly, due to the mild increase of σ_2 on the centerline. It is slightly larger for Case I than Case II when $x/d < 11$, and

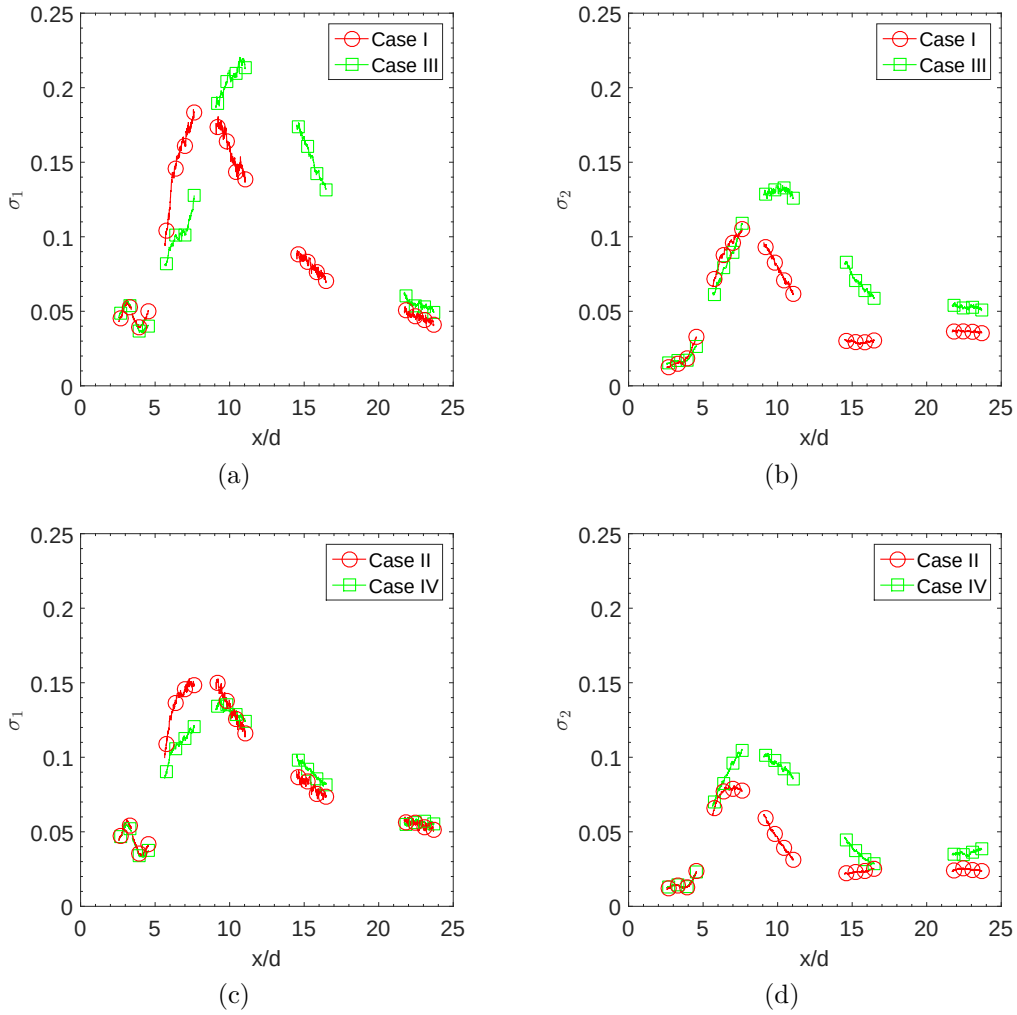

Figure 4.4: Comparisons of the centerline rms fluctuations between the smaller annulus and the larger annulus.

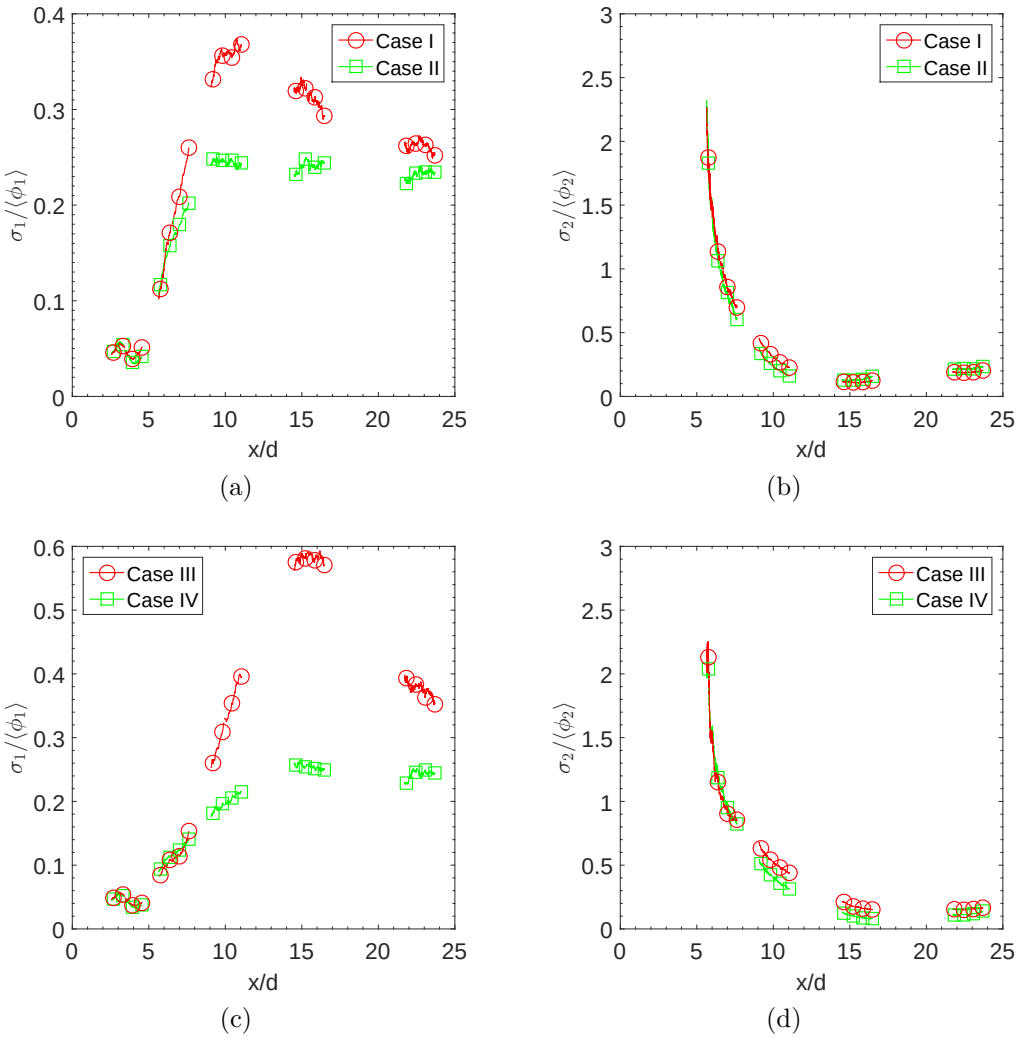

Figure 4.5: Evolution of the scalar fluctuation intensities on the jet centerline.

becomes approximately equal (the asymptotic value) for the two cases for $x/d > 14$, much earlier than that of ϕ_1. This trend is probably due to the smaller initial length scale of ϕ_2 (the annulus width is much smaller than the center jet diameter).

The centerline fluctuation intensities for the larger annulus are shown in figure 4.5c,d. Similar to Case I, the ϕ_1 fluctuation intensity reaches the maximum value near $x/d = 16$ for Case III before beginning to decrease. It is still decreasing at the furthest downstream measurement location, and appears to decrease to the same asymptotic value as that of Case IV. The ϕ_1 fluctuation intensity for Case IV increase monotonically until it reaches the asymptotical value, which is similar to Case II. Again, the overshoot is a result of poor ϕ_1 mixing for Case III. Similar to the smaller annulus, the ϕ_2 fluctuation intensity for the larger annulus decreases rapidly when $x/d < 15$, after which it appears to increase slightly. Similar to Cases I and II, the ϕ_2 fluctuation intensity decreases toward its asymptotical value slightly slower for Case III than Case IV.

Comparisons between profiles of different annulus widths show that the fluctuation intensities approach the asymptotical values further downstream with increased annulus width, while it appears that the asymptotic values are the same for all four cases (figure 4.6). The peak value of the ϕ_1 fluctuation intensity for Case III is larger than for Case I, consistent with the observation that larger amounts of scalars need to be mixed for the larger annulus width.

Different from the scalar mean and rms, which characterize individual scalar fields, the correlation coefficient between ϕ_1 and ϕ_2 fluctuations, $\rho = \frac{\langle \phi_1' \phi_2' \rangle}{\sigma_1 \sigma_2}$, is a measure of the extent of (molecular) mixing between the scalars. For the smaller annulus (figure 4.7a), the correlation coefficient equals negative one close to the jet exit since there is no co-flow air. It begins to increase downstream and reaches the maximum value earlier for Case II than Case I, indicating that the mean shear between

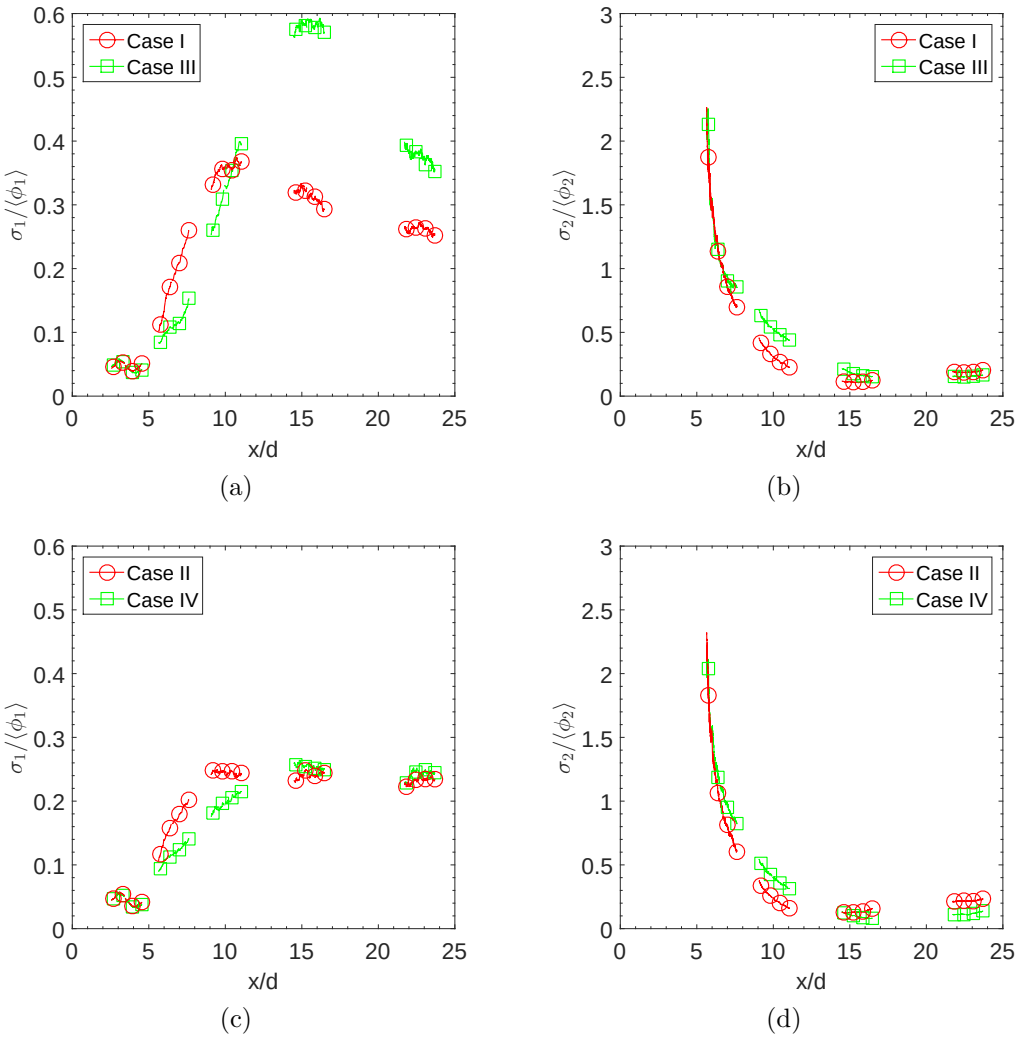

Figure 4.6: Comparisons of the centerline fluctuation intensities between the smaller annulus and the larger annulus.

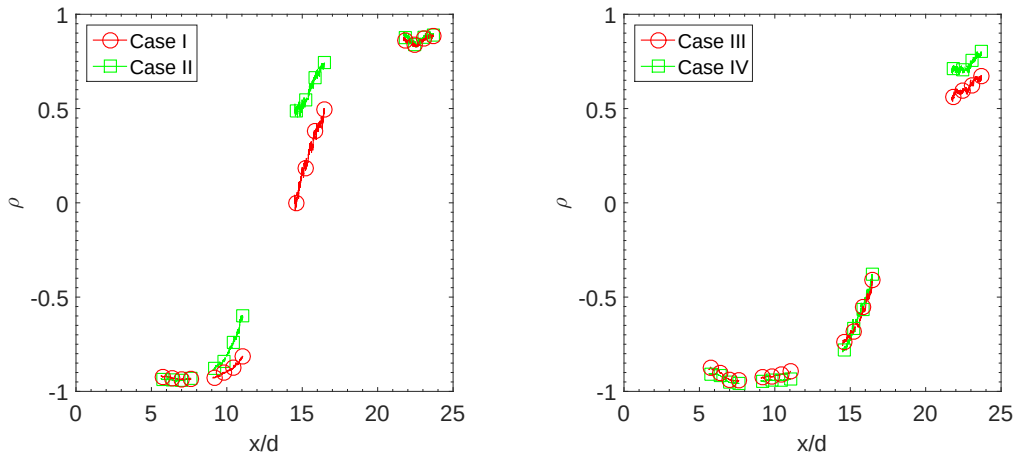

(a) (b)

Figure 4.7: Evolution of the correlation coefficient between ϕ_1 and ϕ_2 on the jet centerline.

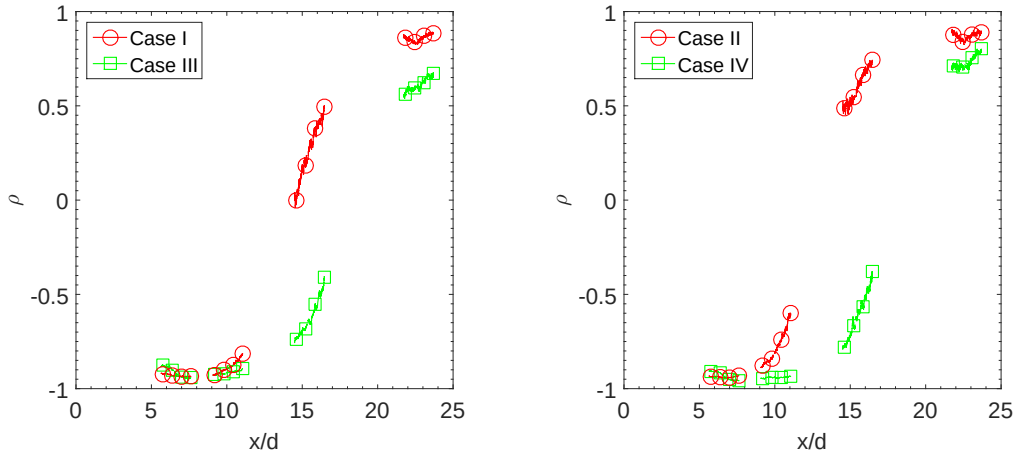

(a) (b)

Figure 4.8: Comparisons of the centerline correlation coefficient between the smaller annulus and the larger annulus.

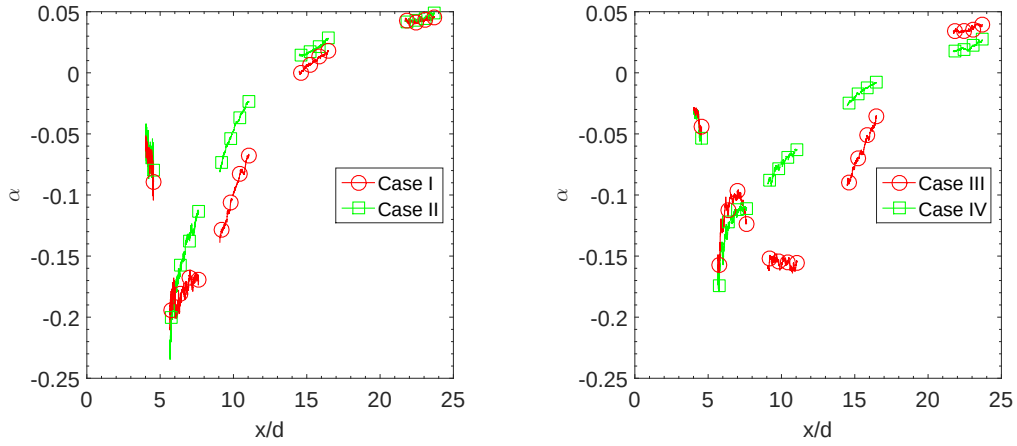

Figure 4.9: Evolution of the segregation parameter between ϕ_1 and ϕ_2 on the jet centerline.

the center jet and the annular flow enhances mixing. The correlation coefficient for the larger annulus cases (figure 4.7b) is still increasing at the furthest downstream measurement location. However, it appears that it would reach the value of unity earlier for Case IV than Case III, again reflecting the faster mixing between ϕ_1 and ϕ_2 due to the mean shear between the two streams. The correlation coefficient profiles for the small annulus begin to increase and reach the maximum value at smaller downstream locations than for the larger annulus (figure 4.8), indicating that the mixing between ϕ_1 and ϕ_2 is faster with the smaller annulus width.

The segregation parameter, $\alpha = \frac{\langle \phi_1' \phi_2' \rangle}{\langle \phi_1 \rangle \langle \phi_2 \rangle}$, is also a measure of the extent of mixing between the scalars. Its evolution on the jet centerline is non-monotonic (figure 4.9a). It is close to zero near the jet exit [6]. It then becomes negative before increasing to positive values for the smaller annulus cases. For both Cases I and II, it appears to approach the same asymptotic value far downstream. Similar to the trend of ρ, α for Case II begins to increase and reaches the asymptotic value at smaller downstream locations than for Case I, again because mixing of ϕ_1 and ϕ_2 is enhanced by the mean shear between the center stream and the annular flow. However, α

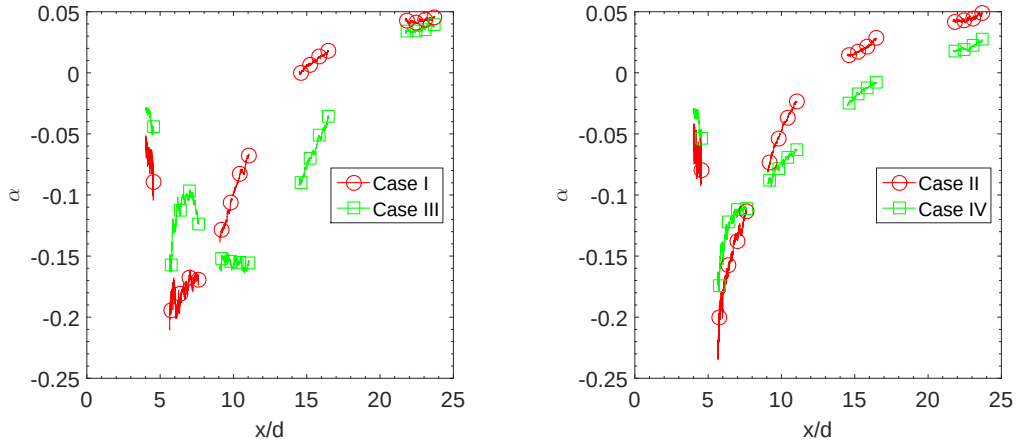

Figure 4.10: Comparisons of the centerline segregation parameter between the smaller annulus and the larger annulus.

(figure 4.9b) for Case III reaches the asymptotic value earlier than for Case IV. Here the evolution of α for Case III is quite different from the other cases. It first decreases from zero to a minimum value. It then increases to a value of approximately -1 near $x/d = 7$, after which it decreases again, reaching another minimum at about $x/d = 10$ before increasing again further downstream and approaching an asymptotic value. Comparing the results for the two annulus widths (figure 4.10), the asymptotic values appear to be approximately equal for all four cases. However, the smaller annulus profiles reach the asymptotic value faster than the larger annulus.

The evolution of the scalar JPDF of ϕ_1 and ϕ_2 on the jet centerline for Cases I and II is shown in figure 4.11. The JPDF in the ϕ_1-ϕ_2 space should be confined to a triangle with the vertices at (1,0), (0,1) and (0,0), representing pure ϕ_1, ϕ_2 and ϕ_3, respectively. The straight line connecting (1,0) and (0,1) represents the ϕ_1-ϕ_2 mixing line. At $x/d = 3.29$, the JPDF is largely concentrated near (1, 0) in the scalar space because only pure ϕ_1 is present there. The broadening of the JPDF here is due to measurement uncertainties including noise. The JPDF begins to extend towards (0, 1) along the ϕ_1-ϕ_2 mixing line at $x/d = 4.31$ as ϕ_2 reaches the centerline and begin

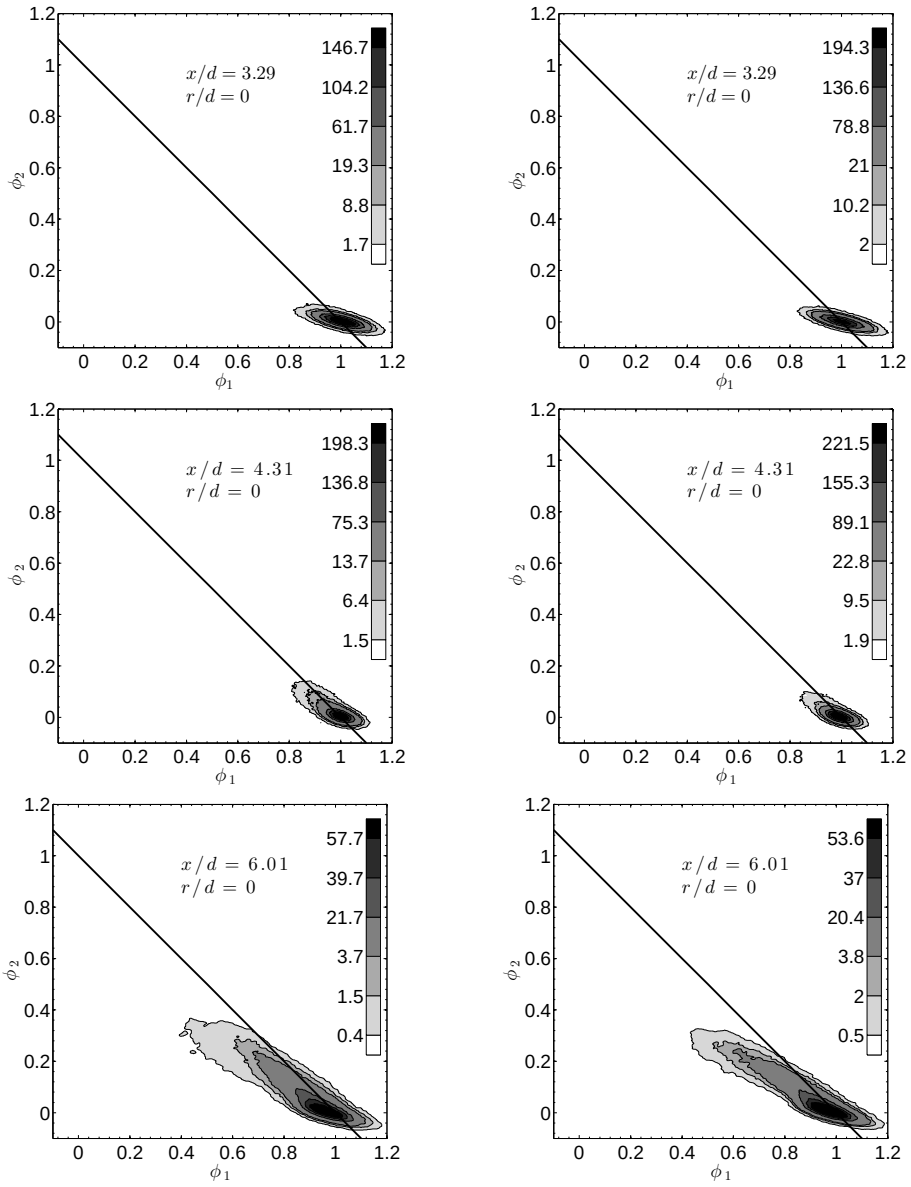

Figure 4.11: Evolution of the scalar JPDF on the jet centerline for Case I (left) and Case II (right). The downstream locations are listed in the top of each figure. The last three contours correspond to boundaries within which the JPDF integrates to 90%, 95%, and 99%, respectively throughout this work. The rest of the contours scale linearly over the remaining range.

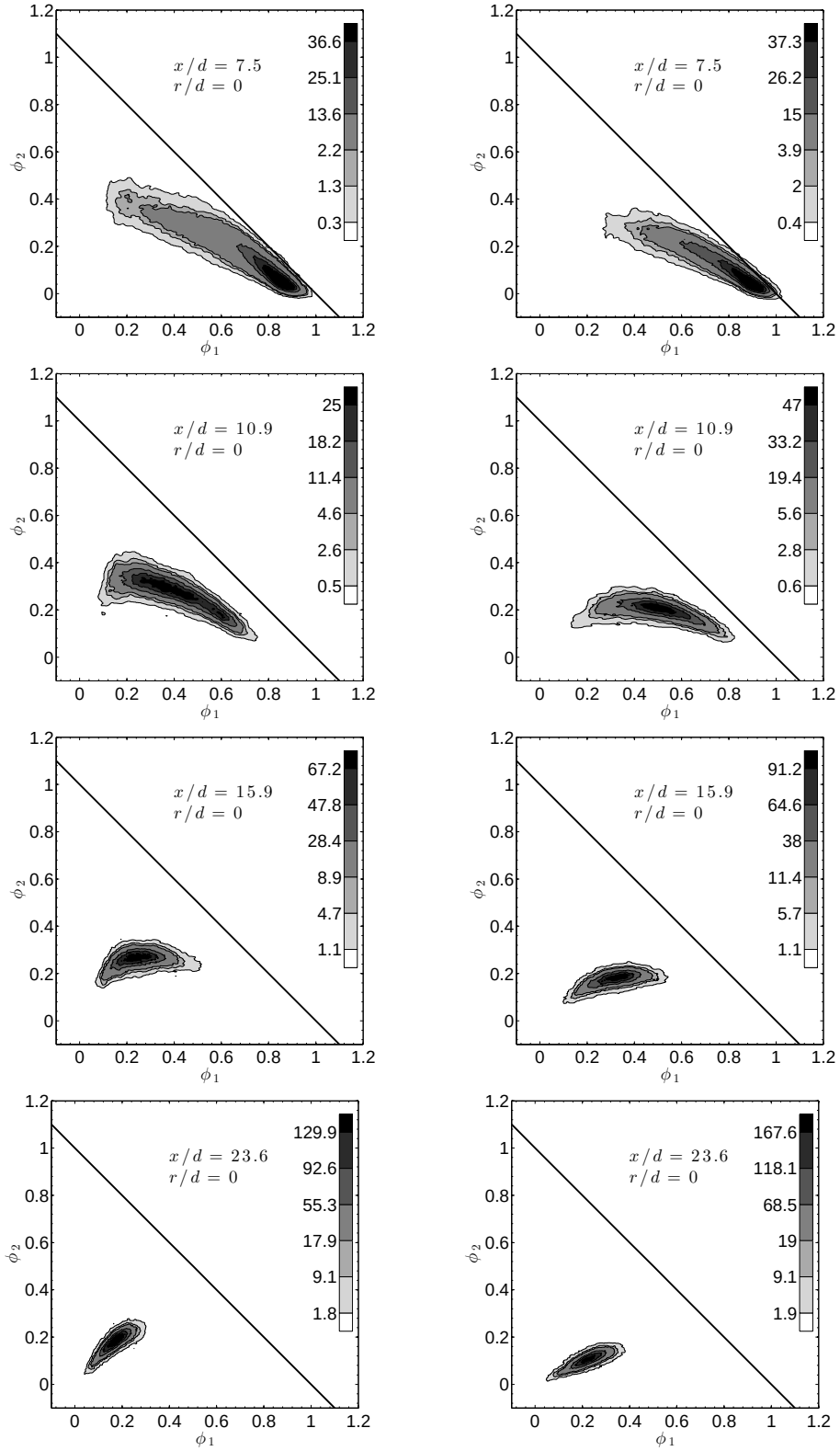

Figure 4.11: (Continued.)

to mix with ϕ_1. At $x/d = 6.01$, the JPDF extends further towards (0, 1) and the tail begins to bend towards (0, 0), which is a result of the presence of ϕ_3 on the centerline. As the downstream distance further increases, the JPDF bends further toward (0, 0). At $x/d = 7.5$, the JPDF area is significantly larger and extends further away from (1,0) for Case I than for Case II, due to the stronger large-scale transport in physical space by the conditional velocity for Case I. Note that transport of the JPDF can result in both production and transport of the scalar variance. The movement of the peak of JPDF towards smaller ϕ_1 values is faster for Case I, consistent with the evolution of the scalar mean, which is primarily due to the mean-flow advection. At $x/d = 10.9$, the ridgeline of the JPDF is almost horizontal for Case II, while it still has a negative slope for Case I. The shapes of the JPDFs are quite different for the two cases. For Case I the JPDF has a somewhat triangular shape, while for Case II the JPDF has a slender shape. There are larger fluctuations of ϕ_2 and ϕ_3 on the LHS of the JPDF for Case I, due to the stronger transport caused by the strong mean shear. The JPDF for Case II extends less than for Case I, suggesting better mixing of ϕ_1 due to the mean shear between the center jet and the annular flow. Thus, mixing is occurring in a mixture with relatively uniform ϕ_2 but large fluctuations of ϕ_1 and ϕ_3. Moving further downstream ($x/d = 15.9$), the ridgeline of the JPDF begins to have a positive slope and moves closer to (0,0). At $x/d = 23.6$, ϕ_1 and ϕ_2 are well correlated. The extent of the JPDF in the ϕ_1 direction is larger for Case II than for Case I, while the extent in the ϕ_2 direction is smaller. The differences in the slopes of the JPDF ridgelines reflect different values of the initial ϕ_2 flux.

The evolution of the scalar JPDF of ϕ_1 and ϕ_2 on the jet centerline for Cases III (figure 4.12) is qualitatively similar to Case I, while that of Case IV is similar to Case II. The JPDF extends much further along the ϕ_1-ϕ_2 mixing line before bending toward (0,0) for the larger annulus than for the smaller annulus, because the larger

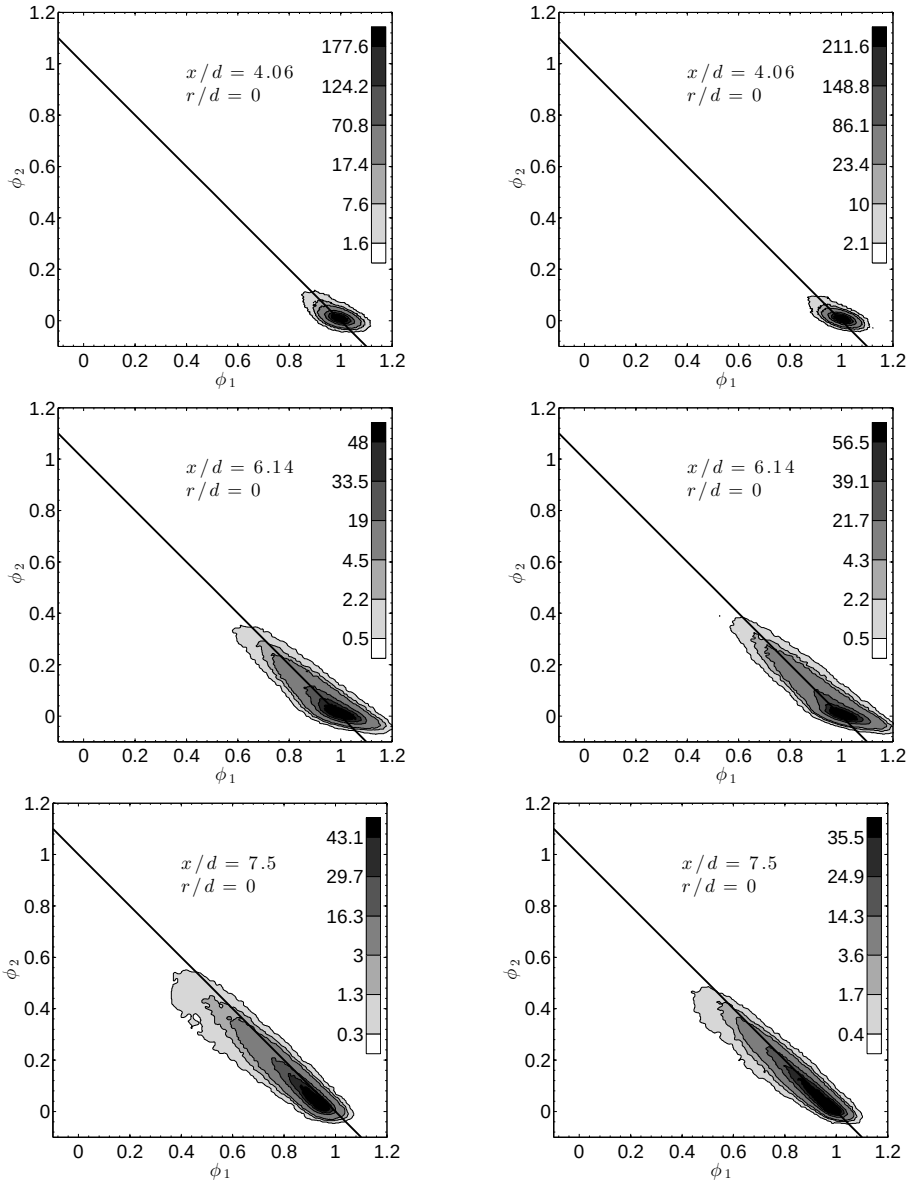

Figure 4.12: Evolution of the scalar JPDF on the jet centerline for Case III (left) and Case IV (right).

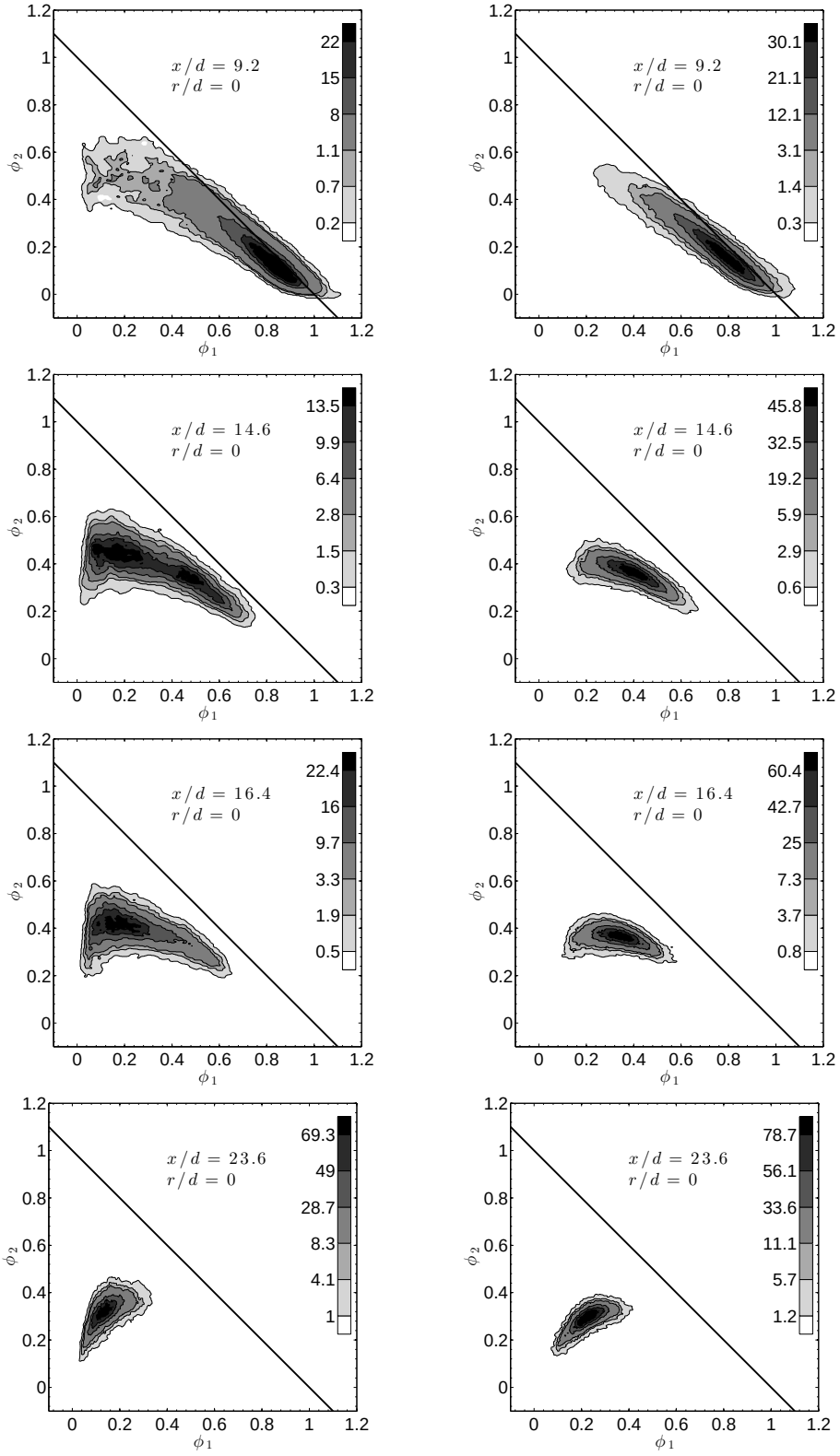

Figure 4.12: (Continued.)

annulus width keeps the co-flow air from reaching the centerline. A major difference between the two cases is that at $x/d = 14.6$, the JPDF for Case III is bimodal with peaks at approximately (0.18,0.48) and (0.5,0.4). The latter mixture is mostly a ϕ_1-ϕ_2 mixture, which likely comes from the ϕ_1-ϕ_2 mixing layer, while the former is mostly a ϕ_2-ϕ_3 mixture coming from the ϕ_2-ϕ_3 mixing layer, which still contains large ϕ_2 fluctuations due to the strong turbulent transport. The two mixtures are unmixed due to the large annulus width and the lack of mean shear between the ϕ_1-ϕ_2 streams, and are transported by the large-scale velocity fluctuations (flapping), resulting in the bimodal JPDF. At $x/d = 14.6$ for Case IV, the JPDF is unimodal with the peak at (0.4,0.4), which is a relatively well mixed mixture of ϕ_1, ϕ_2 and ϕ_3, although the amount of ϕ_3 is not large. Here, ϕ_1 is better mixed with ϕ_2 for Case IV than for Case III, consistent with the earlier onset of mixing between ϕ_1 and ϕ_3, probably because the mean shear on both sides of the annular stream is able to overcome the large annulus width to enhance mixing between ϕ_1 and ϕ_3. We note that while figure 4.7 shows that the values of the correlation coefficient between ϕ_1 and ϕ_2 are nearly equal for Cases III and IV at $x/d = 14.6$, the JPDF shows that the states of mixing have some qualitative differences for these cases, an indication of the limitation of the correlation coefficient in representing the state of mixing, especially when it is small or negative. At $x/d = 16.4$, the JPDF becomes unimodal for Case III. Moving further downstream, the JPDF has a positive slope. However, it still has a tail bending toward (1,0) at $x/d = 23.6$.

While the lack of mean shear between the ϕ_1-ϕ_2 streams results in a bimodal JPDF for Case III at $x/d = 14.6$, it does not do so for Case I. The peak of the JPDF at $x/d = 14.6$ for Case I is at (0.25,0.28), which is essentially a well mixed mixture of ϕ_1, ϕ_2 and ϕ_3, because for the smaller annulus width ϕ_3 is able to reach the centerline due to the smaller distance. For Case III (with the larger annulus width) the mixing

between ϕ_1 and ϕ_3 is slower, because they have to be mixed with ϕ_2 separately before they begin to mix with each other.

4.2 Cross-stream profiles

The cross-stream scalar mean profiles for the smaller annulus are shown in figure 4.13a,b. The $\langle\phi_1\rangle$ profiles are narrower and the $\langle\phi_1\rangle$ values are generally smaller for Case I than for Case II. The maximum slopes of the profiles, however, are larger for Case I. These differences are primarily because of the different annular flow velocity. The larger streamwise mean velocity of the annular flow for Case I results in smaller $\langle\phi_1\rangle$ values to maintain a constant total $\langle\phi_1\rangle$ flux.

The cross-stream $\langle\phi_2\rangle$ profiles have off-centerline peaks, at approximately the same locations for both cases at the upstream location ($x/d = 3.29$). The $\langle\phi_2\rangle$ values are larger for Case I than for Case II at all radial locations. The spread of $\langle\phi_2\rangle$ for Case I is also slower. These trends are because the mean velocity downstream of the annulus decreases faster for Case I than Case II, leading to slower decrease of $\langle\phi_2\rangle$ in order to maintain a constant streamwise $\langle\phi_2\rangle$ flux. Thus, while the total streamwise $\langle\phi_2\rangle$ flux at the jet exit for Case I is larger than Case II due to larger annulus velocity, this difference is not the cause of the higher $\langle\phi_2\rangle$ value. Figure 4.13b also shows that the mean gradient of $\langle\phi_2\rangle$ on the LHS (closer to the centerline) of the peak is larger than the RHS for Case I, whereas the difference between the slopes is smaller for Case II. This reflects the difference in the mean shear for the two cases. The annular stream has mean shear on both sides for Case II whereas there is no significant mean shear on the LHS for Case I, resulting in larger $\langle\phi_2\rangle$ gradients. Moving downstream, the peak location shifts inward until the peaks on both sides merge at the centerline.

The general trends for the cross-stream scalar mean profiles for the larger

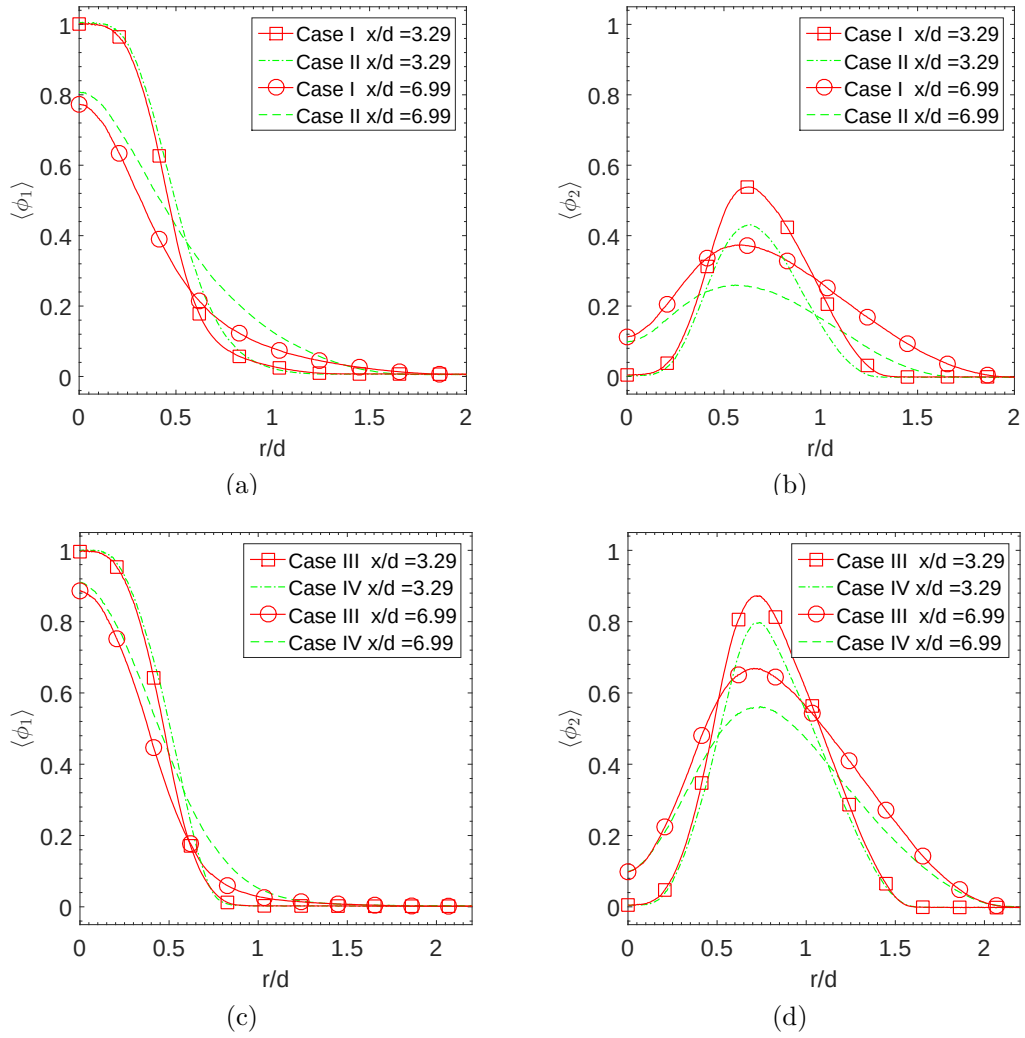

Figure 4.13: Cross-stream scalar mean profiles. The downstream locations are given in the legend.

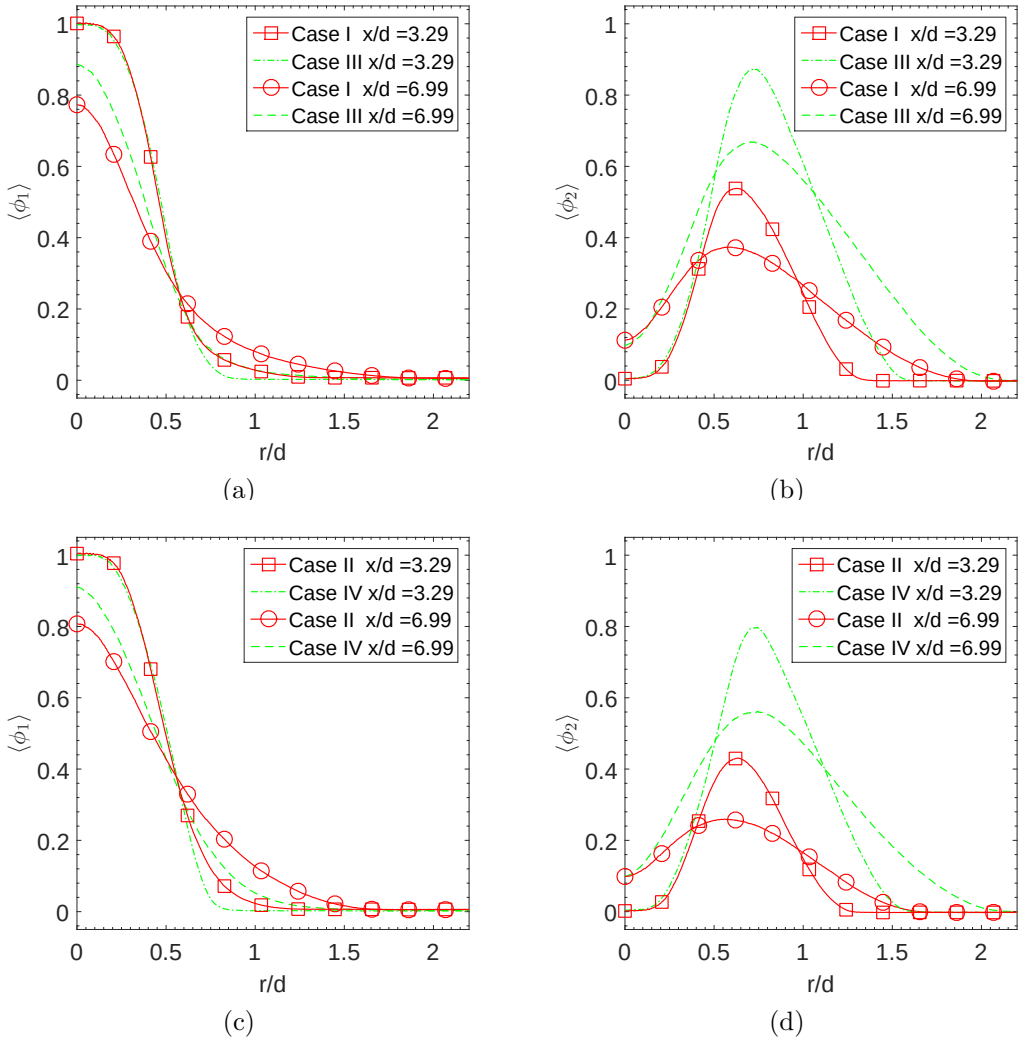

Figure 4.14: Comparisons of the cross-stream mean scalars between the smaller annulus and the larger annulus.

annulus (figure 4.13c,d), are similar to those of the smaller annulus. Comparisons between the smaller annulus and the larger annulus (figure 4.14) show that the $\langle\phi_1\rangle$ values at $x/d = 3.29$ are nearly equal for Cases I and III (and for II and IV) for $r/d < 0.6$, beyond which Case I (II) is larger. At $x/d = 6.99$, $\langle\phi_1\rangle$ is smaller for Case I (II) than Case III (IV) for $r/d < 0.6$, and is larger beyond. The spread of the $\langle\phi_1\rangle$ is faster for the smaller annulus width, suggesting that the large-scale turbulent transport is likely stronger for Case I (II) than for Case III (IV). The $\langle\phi_2\rangle$ peak values are generally lower for the smaller annulus, again due to the stronger turbulent transport.

The cross-stream profiles of the ϕ_1 rms fluctuations have off-centerline peaks (figure 4.15a). At $x/d = 3.29$ σ_1 peaks at the same location ($r/d = 0.45$) for both Cases I and II. Further downstream the peak location shifts inward (to $r/d = 0.3$ at $x/d = 6.99$). The σ_1 peak value is larger for Case I, which is likely a result of the larger production rate of σ_1^2 as the mean scalar gradient is larger for Case I. The σ_1 profile is narrower for Case I than for Case II, consistent with the widths of the mean scalar profiles. The peak value of σ_1 for Case I is 13% larger than Case II at $x/d = 3.29$ while it is 26% larger at $x/d = 6.99$. The faster decay of σ_1 for Case II suggests faster mixing of ϕ_1 due to the mean shear between the center stream and the annular stream. For the larger annulus (figure 4.15c), the peak values of the ϕ_1 rms fluctuations are generally larger for Case III than Case IV, again a result of larger production for Case III. The peak value increases by about 10% from $x/d = 3.29$ to $x/d = 6.99$ for Case III whereas it decreases by about 10% for Case IV, suggesting that the ϕ_1 field is still in the early stages of development for Case III, probably because the large mean shear results in stronger velocity fluctuations and a slower transition to fully developed turbulence.

There are two off-centerline peaks for each cross-stream ϕ_2 rms profile (figure

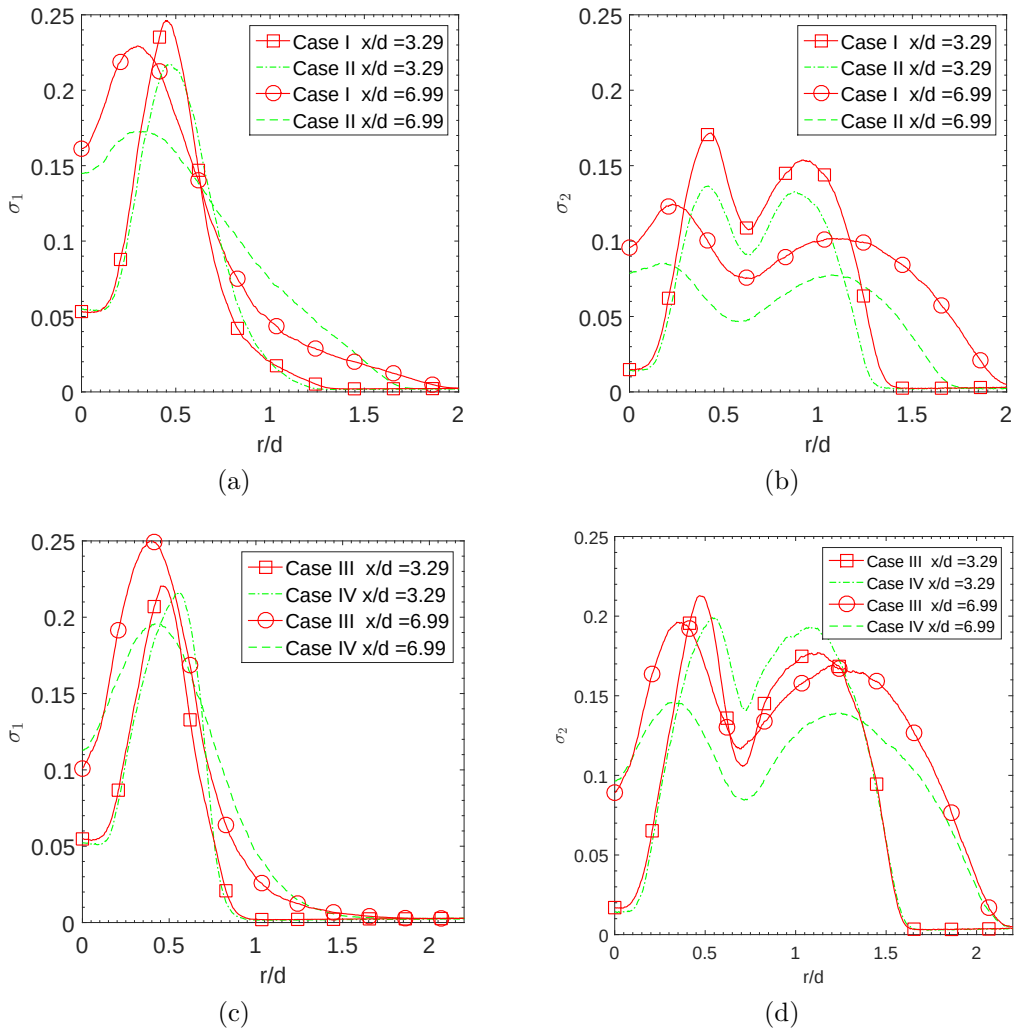

Figure 4.15: Cross-stream scalar rms profiles. The downstream locations are given in the legend.

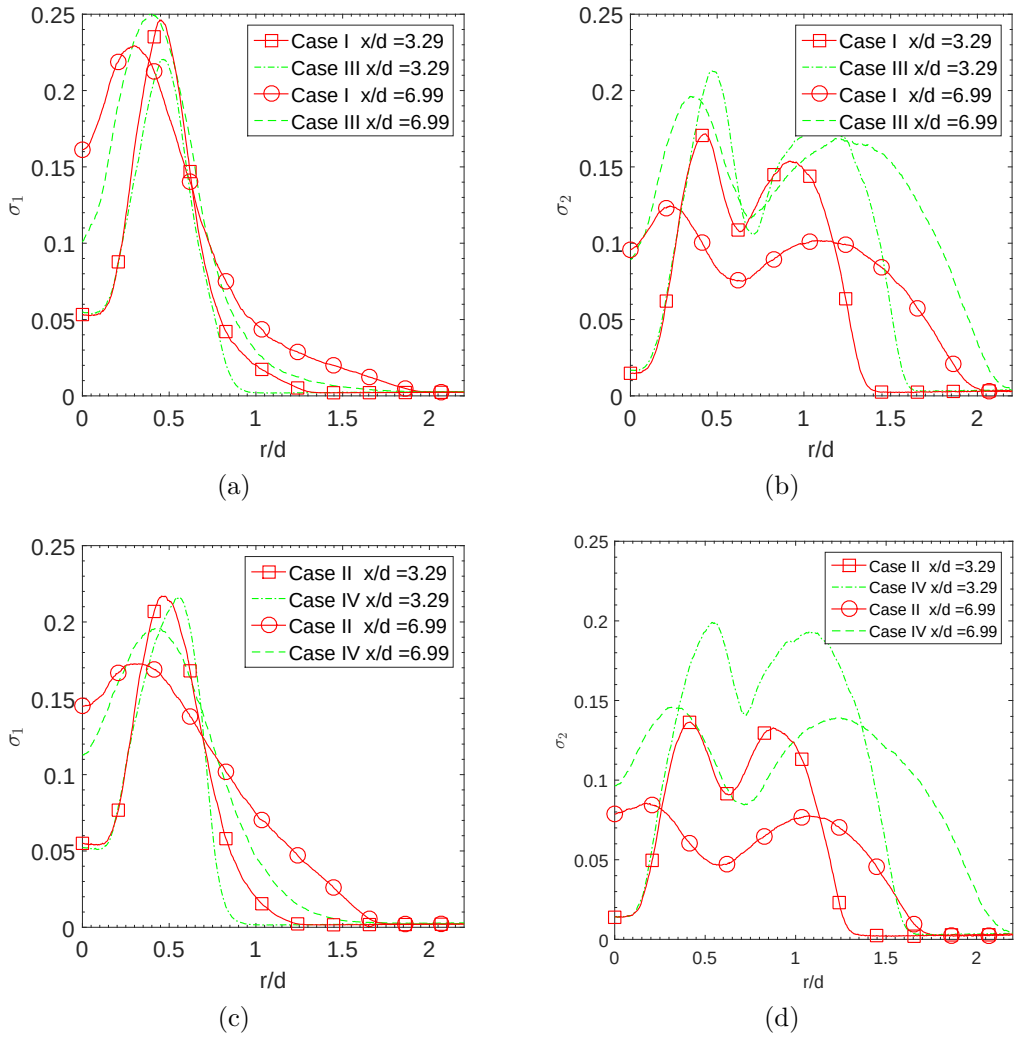

Figure 4.16: Comparisons of the cross-stream rms fluctuations between the smaller annulus and the larger annulus.

4.15b), one located on each side of the peak of the $\langle\phi_2\rangle$ profile. The peak locations are essentially the same for Cases I and II at both $x/d = 3.29$ and $x/d = 6.99$. Similar to σ_1, the σ_2 values are generally larger for Case I than for Case II, consistent with larger mean scalar gradients, which would result in a larger production rate of σ_2^2 for Case I. The value of the left peak (close to centerline) is larger than that of the right peak (away from the centerline) for Case I, while the two peak values are very close for Case II. These results are again consistent with the magnitudes of the mean scalar gradient. Therefore, the ϕ_2 mixing process in the two mixing layers are more similar when there are mean shear on both sides of the annular flow. Similar to σ_1, the peak value of σ_2 decays faster for Case II, indicating faster ϕ_2 mixing for Case II. For the larger annulus (figure 4.15d), the peak values of the σ_2 profiles are larger for Case III than for Case IV except the right peak at $x/d = 3.29$. The inward shift of the left peak location for Case III is slower than for Case IV, while the outward shift of the right peak location is similar for the two cases. The slower inward shift suggests slower mixing between ϕ_1 and ϕ_2 for Case III due to the lack of mean shear between the center stream and the annular stream. We note that the downstream evolutions of the peaks and the minimum between them are responsible for the non-monotonic centerline profile of σ_2 for $x/d > 11$ (figure 4.3): the inward shift of the left peak and the minimum causes σ_2 to increase and then decrease. The broadening of the right peak eventually causes σ_2 to increases again on the centerline.

The above results also show that the progression of the mixing process is faster for the smaller annulus, with generally smaller peak values (figure 4.16). The peak value of σ_1 decreases from $x/d = 3.29$ to $x/d = 6.99$ for Case I whereas it is still increasing for Case III. The decay rate of σ_2 is larger for the smaller annulus. The σ_2 peak value decreases by about 23% for Case II whereas it decreases only 11% for Case IV. The peak locations also shift (inward and outward for the left and right

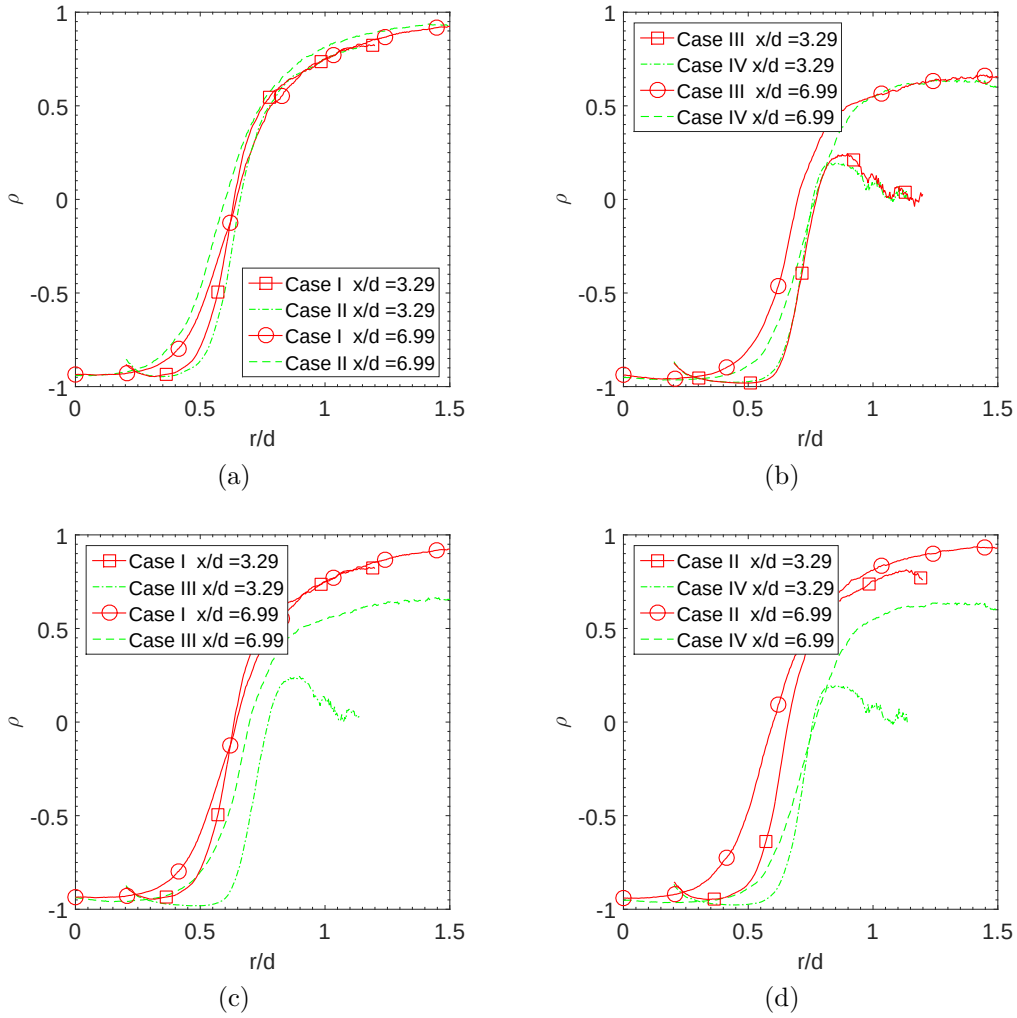

Figure 4.17: Cross-stream profiles of the scalar correlation coefficient. The downstream locations are given in the legend.

peak, respectively) much faster for the smaller annulus.

The cross-stream profiles of the correlation coefficient are shown in figure 4.17. The correlation coefficient generally has the value of negative one close to the centerline, increasing toward unity far away from the centerline. Close to the centerline, ϕ_1 and ϕ_2 are anti-correlated ($\rho \approx -1$) because there is virtually no ϕ_3. It begins to increase when ϕ_1 and ϕ_2 begin to mix with ϕ_3, and approaches unity far away from the centerline, indicating that the two scalars are well mixed and their fluctuations

are in phase. At $x/d = 3.29$, the slight increase (from -1) toward the centerline is due to the measurement noise, because the composition is mostly pure ϕ_1 with very small fluctuations. For the larger annulus, the profile begins to decrease at $r/d = 0.9$, also due to the measurement noise, because the composition is mostly pure ϕ_3. The differences between Cases I and II and between Cases III and IV are small. As discuss in section 4.3, there are significant differences among the JPDFs and conditional diffusion for the cases, again an indication of the limitations of the correlation coefficient in representing the state of mixing. Comparisons between Cases I and III and between Cases II and IV show that the evolution of the correlation coefficient is much slower for the larger annulus than for the smaller annulus.

The cross-stream profiles of the segregation parameter are shown in figure 4.18. The segregation parameter is negative close to the centerline because ϕ_1 and ϕ_2 are negatively correlated (It is zero on the centerline very close to the jet exit). For both Cases I and II at $x/d = 3.29$, α has minima near $r/d = 0.4$, after which it increase monotonically and has positive values far away from the centerline. At $x/d = 6.99$, there is a minimum near $r/d = 0.2$ for Case I whereas it increases monotonically from the centerline for Case II. Away from the centerline ($r/d > 0.7$), the α values are smaller at $x/d = 6.99$ than at $x/d = 3.29$ for both Cases I and II, consistent with the degrees of the progression of mixing. The α values are generally larger for Case I than Case II when $r/d > 0.8$, probably because the mixing between ϕ_1 and ϕ_2 is slower for Case I. For the larger annulus, the profiles generally have off-centerline minima. The difference between Case III and Case IV are small. Comparisons between Cases I and III and between Cases II and IV show that α increases faster for the smaller annulus.

The cross-stream profiles of the mean scalar dissipation rates and mean cross-dissipation rate for the smaller annulus are shown in figure 4.19a,c,e. The general

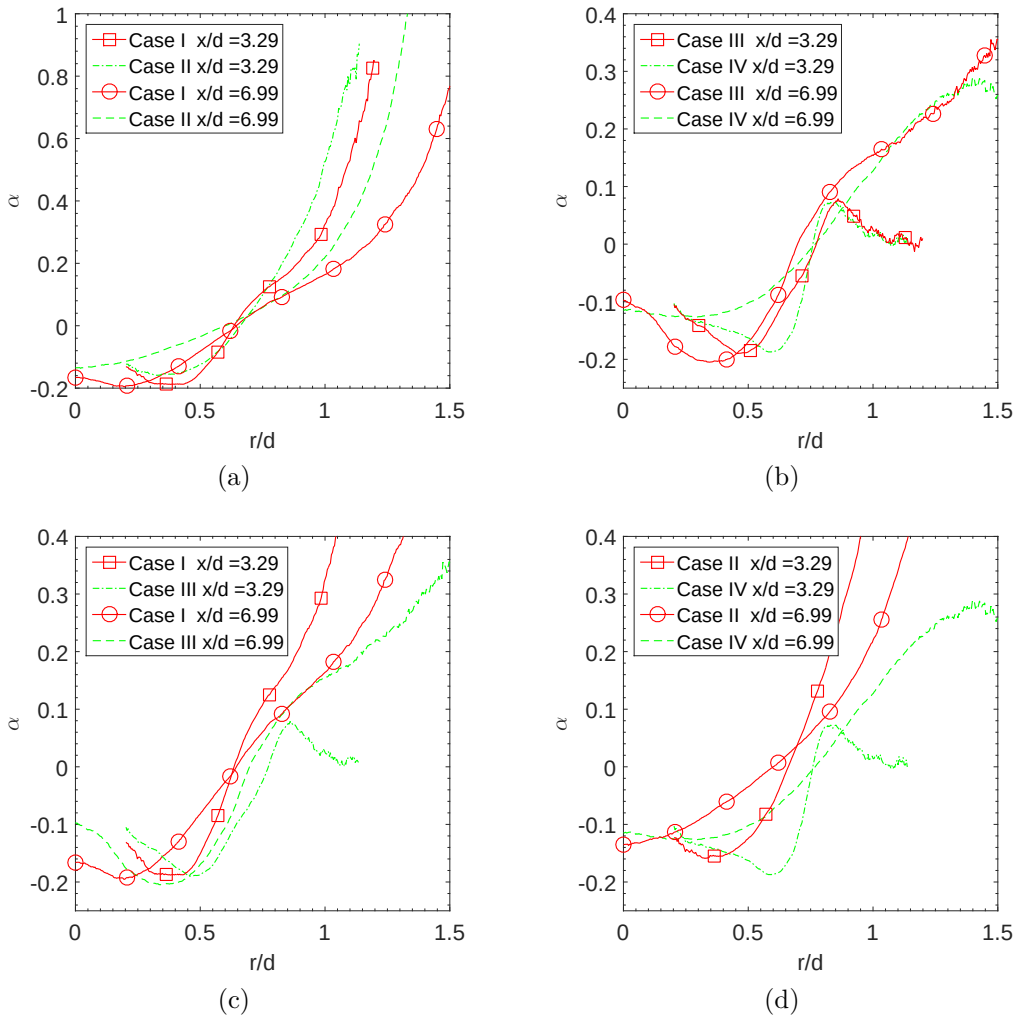

Figure 4.18: Cross-stream profiles of the segregation parameter. The downstream locations are given in the legend.

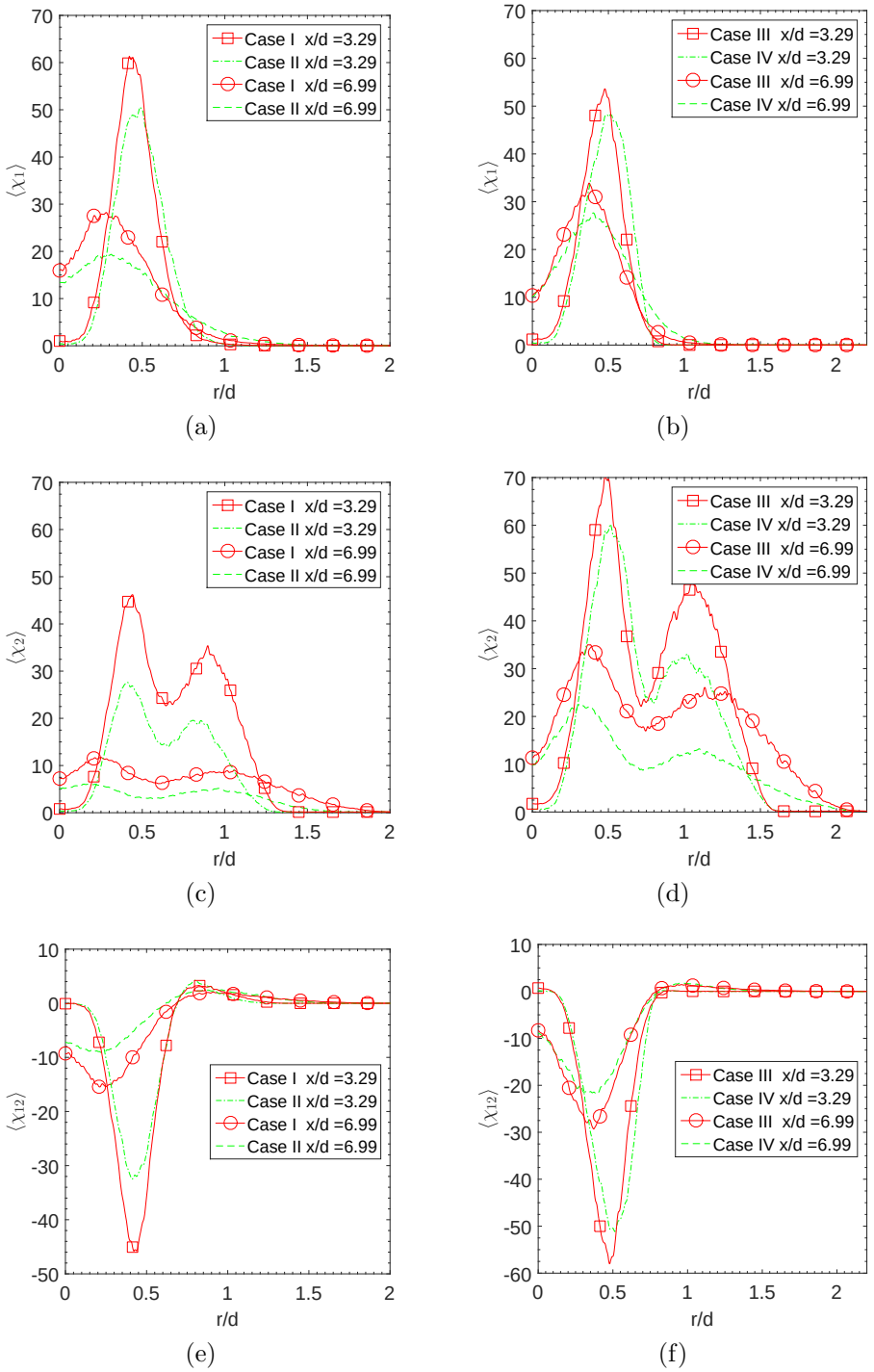

Figure 4.19: Cross-stream profiles of the mean scalar dissipation rates and the mean cross-dissipation rate.

shapes of mean scalar dissipation rates are similar to those of the rms fluctuations profiles. Each profile of the ϕ_1 dissipation rate, $\langle\chi_1\rangle$, also has an off-centerline peak, at approximately the same radial location as that of σ_1. The peak value is larger for Case I than Case II, because of the larger production rate of σ_1^2 due to the larger $\langle\phi_1\rangle$ gradient. The $\langle\chi_1\rangle$ peak value decreases faster downstream for Case II, again indicating the faster progression of mixing due to the mean shear between the center stream and the annular stream. Each profile of the ϕ_2 dissipation rate, $\langle\chi_2\rangle$, has two off-centerline peaks at approximately the same radial locations as those of the σ_2 profile. The values are larger for Case I than Case II at all radial locations, again consistent with the larger production rate of σ_2^2 for Case I. It is interesting that the mean shear between the ϕ_1-ϕ_2 streams for Case II does not result in higher $\langle\chi_1\rangle$ and $\langle\chi_2\rangle$ (left peak) values. Each profile of the mean cross-dissipation rate between ϕ_1 and ϕ_2, $\langle\chi_{12}\rangle$, has a negative off-centerline peak. Further away from the centerline, it increase and overshoots to a small positive value at approximately $r/d = 0.8$, before decreasing toward zero. The peak value (maximum magnitude) for Case I is also larger than Case II, which is a result of larger mean gradients for both ϕ_1 and ϕ_2.

The cross-stream profiles of the mean scalar dissipation rates and mean cross-dissipation for the larger annulus (figure 4.19b,d,f) have general trends similar to those of the smaller annulus. The peak values of the mean dissipation rates and the mean cross-dissipation rate are generally larger for Case III than Case IV. The peak values of $\langle\chi_1\rangle$ are slightly larger for the smaller annulus than the larger annulus at $x/d = 3.29$. However, they are smaller at $x/d = 6.99$. The peak values of $\langle\chi_2\rangle$ and $\langle\chi_{12}\rangle$ are generally much smaller for the smaller annulus and the peak values decay faster downstream for the smaller annulus. Moving downstream the peak locations generally also shift (both inward and outward) faster for the smaller annulus, also suggesting faster progression of mixing for the smaller annulus.

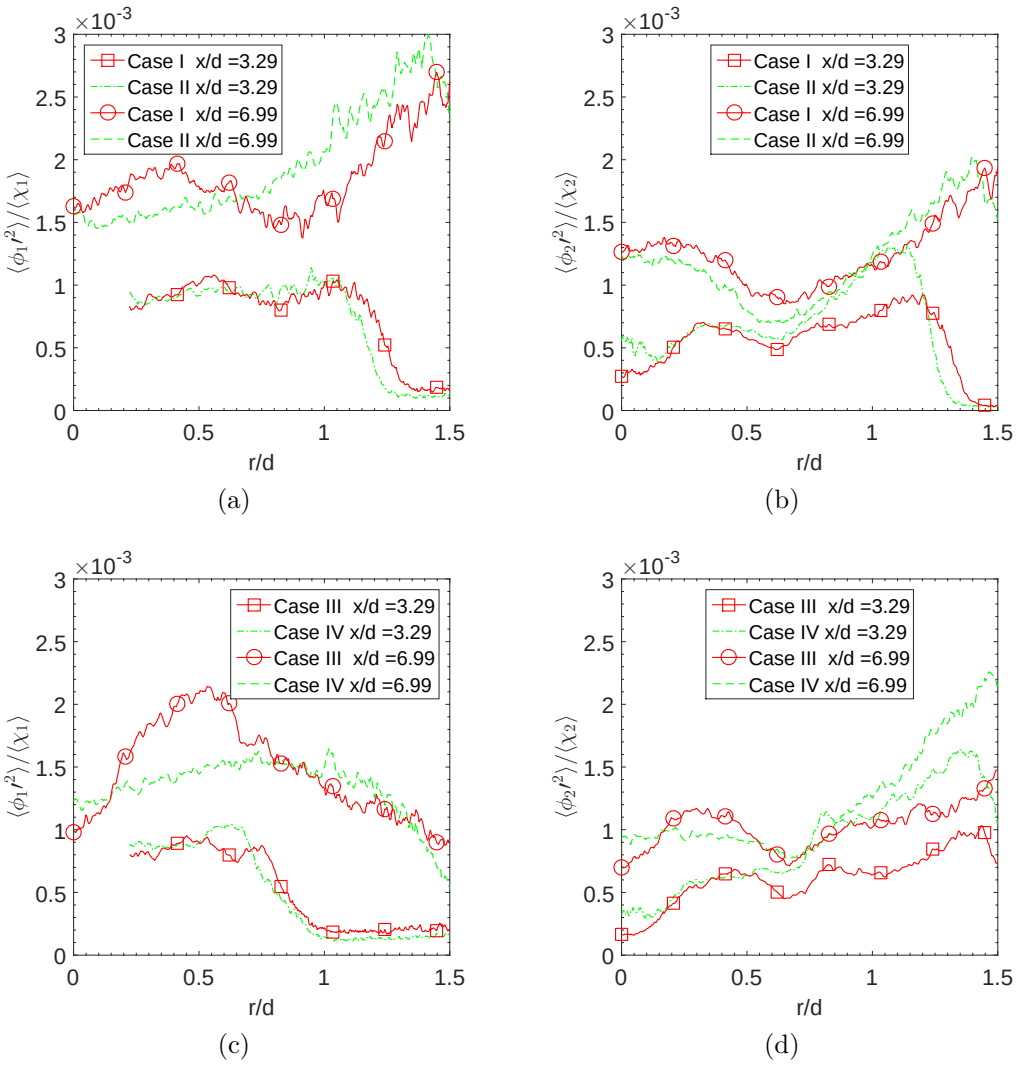

Figure 4.20: Cross-stream profiles of the scalar dissipation timescales.

The scalar dissipation time scale profiles are shown in figure 4.20. The time scale of ϕ_1, $\langle\phi_1'^2\rangle/\langle\chi_1\rangle$, is generally larger than the time scale of ϕ_2, $\langle\phi_2'^2\rangle/\langle\chi_2\rangle$, for all cases. The scalar time scale generally increases with the downstream distance as the jet width grows. The cross-stream variations of the time scales are generally small, similar to two scalar mixing in turbulent jets [38], except at locations far away from the centerline ($r/d > 0.8$) where the scalar mean dissipation rates are small (less than 10% of the peak value) and are susceptible to measurement uncertainties. The time scale profiles for Cases I(III) and II(IV) do not show significant differences. Comparisons between Cases I(II) and III(IV) also do not show significant differences.

4.3 Cross-stream JPDF, conditional diffusion, and conditional dissipation

The JPDF for $x/d = 3.29$ at three radial locations for the smaller annulus are shown in figure 4.21. On the centerline, the mixture is essentially pure ϕ_1 (figure 4.11). At $r/d = 0.165$ (not shown), the JPDF begins to extend toward (0,1) along the ϕ_1-ϕ_2 mixing line as ϕ_2 begins to mix with ϕ_1. The JPDF extends further for Case I than for Case II, a result of the stronger large-scale transport (flapping) for Case I. At $r/d = 0.372$, the JPDF extends further towards (0,1) and also begins to bend toward (0,0). The JPDF has reached (0.1, 0.5) and (0.16, 0.5) for Case I and Case II, respectively. These mixtures come from the co-flow air side and contain mostly ϕ_2 and ϕ_3. The JPDF area is larger and the left tail is closer to (0,0) for Case I.

Moving further away from the centerline, the JPDF extends further towards (0, 1) and bends more towards (0, 0) indicating that more ϕ_2 and ϕ_3 are present. Near the peak location of σ_1 profile (e.g. $r/d = 0.521$), the JPDF is bimodal for Case

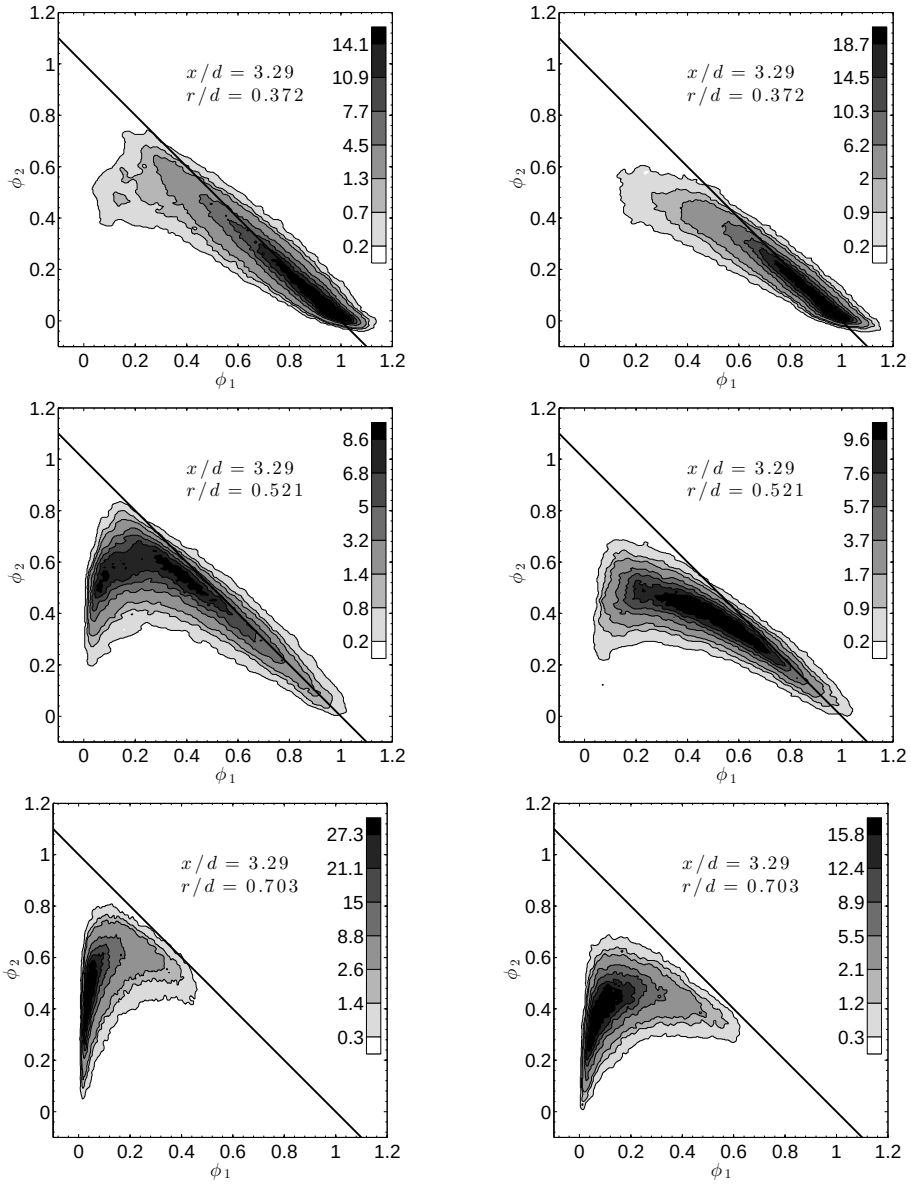

Figure 4.21: Cross-stream evolution of the scalar JPDF at $x/d = 3.29$ for the smaller annulus. Case I: left figures, Case II:right figures. The radial location is given in the top of each figure.

I with two peaks at (0.4, 0.5) and (0.10, 0.50). The two mixtures are essentially the ϕ_1-ϕ_2 and ϕ_2-ϕ_3 mixtures coming from the two mixing layers, and there is little mixing between them. The bimodal JPDF is a result of the transport of the two mixtures by the large-scale velocity fluctuations (flapping) generated by the single shear layer, and the relatively poor small-scale mixing due to the lack of a shear layer between the ϕ_1 and ϕ_2 streams. The strong transport also results in larger fluctuations in the ϕ_2-ϕ_3 mixture. By contrast, the JPDF for Case II is unimodal at all radical locations, due to the weaker transport and better small-scale mixing caused by the presence of the shear layer between the ϕ_1 and ϕ_2 streams. At $r/d = 0.703$, the JPDF for Case I becomes unimodal again and the peak of the JPDF moves close to (0, 0). The JPDF is mostly concentrated at very small ϕ_1 values with a tail pointing toward (1,0). However, the ϕ_1 value of the peak of the JPDF is larger for Case II. The tail for Case II extends further toward (1,0) for Case I, which represents well-mixed ϕ_1-ϕ_2 mixtures transported outward by the large-scale velocity fluctuations. These results are likely due to the larger advection by the mean-flow. Moving further outside ($r/d \geq 0.951$), the ridgeline of the JPDF (not shown) becomes a straight line with a large positive slope and the peak close to (0, 0), indicating that a small amount of ϕ_1 is well mixed with ϕ_2 and that the ϕ_1-ϕ_2 mixture is mixing with ϕ_3.

The conditional scalar diffusion, $\langle D_1 \nabla^2 \phi_1 | \phi_1, \phi_2 \rangle$ and $\langle D_2 \nabla^2 \phi_2 | \phi_1, \phi_2 \rangle$, for $x/d = 3.29$ at three radial locations for the smaller annulus is shown in figure 4.22. Since these diffusion terms transport the JPDF in the ϕ_1-ϕ_2 scalar space and are two components of a diffusion velocity, we use diffusion streamlines to represent them. We use the mean dissipation rate and rms fluctuations of ϕ_1 to non-dimensionalize the magnitude of the diffusion velocity. The mean composition, ($\langle \phi_1 \rangle$, $\langle \phi_2 \rangle$), is represented by a solid circle in the diffusion streamline plot. Close to the centerline (not shown), the diffusion streamlines generally converge towards the ϕ_1-ϕ_2 mixing line

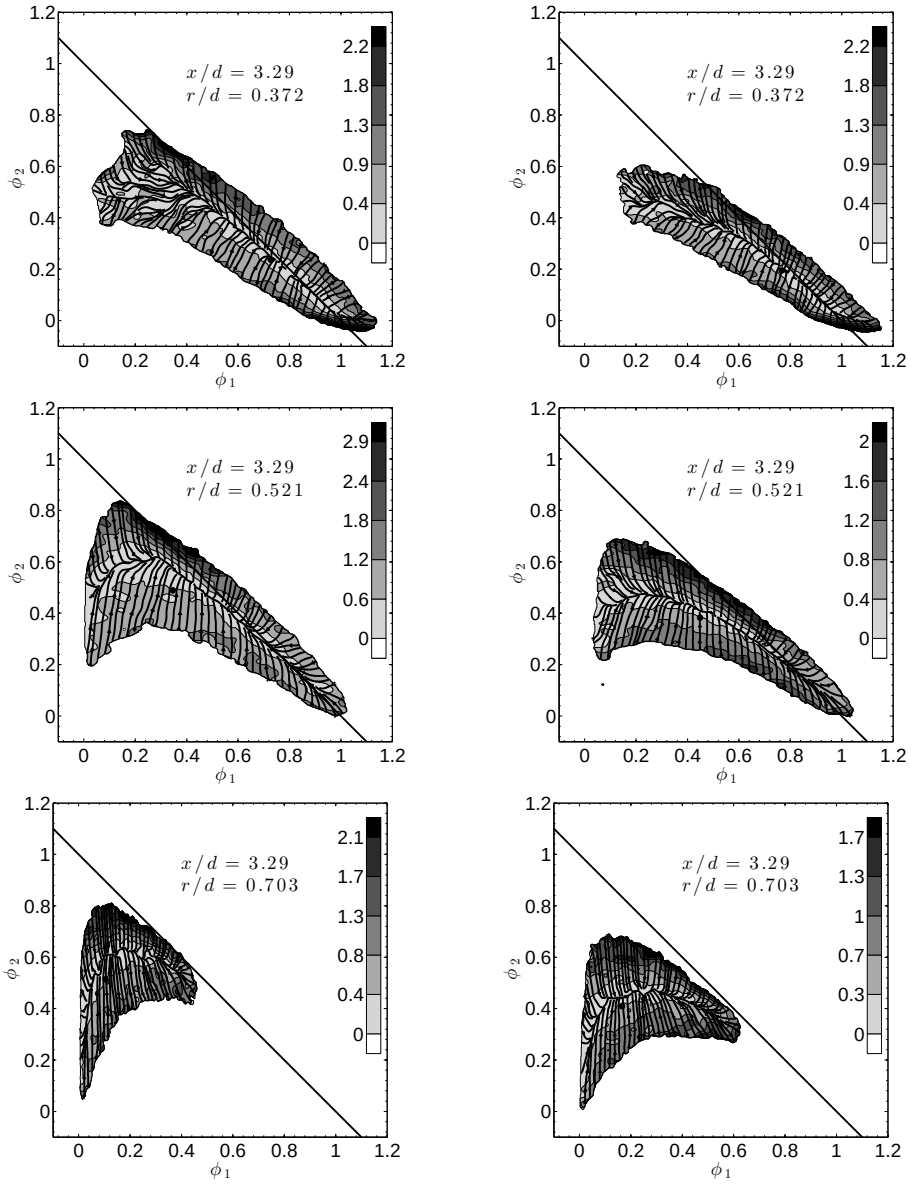

Figure 4.22: Cross-stream evolution of the scalar conditional diffusion at $x/d = 3.29$ for the smaller annulus. Case I: left figures, Case II:right figures. The contours magnitudes of the diffusion are the Euclidean norm of the diffusion velocity vector. The mean scalars $(\langle\phi_1\rangle, \langle\phi_2\rangle)$ is indicated in each streamline plot by a solid circle.

because the conditional diffusion is small and the measurement is dominated by the uncertainties. At $r/d = 0.372$, a manifold, towards which the diffusion streamlines first converge to, begins to emerge for Case I. There is also a hint of an emerging manifold for Case II. At $r/d = 0.521$, there are well-defined and bell-shaped diffusion manifolds for both cases, which are close to the ridgelines of the JPDFs. The manifold for Case I begins near (0, 0.45) and moves up to (0.3, 0.60), then bending towards the ϕ_1-ϕ_2 mixing line. The streamlines generally converge first in the ϕ_2 direction with large diffusion velocity magnitudes, and then move along the manifold with smaller diffusion velocity magnitudes. Unlike near the jet centerline, these diffusion streamlines results primarily from scalar mixing because the magnitude of conditional diffusion is much larger than that resulting from the measurement uncertainties, although it is still affected by them. The curvature of the manifold is much larger for Case I than Case II, consistent with a lesser degree of mixing for Case I, because mixing will eventually lead to a straight mixing line. The JPDF appears to be more symmetric with respect to the manifold in the ϕ_2 direction for Case II, while it extends further in the direction of lower ϕ_2 values for Case I, i.e., the fluctuations of ϕ_2 conditional on ϕ_1 is skewed toward small ϕ_2 values. This may reflect the uneven mixing on the two sides of the annular stream for Case I, with large mean shear on one side of the ϕ_2 stream, bringing in the co-flow air and generating large negative ϕ_2 fluctuations. Since there is mean shear on both sides of the ϕ_2 stream for Case II, the fluctuations of ϕ_2 are more symmetric with respect to the manifold. The solid circle (mean scalar values) is well below the manifold for Case I while it is closer to the manifold for Case II, consistent with faster mixing for Case II. We note that the manifold is close to the conditional mean, $\langle \phi_2 | \phi_1 \rangle$, and the separation of the mean scalars from it is a result of the three-scalar flow configuration. They become closer as the mixing process progresses. At $r/d = 0.703$, the diffusion streamline patterns

are the opposite of those close the centerline.

The conditional dissipation rates of ϕ_1 and ϕ_2, $\langle\chi_1|\phi_1,\phi_2\rangle$ and $\langle\chi_2|\phi_1,\phi_2\rangle$, and the conditional cross-dissipation rate, $\langle\chi_{12}|\phi_1,\phi_2\rangle$, are non-dimensionalized by the maximum mean dissipation rate of ϕ_1 at the same x/d location. For the smaller annulus at $x/d = 3.29$, the mixing is mostly between ϕ_1 and ϕ_2 close to the centerline; therefore the shapes of the conditional dissipation rates of ϕ_1 and ϕ_2 are similar, being small close to (1,0) and increasing away from (1,0) (figures not shown). The conditional cross-dissipation rate is generally negative since ϕ_1 and ϕ_2 are anti-correlated close to the centerline. At $r/d = 0.521$, where the JPDF is bimodal, $\langle\chi_1|\phi_1,\phi_2\rangle$ peaks on the lower edge of the JPDF near $\phi_1 = 0.4$ for both cases (figure 4.23). The peak is a result of mixing between nearly pure ϕ_1 and the ϕ_2-ϕ_3 mixture transported to this location by the large-scale velocity fluctuations, generating a sharp interface between them. A significant difference between Cases I and II is that above the peak location and near the ϕ_1-ϕ_2 mixing line, where the amount of co-flow air is small, the conditional dissipation rate of ϕ_1 is larger for Case I than Case II. The large velocity fluctuations for Case I transport relatively well-mixed ϕ_2-ϕ_3 mixtures to this location, resulting in a sharp interface and larger $\langle\chi_1|\phi_1,\phi_2\rangle$. By contrast, the turbulent transport is weaker for Case II and the small-scale mixing between ϕ_1-ϕ_2 streams is better due to the mean shear between the streams, especially when the amount of the co-flow air is small, thereby resulting in a lower dissipation near the ϕ_1-ϕ_2 mixing line. There are two peaks for the conditional dissipation rates of ϕ_2, due to the mixing of ϕ_2 on both sides of the ϕ_2 stream. The right peak of $\langle\chi_2|\phi_1,\phi_2\rangle$ is close to the peak location of $\langle\chi_1|\phi_1,\phi_2\rangle$, because it also results from the mixing between ϕ_1 and ϕ_2-ϕ_3 mixture. Similar to $\langle\chi_1|\phi_1,\phi_2\rangle$, $\langle\chi_2|\phi_1,\phi_2\rangle$ on the ϕ_1-ϕ_2 mixing line is larger for Cases I than Case II. The conditional cross-dissipation rates are mostly negative, and the (negative) peak is near the peak location of $\langle\chi_1|\phi_1,\phi_2\rangle$, because the gradients of

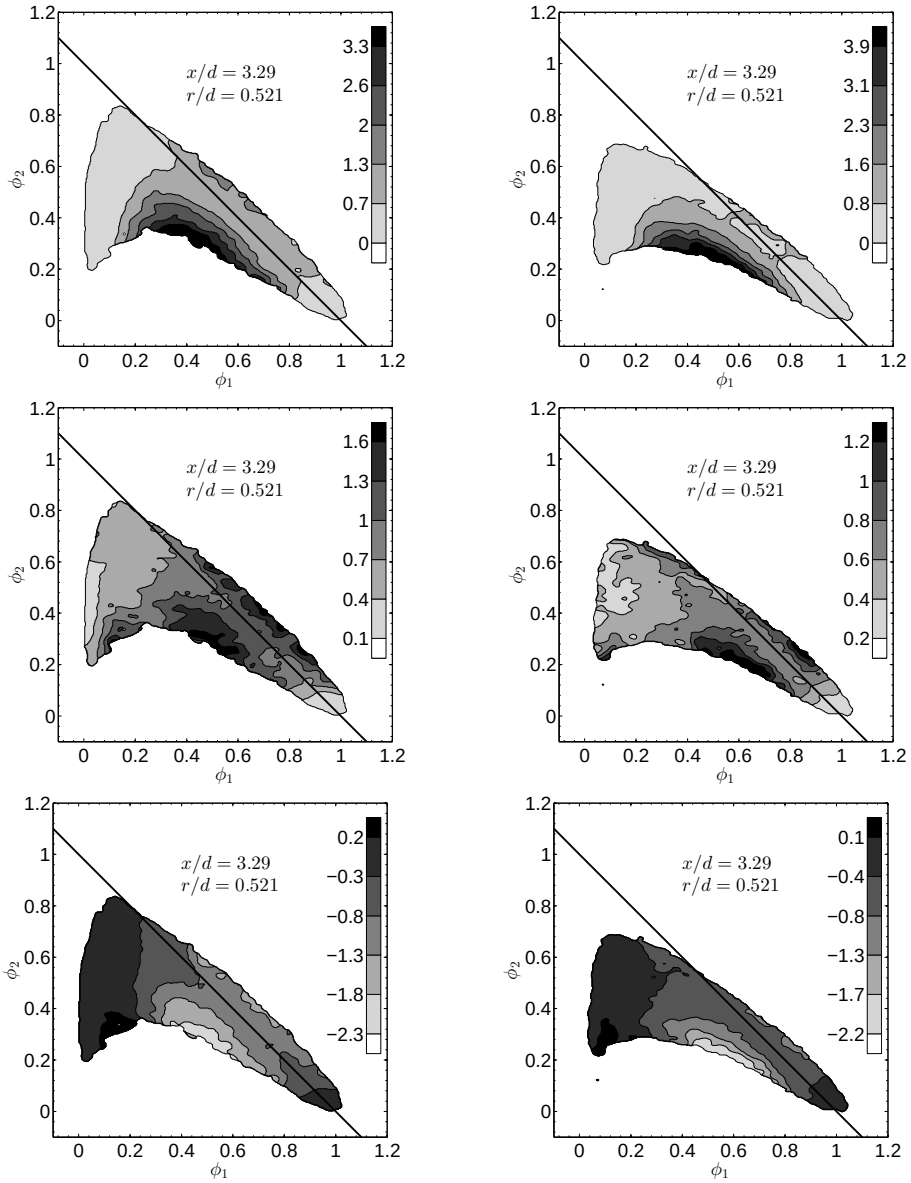

Figure 4.23: Conditional dissipation rate and conditional cross-dissipation rate at $x/d = 3.29$ and $r/d = 0.521$ for the smaller annulus. Case I: left figures, Case II:right figures. The top, middle and bottom rows are for $\langle \chi_1 | \phi_1, \phi_2 \rangle$, $\langle \chi_2 | \phi_1, \phi_2 \rangle$, and $\langle \chi_{12} | \phi_1, \phi_2 \rangle$, respectively.

ϕ_1 and ϕ_2 are anti-correlated. Moving away from the centerline (figures not shown), $\langle \chi_{12} | \phi_1, \phi_2 \rangle$ has positive peaks because ϕ_1 and ϕ_2 are well mixed.

Moving downstream to $x/d = 6.99$, the JPDF has already bent down toward (0,0) on the centerline for both cases (figure 4.24). Again, the area of the JPDF is larger and extends much further away from (1,0) for Case I than Case II. The peak of the JPDF has already moved away from the ϕ_1-ϕ_2 mixing line, with Case II moving further. The JPDF is again bimodal near the peak location of σ_1 profile (e.g. $r/d = 0.376$) for Case I. However, the curvature of the ridgeline of the JPDF is smaller than at the upstream location ($x/d = 3.29$ and $r/d = 0.521$), due to the progression of the mixing process. The JPDF is again unimodal for Case II at all radial locations. At $r/d = 0.538$, the peak of the JPDF is at (0.1, 0.4) for Case I, which is largely a ϕ_2-ϕ_3 mixture with large but relatively rare ϕ_1 fluctuations. The peak of the JPDF for Case II is at (0.4,0.3), which is close to the center of the JPDF. The mixture contains significant amounts of all three scalars. Again, mixing is occurring in a mixture with relatively uniform ϕ_2 but with large variations of ϕ_1 and ϕ_3. At $r/d = 0.827$, the peak of the JPDF moves close to (0,0), but with a tail bending toward (1,0). Similar to the upstream location ($x/d = 3.29$), the tail is longer for Case II than Case I. The tail disappears further away from the centerline and the ridgeline of the JPDF becomes a straight line.

The conditional diffusion streamlines at $x/d = 6.99$ (figure 4.25) have general patterns similar to those at $x/d = 3.29$. The manifold is already well defined even on the centerline. For both Cases I and II, the curvature of the manifold is smaller at $x/d = 6.99$ than at $x/d = 3.29$ and the mean composition (the solid circle) is closer to the manifold. The curvature of the manifold is larger for Case I than Case II, again consistent with a lesser degree of mixing for Case I. The JPDF is skewed toward smaller ϕ_2 values for Case I, while it is quite symmetric with respect

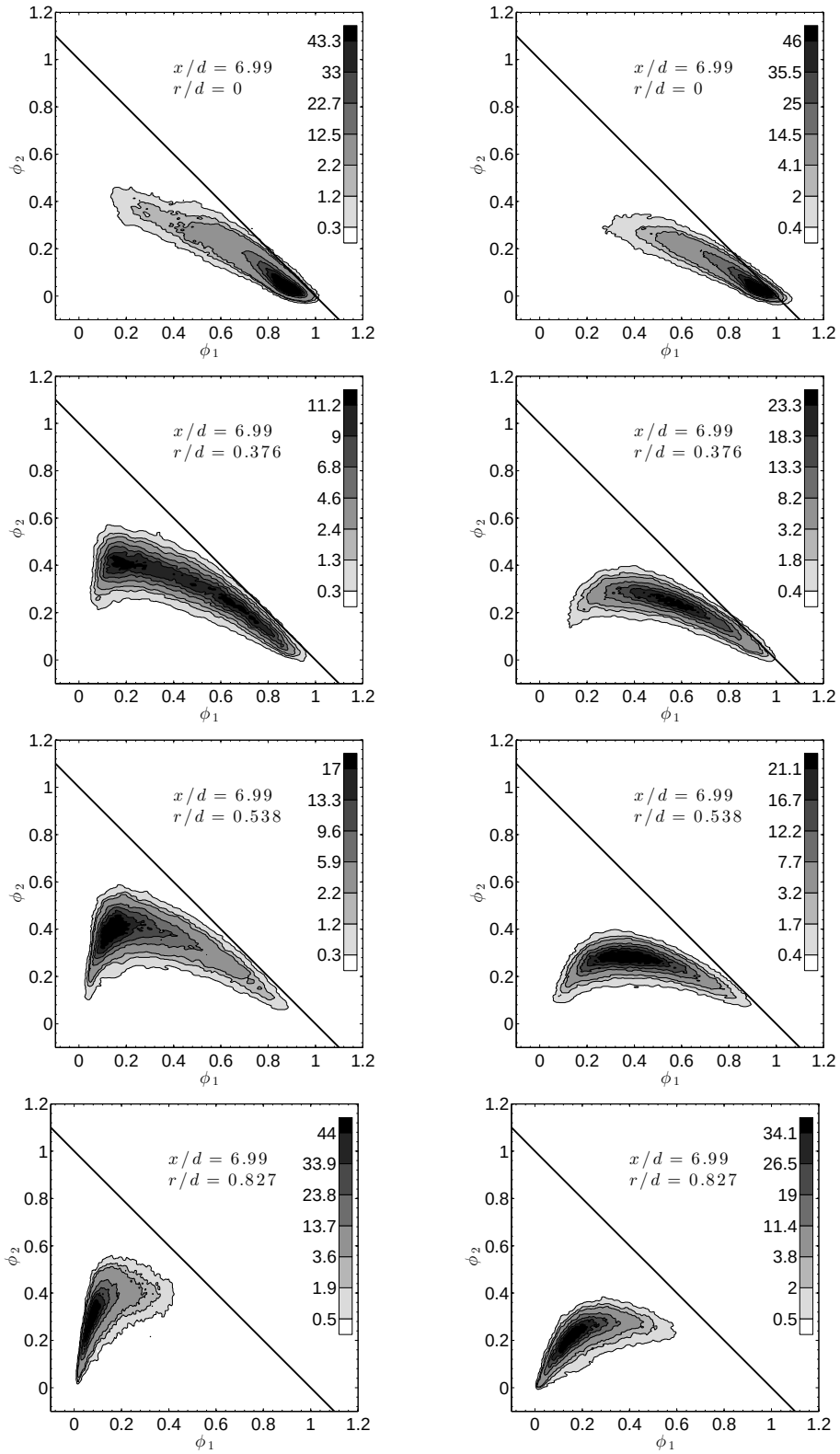

Figure 4.24: Conditions same as figure 4.21 but at $x/d = 6.99$.

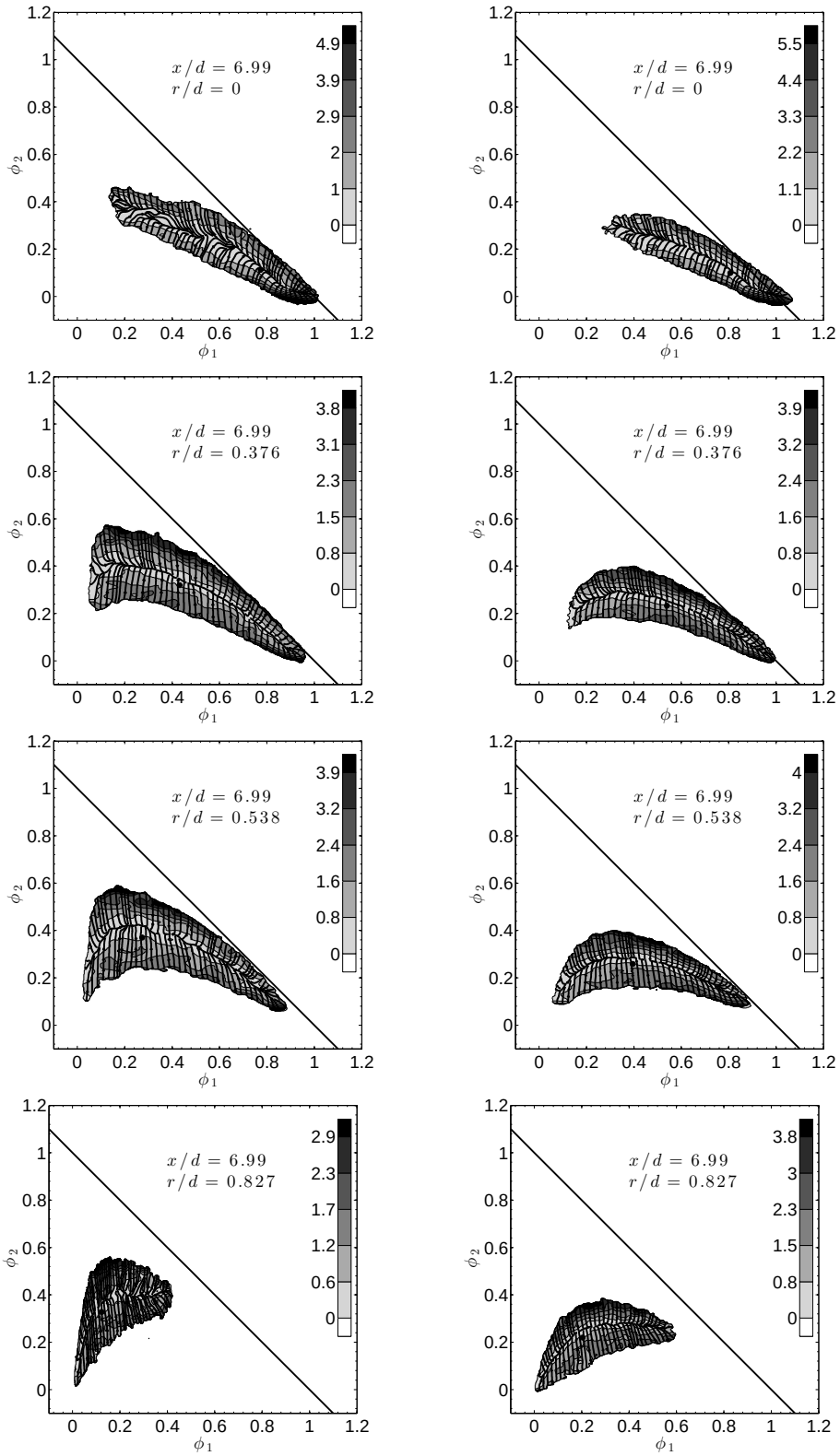

Figure 4.25: Conditions same as figure 4.22 but at $x/d = 6.99$.

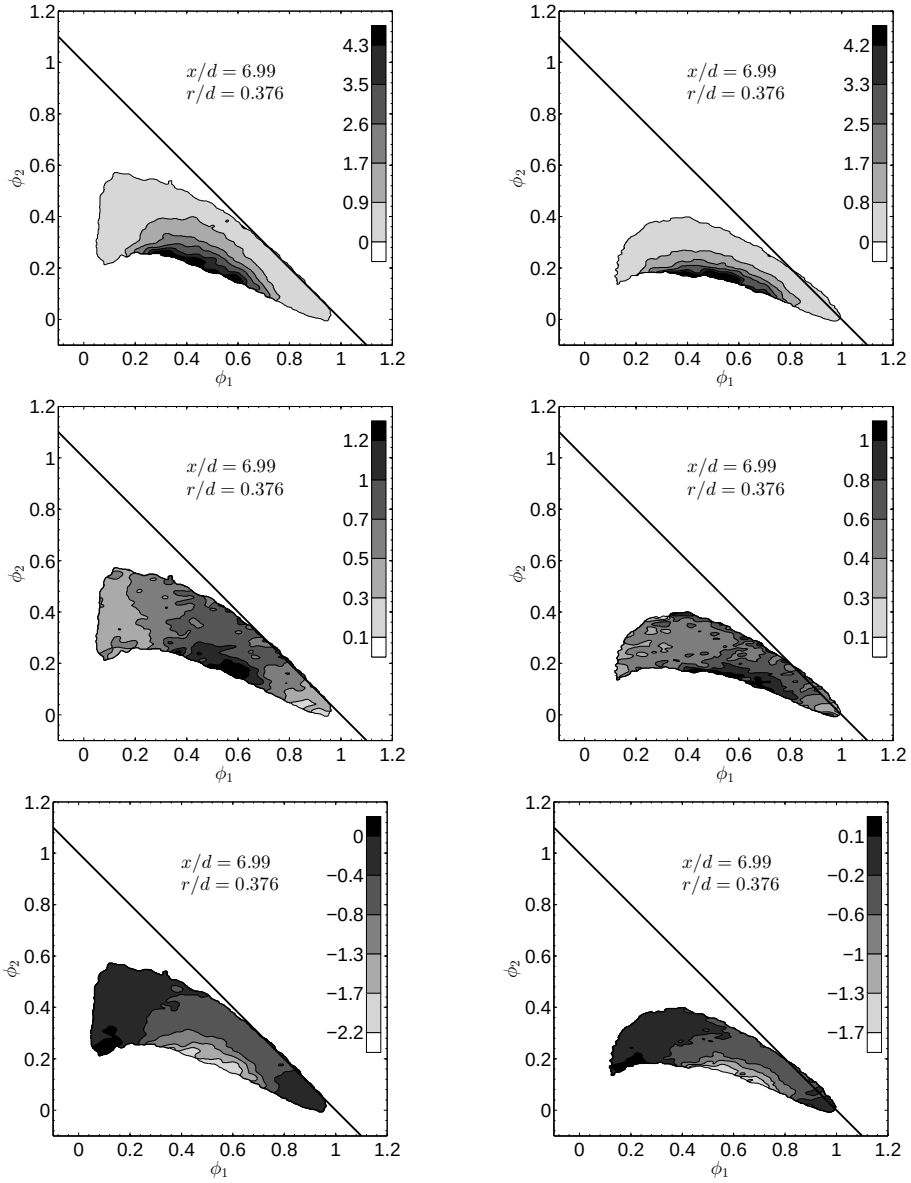

Figure 4.26: Conditions same as figure 4.23 but at $x/d = 6.99$ and $r/d = 0.376$.

to the manifold for Case II. The general trends for the conditional dissipation and conditional cross-dissipation at $x/d = 6.99$ (figure 4.26) are also generally similar to those at $x/d = 3.29$.

The JPDF for $x/d = 3.29$ at three radial locations for the larger annulus are shown in figure 4.27. On the centerline, the mixture is again essentially pure ϕ_1 (figure 4.12). At $r/d = 0.124$, the JPDF begins to extend along the ϕ_1-ϕ_2 mixing line. The JPDF extends further for Case III than for Case IV, similar to the differences between Case I and Case II. At $r/d = 0.331$, the JPDF has a long tail toward (0,1), indicating large ϕ_2 fluctuations, while the peak is still close to (1,0). At $r/d = 0.448$, the ridgeline of the JPDF connects (0,1) and (1,0), which is a result of the turbulent transport (flapping of the ϕ_1-ϕ_2 mixing layer). The peak of the JPDF has moved significantly toward (0,1). The JPDF is still quite symmetric with respect to the ϕ_1-ϕ_2 mixing line for Case III. However, there is a tail on the LHS of the JPDF extending toward (0,0) for Case IV. At $r/d = 0.662$, the peak of the JPDF is very close to (0,1), while the JPDF has tails pointing toward both (0,0) and (1,0), indicating that nearly pure ϕ_2 mixture is mixing with ϕ_1 and ϕ_3 separately. There is no direct mixing between ϕ_1 and ϕ_3 because they are separated by nearly pure ϕ_2. The lower values of ϕ_2 for Case IV is due to the faster mixing of ϕ_2 since there is mean shear on both sides of the annular stream. The tail toward (0,0) becomes longer and the tail toward (1,0) becomes shorter when moving further away from the centerline (not shown). The peak of JPDF also leaves (0,1) and moves toward (0,0).

The conditional diffusion at $x/d = 3.29$ and $r/d = 0.662$ for Cases III and IV is shown in figure 4.28. Diffusion streamlines at other radial locations are not shown because they are dominated by measurement uncertainties. At $r/d = 0.662$, the diffusion streamlines mostly converge to the ϕ_1-ϕ_2 mixing line directly. There is no sign of a curved manifold. Here the mixing is still largely binary as ϕ_1 and ϕ_3 are

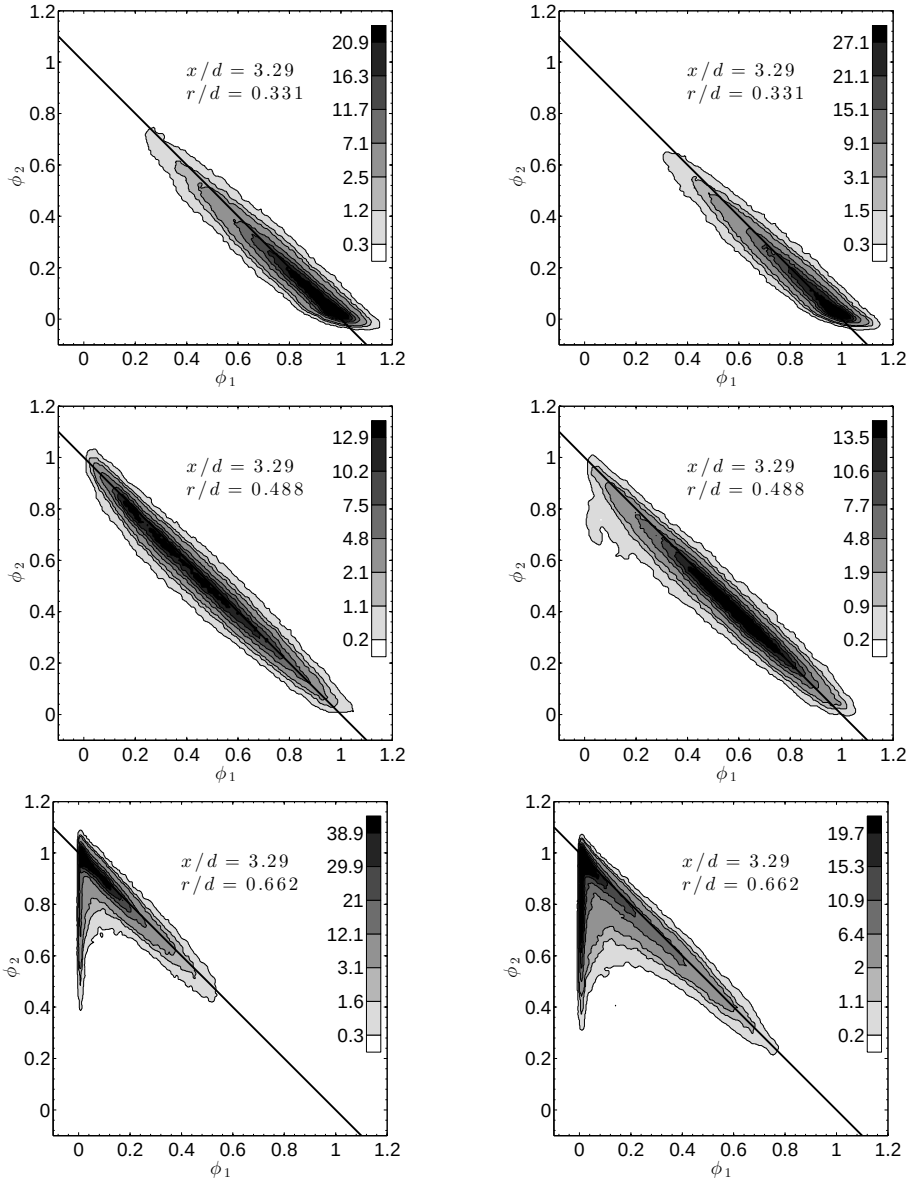

Figure 4.27: Cross-stream evolution of the scalar JPDF at $x/d = 3.29$ for the larger annulus. Case III:left figures, Case IV:right figures.

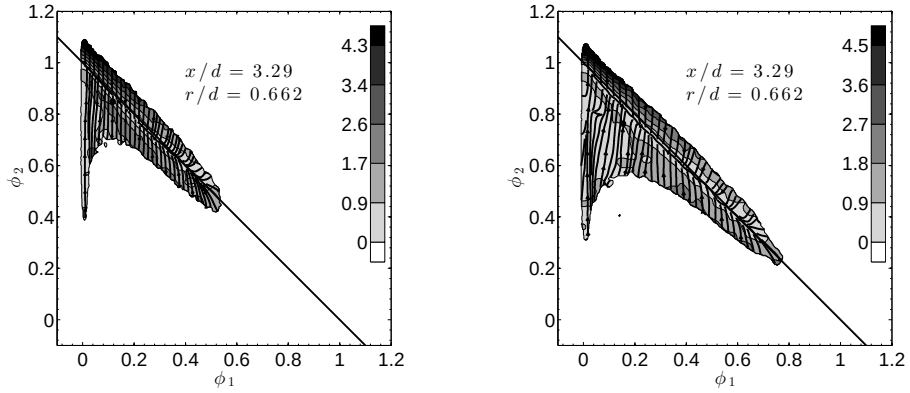

Figure 4.28: Scalar conditional diffusion at $x/d = 3.29$ and $r/d = 0.662$ for the larger annulus. Case III:left, Case IV:right.

still separated by nearly pure ϕ_2 without direct mixing between them, while a curved manifold generally is a result of three-scalar mixing.

On the centerline at $x/d = 6.99$, the ridgelines of the JPDFs are still close to the ϕ_1-ϕ_2 mixing line for both Cases III and IV (figure 4.29). At $r/d = 0.289$, the JPDF begins to bend toward (0,0) and extends much further toward (0,1) for Case III. Its area is also larger, indicating stronger transport. The JPDF for Case III is bimodal at $r/d = 0.496$, with two peaks at (0.4,0.6) and (0.05,0.6), which are essentially ϕ_1-ϕ_2 mixture and ϕ_2-ϕ_3 mixture coming from the two mixing layers. There are still nearly pure ϕ_2 samples at this location. However, unlike at $x/d = 3.29$ the peak of JPDF does not reach (0,1), a result of the progression of the mixing process. The JPDF is unimodal for Case IV at all radial locations. At $r/d = 0.744$, the right peak has disappeared for Case III. The general trends of the evolution of the JPDF moving further outside are similar to those of the smaller annulus cases.

The patterns of conditional diffusion streamlines at $x/d = 6.99$ for the larger annulus (figure 4.30) are generally similar to those of the smaller annulus cases at $x/d = 3.29$. The manifold begins to emerge at $r/d = 0.289$ (figures not shown) and it is well defined at $r/d = 0.496$. The curvature of the manifold is larger for Case III

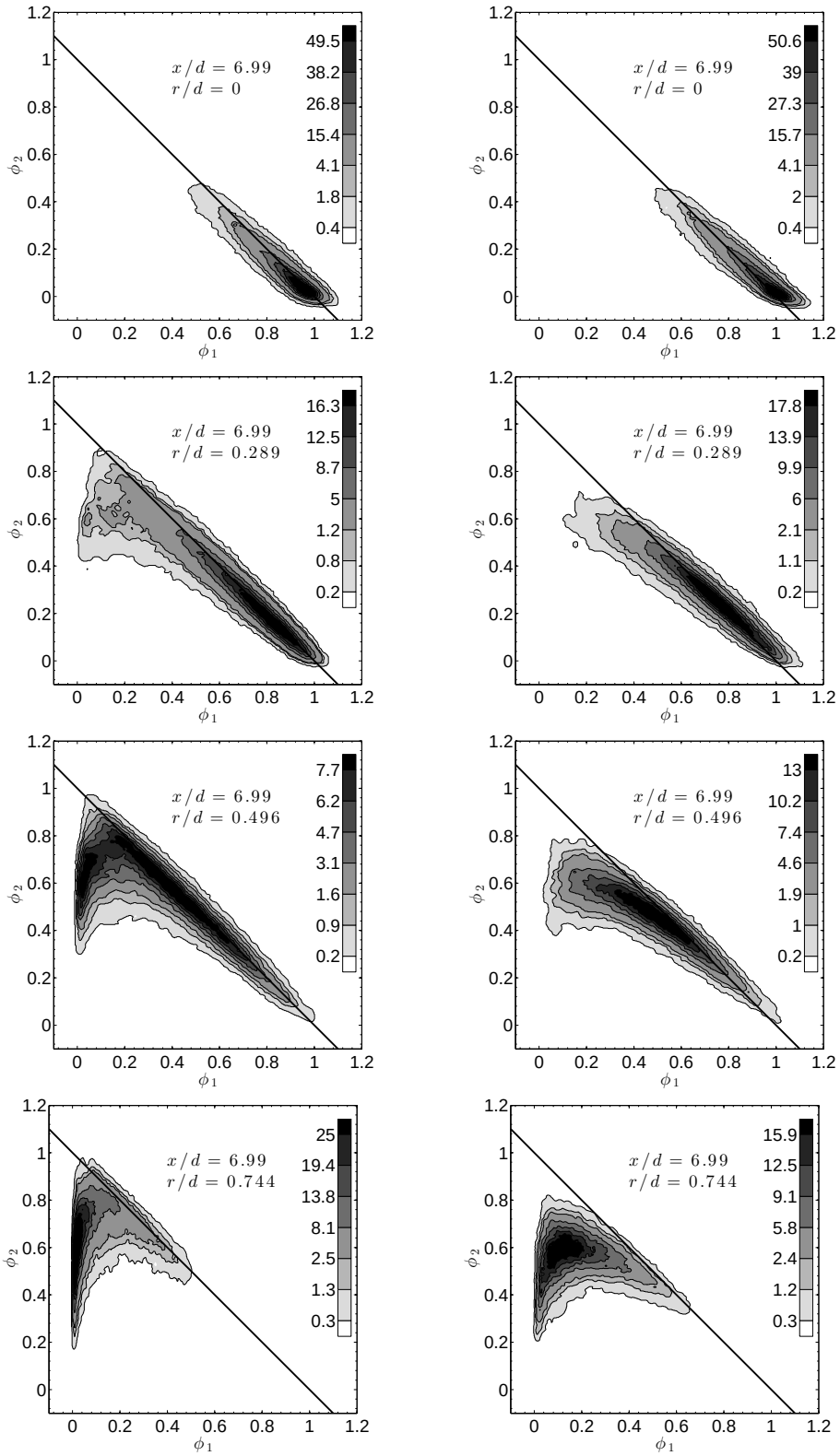

Figure 4.29: Cross-stream evolution of the scalar JPDF at $x/d = 6.99$ for the larger annulus. Case III:left figures, Case IV:right figures.

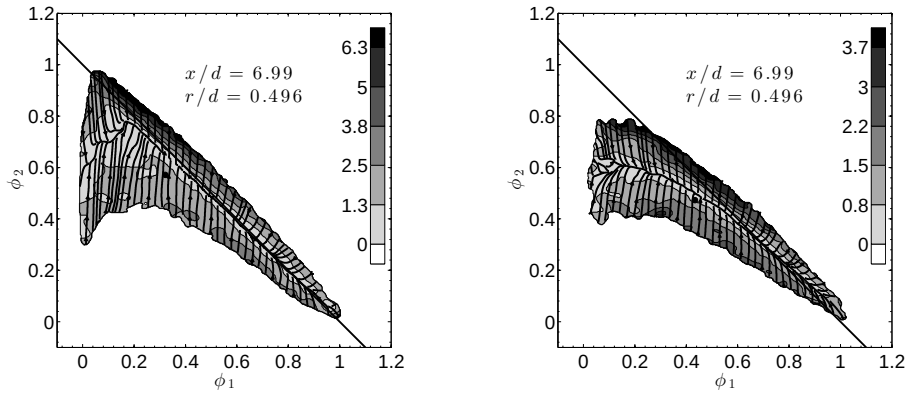

Figure 4.30: Cross-stream scalar conditional diffusion at $x/d = 6.99$ and $r/d = 0.496$ for the larger annulus. Case III:left, Case IV:right.

than Case IV. The mean composition is further away from the manifold for Case III. The curvature of the manifold for Case III at $x/d = 6.99$ appears to be larger than for Case I at $x/d = 3.29$, indicating that the mixing has progressed less. The general trends of the conditional dissipation rates and conditional cross-dissipation rate for the larger annulus at $x/d = 6.99$ (figure 4.31) are also similar to those of the smaller annulus at $x/d = 3.29$.

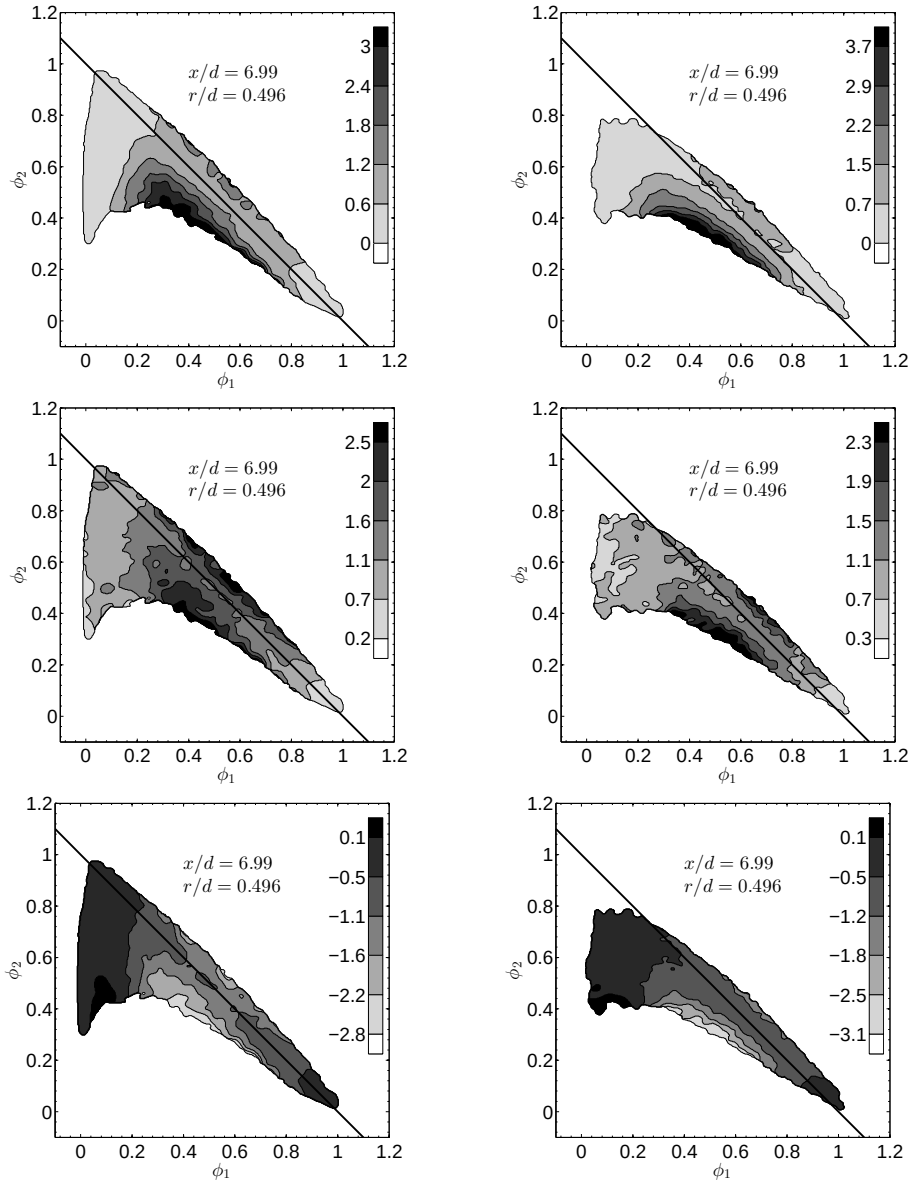

Figure 4.31: Cross-stream scalar conditional dissipation at $x/d = 6.99$ and $r/d = 0.496$ for the larger annulus. Case III:left, Case IV:right. The top, middle and bottom rows are for $\langle \chi_1 | \phi_1, \phi_2 \rangle$, $\langle \chi_2 | \phi_1, \phi_2 \rangle$, and $\langle \chi_{12} | \phi_1, \phi_2 \rangle$, respectively.

Chapter 5

Three-scalar subgrid-scale mixing in the context of LES

The three-scalar SGS mixing in the turbulent coaxial jets will be studied in this Chapter. The scalar FJDF and the SGS mixing terms in the FJDF transport equation will be analyzed to study the physics of multiscalar SGS mixing. The FJDF is defined as

$$f(\hat{\phi}_1, \hat{\phi}_2; \mathbf{x}, t) = \langle \delta(\phi_1 - \hat{\phi}_1)\delta(\phi_2 - \hat{\phi}_2) \rangle_L = \int \delta(\phi_1 - \hat{\phi}_1)\delta(\phi_2 - \hat{\phi}_2) G(\mathbf{x} - \mathbf{x}') d\mathbf{x}', \quad (5.1)$$

where ϕ_1, ϕ_2, $\hat{\phi}_1$, and $\hat{\phi}_2$ are the mixture fractions of the center jet stream and the annular stream, and their sample-space variables, respectively. The filter function is denoted by G. We use the "top-hat" (or box) filter in this study since it is simple and ensures positiveness of the FJDF. The FJDF transport equation is

$$\begin{aligned} \frac{\partial f}{\partial t} + \frac{\partial}{\partial x_i}\left[f \langle V_i | \hat{\phi}_1, \hat{\phi}_2 \rangle_L \right] &= -\frac{\partial}{\partial \hat{\phi}_1}\left[f \langle D_1 \nabla^2 \phi_1 | \hat{\phi}_1, \hat{\phi}_2 \rangle_L \right] - \frac{\partial}{\partial \hat{\phi}_2}\left[f \langle D_2 \nabla^2 \phi_2 | \hat{\phi}_1, \hat{\phi}_2 \rangle_L \right] \\ &= (D_1 + D_2)\nabla^2 f - \frac{1}{2}\frac{\partial^2}{\partial \hat{\phi}_1^2}\left[f \langle \chi_1 | \hat{\phi}_1, \hat{\phi}_2 \rangle_L \right] - \frac{1}{2}\frac{\partial^2}{\partial \hat{\phi}_2^2}\left[f \langle \chi_2 | \hat{\phi}_1, \hat{\phi}_2 \rangle_L \right] - \frac{\partial^2}{\partial \hat{\phi}_1 \partial \hat{\phi}_2}\left[f \langle \chi_{12} | \hat{\phi}_1, \hat{\phi}_2 \rangle_L \right], \end{aligned} \quad (5.2)$$

where V_i is the velocity vector. The LHS of equation 5.2 is the time rate of change of the FJDF and the transport of the FJDF in physical space by the conditionally filtered velocity. The RHS gives two forms of the mixing terms. The first involves two terms that can be interpreted as the transport of FJDF in the scalar space by the corresponding conditionally filtered diffusion, $\left\langle D_1 \nabla^2 \phi_1 | \hat{\phi}_1, \hat{\phi}_2 \right\rangle_L$ and $\left\langle D_2 \nabla^2 \phi_2 | \hat{\phi}_1, \hat{\phi}_2 \right\rangle_L$. The second form involves four terms, which are the transport of FJDF in physical space by molecular diffusion, and transport in scalar space by the conditionally filtered dissipation rates and by the conditionally filtered cross-dissipation rate.

The filtered scalar means, the filtered mean scalar SGS variances, the scalar FJDF, the conditionally filtered scalar dissipation rates, conditionally filtered cross-dissipation rate, and the conditionally filtered diffusion are analyzed to study the SGS mixing. We compute the means of these variables conditional on the filtered value and the SGS variance of ϕ_1, given as

$$\langle \phi_1 \rangle_L = \int \phi_1(\mathbf{x}') G(\mathbf{x} - \mathbf{x}') d\mathbf{x}' \tag{5.3}$$

and

$$\langle \phi_1''^2 \rangle_L = \int \{\phi_1(\mathbf{x}') - \langle \phi_1 \rangle_L(\mathbf{x})\}^2 G(\mathbf{x} - \mathbf{x}') d\mathbf{x}'. \tag{5.4}$$

In the present three-scalar mixing problem, ϕ_1 is analogous to the mixture fraction in a nonpremixed reactive flow. Due to the important role of mixture fraction in such flows, previous studies [4, 8, 29] have obtained the conditionally filtered dissipation and diffusion using the filtered mixture fraction and the mixture fraction SGS variance as conditioning variables. Thus the conditioning variables in the present study ensure that the SGS mixing process closely approximate that in a nonpremixed reactive flow. Several filter widths (Δ) ranging from 0.25 to 0.8 mm were used. To ensure that the

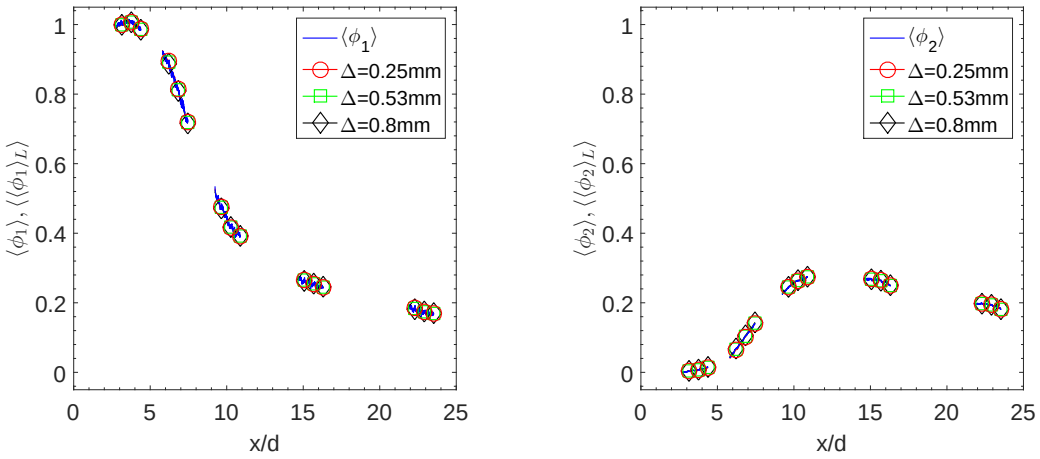

Figure 5.1: Centerline profiles of the filtered mean scalar for Case I.

results are relevant to LES at high Reynolds numbers, the filter widths employed are significantly larger than the dissipative scales (≈ 0.014 mm), so that the subgrid scales contain sufficient fluctuations. Given the moderate Reynolds number of the coaxial jet, the filter widths employed are not very small compared to the integral length scales. Nevertheless, they are preferable than smaller filter widths, which will be too close to the dissipative scales. Previous studies (e.g., [63, 67]) have shown that when the filter width is much larger than the dissipation scales the properly scaled conditional statistics are not sensitive to the filter width. Thus, the results for the FJDF and the SGS mixing terms are only given for the 0.53 mm filter.

5.1 Evolution on the jet centerline

The profiles of the mean filtered scalars, $\langle\langle\phi_1\rangle_L\rangle$ and $\langle\langle\phi_2\rangle_L\rangle$, on the jet centerline for Case I are shown in figure 5.1. The difference in the mean filtered scalars between different filter scales are negligible. The mean filtered scalars are very close to the mean scalar profiles for the filter scales considered. The general trends are

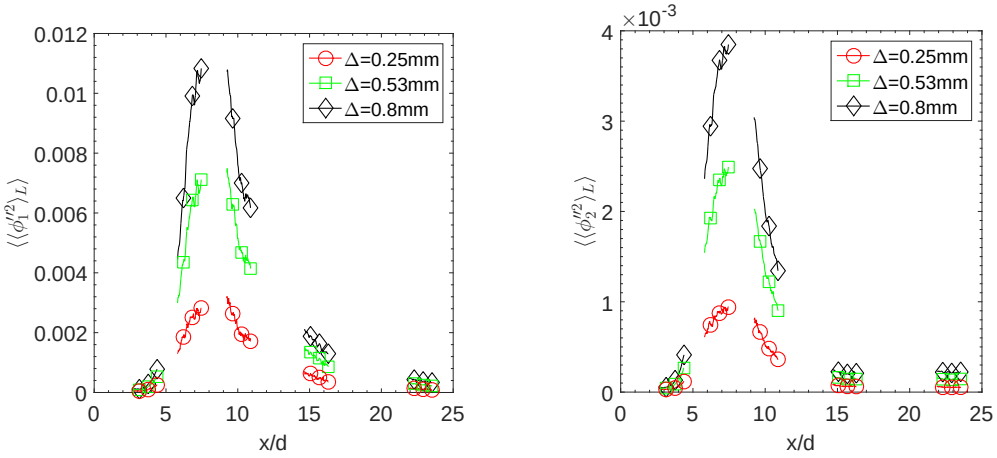

(a) (b)

Figure 5.2: Centerline profiles of the filtered mean SGS variance for Case I.

similar for other cases (figures not shown).

The profiles of the mean SGS scalar variances, $\langle\langle\phi_1''^2\rangle_L\rangle$ and $\langle\langle\phi_2''^2\rangle_L\rangle$, on the jet centerline for Case I are shown in figure 5.2. The SGS scalar variances evolve similarly as the scalar variances (figure 4.3). Their values, however, are significantly smaller than the scalar variances. The peak value of $\langle\langle\phi_1''^2\rangle_L\rangle$ is approximately 8%, 20% and 32% of $\langle\phi_1'^2\rangle$ for the three filter widths ($\Delta = 0.25, 0.53, 0.8$mm), respectively, while $\langle\langle\phi_2''^2\rangle_L\rangle$ is 6.5%, 17% and 27% of $\langle\phi_2'^2\rangle$. The general trends are similar for the other cases (figures not shown). The relative magnitudes of the mean SGS variances among the cases are similar to those of the scalar variances, with the peak values generally larger for cases with the higher velocity ratio and the larger annulus width.

The results for the FJDF are given as a conditional mean, $\langle f|\langle\phi_1\rangle_L, \langle\phi_1''^2\rangle_L\rangle$, referred to simply as FJDF hereafter for convenience. The FJDF conditional on the small SGS variance on the centerline for Case I are shown in figure 5.3. The values of the conditional variables, $\langle\phi_1\rangle_L$ and $\langle\phi_1''^2\rangle_L$, are given in each figure. The value of $\langle\phi_1\rangle_L$ is taken as its local mean, $\langle\langle\phi_1\rangle_L\rangle$, at the physical location. We use grayscales and isocontours to represent the FJDF. The outermost contour represents the boundary

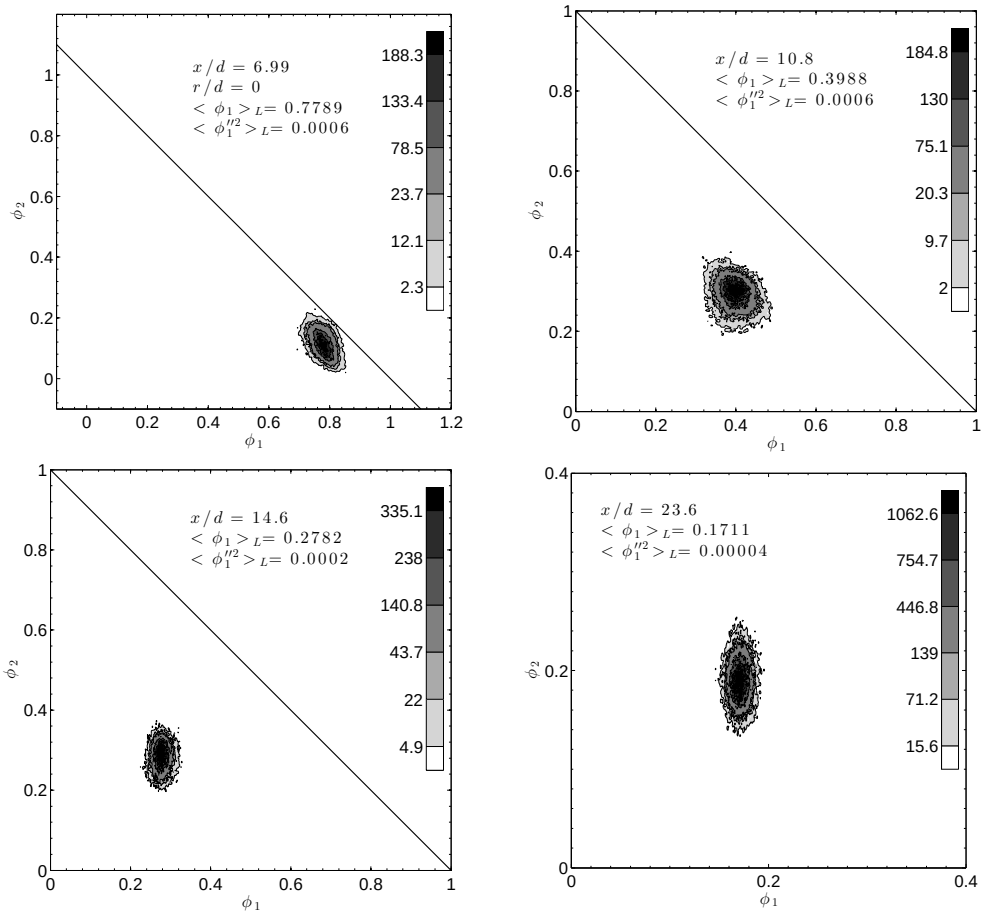

Figure 5.3: Evolution of the scalar FJDF conditional on the small SGS variance on the centerline for Case I.

within which the FJDF integrates to 99%. The FJDF should be confined to a triangle in the ϕ_1-ϕ_2 space with the vertices at (1, 0), (0, 1), and (0, 0), where the coordinates denote the sample-space variables for ϕ_1, ϕ_2 and ϕ_3, respectively. For small SGS variance, the FJDF is always unimodal and appears to have a Gaussian-like shape. For $x/d < 5$, it is centered on the ϕ_1-ϕ_2 mixing line connecting (1, 0) and (0, 1), indicating that the SGS scalars contain little co-flow air. Further downstream the FJDF moves away from the mixing line towards (0, 0) due to mixing with the co-flow air. The evolution of the FJDF is generally consistent with filtered mean values. The general trends are similar for other cases (figures not shown).

For large SGS variance (figure 5.4), the FJDF close to the jet exit ($x/d < 8$) is unimodal, with the peak near (1, 0) and a long tail. The area of the FJDF is much larger than for the small SGS variance, consistent with the relative magnitudes of the SGS variance. At $x/d = 10.8$, the FJDF becomes bimodal for both Cases I and II, indicating that the SGS mixing is between two distinct and segregated SGS mixtures (ϕ_1'' and ϕ_2''). The two SGS scalars are negatively correlated at this location. At $x/d = 14.6$, the two peaks become closer and are away from the mixing line due to the presence of more co-flow air. The ridgeline of the FJDF is horizontal for both cases with Case II has a much slender shape, consistent with better molecular mixing due to the existence of mean shear between the center jet and the annular stream. Further downstream ($x/d = 23.6$), the FJDF is still bimodal while moving closer to (0, 0). The two peaks are also much closer and become positively correlated, indicating that they are well mixed and that they are mixing largely in unison with the co-flow air. Note that for the smaller annulus cases, the JPDF is unimodal on the centerline. Thus similar to the SGS mixing in binary mixing, there also exist two SGS mixing regimes for the coaxial jets. For small SGS variance the SGS scalars are relatively well mixed whereas for large SGS variance the scalars are highly segregated.

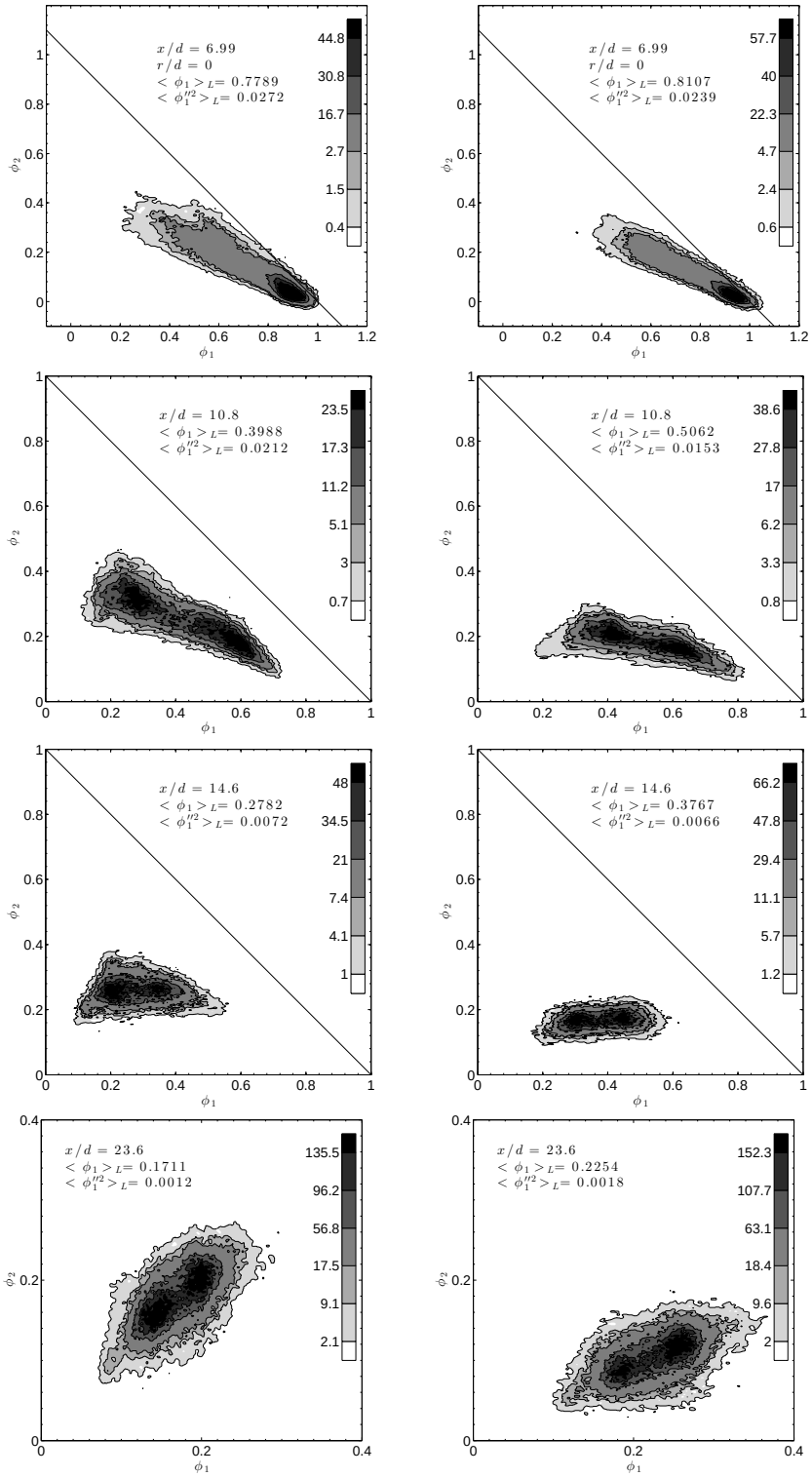

Figure 5.4: Evolution of the scalar FJDF conditional on the large SGS variance on the centerline for Case I (Left) and Case II (Right).

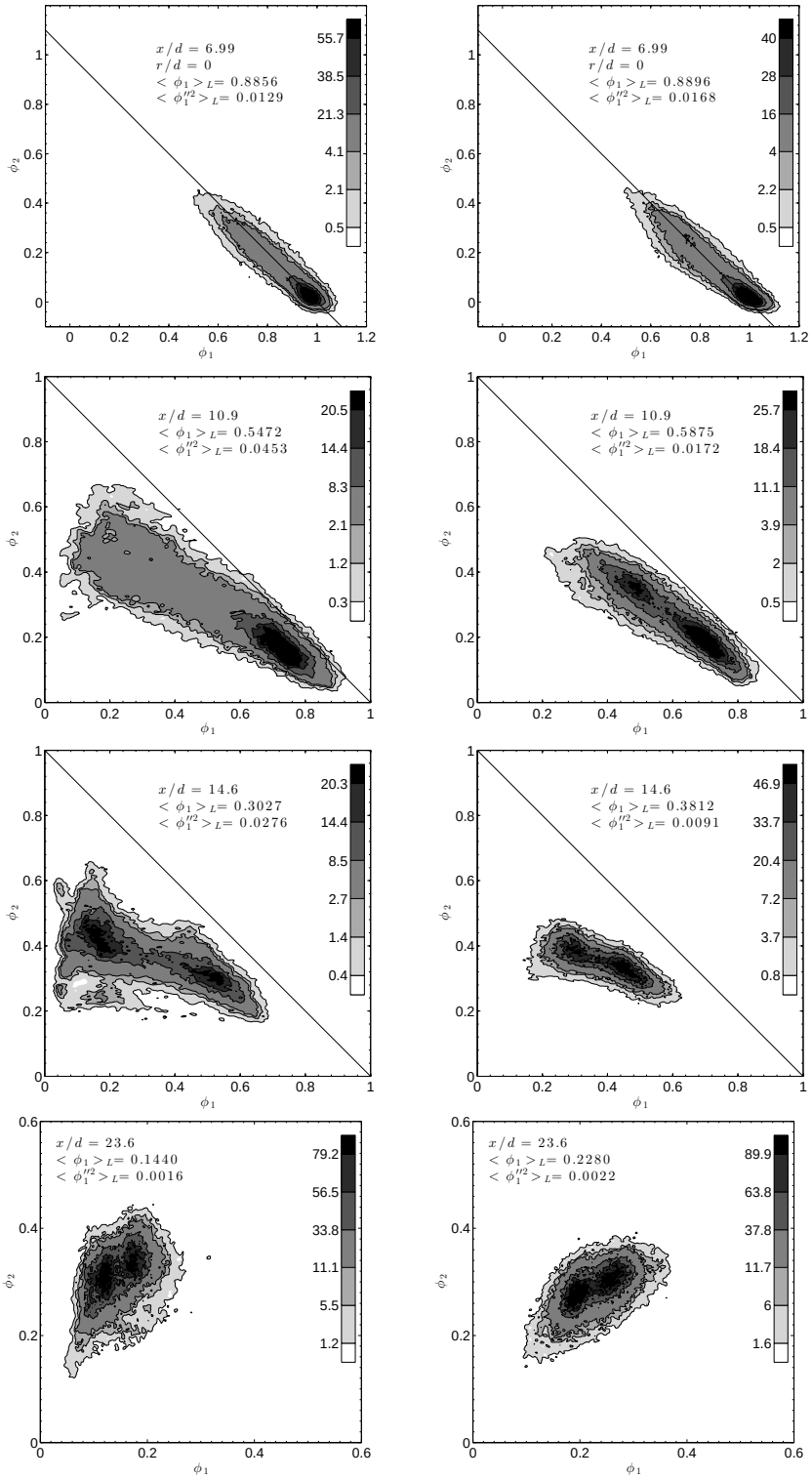

Figure 5.5: Evolution of the scalar FJDF conditional on the large SGS variance on the centerline for Case III (Left) and Case IV (Right).

The general trends for larger annulus cases (figure 5.5) are generally similar to those of the smaller annulus. The FJDF extends further along the ϕ_1-ϕ_2 mixing line before bending toward (0,0), consistent with slower progression of mixing for the larger annulus cases. The FJDF is unimodal for Case III at $x/d = 10.9$ while it is bimodal for Case IV, although the value of the SGS variance chosen is smaller for Case IV (The mean SGS variance is also smaller). This is quite different from the evolution of the JPDF on the centerline in that JPDF is bimodal at some locations for Case III but is always unimodal for Case IV (figure 4.12). Moving downstream ($x/d = 14.6$), the FJDF also becomes bimodal for Case III. Similar to the smaller annulus cases, the FJDF is bimodal for both cases further downstream ($x/d = 23.6$) and the two SGS scalars are positively correlated. These results show that similar to two-scalar mixing [63, 67], the FJDF can be bimodal even when the JPDF is unimodal everywhere (Cases II and IV). The earlier appearance of the bimodal FJDF for Case IV is due to stronger SGS transport resulting from the SGS velocity and scalar fluctuation generated by the mean shear between the center stream and the annular stream and between the annular stream and the co-flow.

5.2 Cross-stream subgrid-scale profiles

The radial profiles of the mean SGS variances with filter width $\Delta = 0.53$ mm are shown in figure 5.6. They have similar shapes and peak locations to the scalar variances (figure 4.15). Similar to the variance of ϕ_1, the peak location of $\langle\langle\phi_1''^2\rangle_L\rangle$ moves towards the centerline as x/d increases. The peak value of $\langle\langle\phi_1''^2\rangle_L\rangle$ decreases as x/d increases for all cases, whereas the peak value of ϕ_1 variance for Case III increases from $x/d = 3.29$ to $x/d = 6.99$. This difference is likely because that the scalar integral length scale increases with x/d; for a fixed filter width, the fraction of

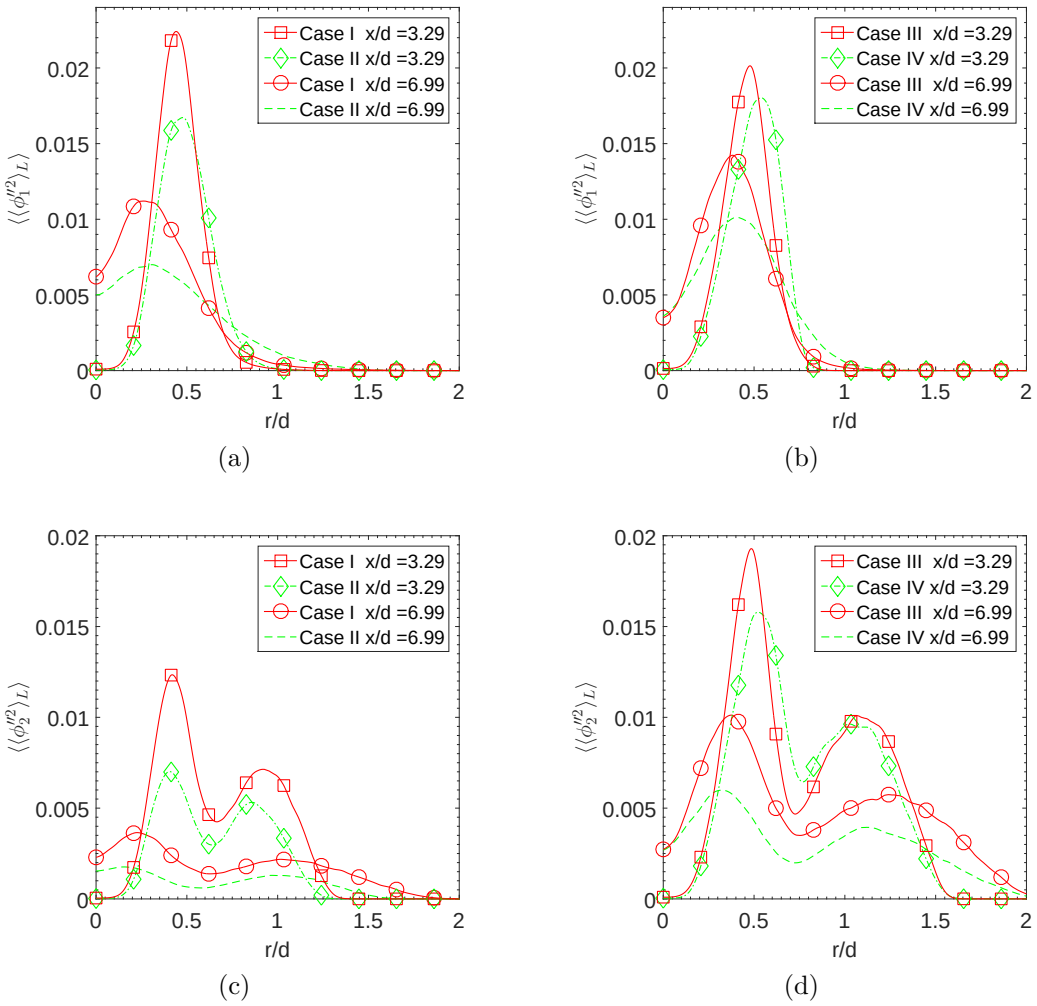

Figure 5.6: Cross-stream filtered mean SGS variance profiles. The filter width Δ is 0.53 mm.

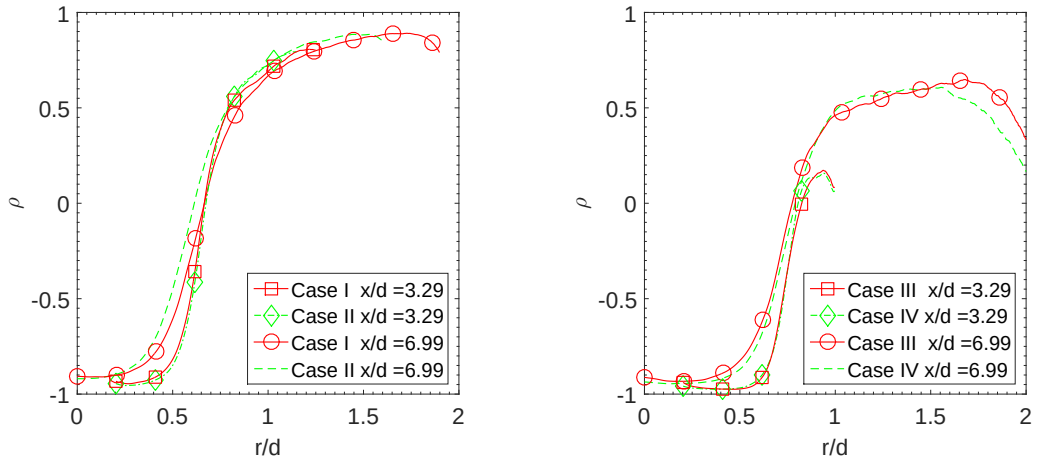

(a) (b)

Figure 5.7: Cross-stream filtered correlation coefficient between ϕ_1 and ϕ_2. The filter width Δ is 0.53 mm.

the variance contained in the subgrid scales decreases. The mean SGS variance of ϕ_2 also have the same trend as the variance of ϕ_2 (figure 4.15). The peak values decrease with increasing x/d. The mean SGS variance, however, decreases faster than the variance due to the increase of the integral length scale. The relative magnitudes of the mean SGS variances among the cases are also similar to those of scalar variances. The peak values of both ϕ_1 and ϕ_2 mean SGS variances are smaller and decrease faster for Case II (IV) than for Case I (III). However, the profiles of $\langle\langle\phi_1''^2\rangle_L\rangle$ are wider for Case II (IV) than for Case I (III). The peak values are generally smaller and decrease faster for the smaller annulus cases than for the larger annulus cases, except that the peak value of $\langle\langle\phi_1''^2\rangle_L\rangle$ at $x/d = 3.29$ is larger for Case I than for Case III. The general trends for the other filter width are similar but with different magnitudes.

The filtered correlation coefficient between ϕ_1 and ϕ_2, $\rho = \frac{\langle\langle\phi_1''\phi_2''\rangle_L\rangle}{\langle\langle\phi_1''^2\rangle_L\rangle^{\frac{1}{2}}\langle\langle\phi_1''^2\rangle_L\rangle^{\frac{1}{2}}}$, is shown in figure 5.7. The correlation coefficient generally has the value of negative one close to the centerline, increasing toward unity far away from the centerline. Close

to the centerline, ϕ_1 and ϕ_2 are anti-correlated ($\rho \approx -1$) because there is virtually no ϕ_3. It begins to increase when ϕ_1 and ϕ_2 begin to mix with ϕ_3, and approaches unity far away from the centerline, indicating that the two scalars are well mixed and their fluctuations are in phase. At $x/d = 3.29$, the results for both close to the centerline and toward the edge of the jet (at approximately $r/d = 1$) are not shown, because the correlation coefficient evolves toward zero due to the measurement uncertainties. The correlation coefficient begins to increase at smaller r/d values at $x/d = 6.99$ than at $x/d = 3.29$, resulting from the progression of scalar mixing. The differences between Cases I and II and between Cases III and IV are small. Comparisons between Cases I and III and between Cases II and IV show that the evolution of the correlation coefficient is much slower for the larger annulus than for the smaller annulus.

5.3 Cross-stream FJDF and conditionally filtered diffusion

In this section, the FJDF and the conditionally filtered diffusion at two downstream locations ($x/d = 3.29$ and 6.99) in the near field of the coaxial jet would be shown. The conditionally filtered diffusion is given as conditional means,

$\langle\langle D_1\nabla^2\phi_1|\hat{\phi}_1,\hat{\phi}_2\rangle_L|\langle\phi_1\rangle_L,\langle\phi_1''^2\rangle_L\rangle$ and $\langle\langle D_2\nabla^2\phi_2|\hat{\phi}_1,\hat{\phi}_2\rangle_L|\langle\phi_1\rangle_L,\langle\phi_1''^2\rangle_L\rangle$. The conditionally filtered scalar diffusion terms in the FJDF equation transport the FJDF in the scalar space; therefore, the conditionally filtered diffusion represents the two components of a diffusion (or transport) velocity. The conditionally filtered diffusion is presented as the diffusion velocity, represented by streamlines and magnitudes (using isocontours). Both conditionally filtered diffusion terms are non-dimensionized by the square root of ϕ_1 SGS variance and the conditionally filtered dissipation time

scale for ϕ_1, $\frac{\langle \phi_1''^2 \rangle_L}{\langle \langle \chi_1 \rangle_L | \langle \phi_1 \rangle_L, \langle \phi_1''^2 \rangle_L \rangle}$.

At $x/d = 3.29$, close to the jet centerline (not shown) the FJDF is largely limited to the ϕ_1-ϕ_2 mixing line. The spread of FJDF is largely due to the measurement uncertainties. For small SGS variance at $r/d = 0.372$ (figure 5.8), the FJDF is unimodal with the peak near the ϕ_1-ϕ_2 mixing line. The diffusion streamlines converge to the peak of the FJDF. At $r/d = 0.496$, the FJDF still has a Gaussian-like shape but the peak has already moved away from the ϕ_1-ϕ_2 mixing line, indicating that ϕ_1 and ϕ_2 are well mixed and there is some co-flow air present. The diffusion streamlines again converge to the stagnation point near $(\langle \phi_1 \rangle_L, \langle \langle \phi_2 \rangle_L | \langle \phi_1 \rangle_L, \langle \phi_1''^2 \rangle_L \rangle)$, which is again the peak of FJDF. Further away from the centerline (at $r/d = 0.703$), the peak of the FJDF moves closer to (0,0), consistent with the evolution of the filtered mean values. The general trends for other cases are also similar (figures not shown).

For large SGS variance (generally more than four times the mean SGS variance), the FJDF close to the centerline (not shown) is concentrated at (1, 0) with a tail extending toward (0, 1), indicating that the SGS mixing is largely limited to between ϕ_1 and ϕ_2 but with only a small amount of ϕ_2. At $r/d = 0.372$ (figure 5.9), the FJDF begins to extend toward (0, 0) for both Cases I and II. A diffusion manifold begins to emerge, and the diffusion streamlines converge to a stagnation point that is different from both the local filtered mean scalars and the peak of FJDF. For Case II, it appears a second peak begins to emerge on the left hand side of the FJDF. At $r/d = 0.496$ (figure 5.10), the FJDF has become bimodal for both Cases I and II with the bimodality of Case I stronger, consistent with the larger SGS variance for Case I. The right peak is close to the ϕ_1-ϕ_2 mixing line without much ϕ_3, while the left peak contains little ϕ_1, indicating that the two mixtures coming from the two mixing layers are segregated with a sharp interface between them within the grid cell. The diffusion streamlines first move towards a well defined and bell-shaped manifold,

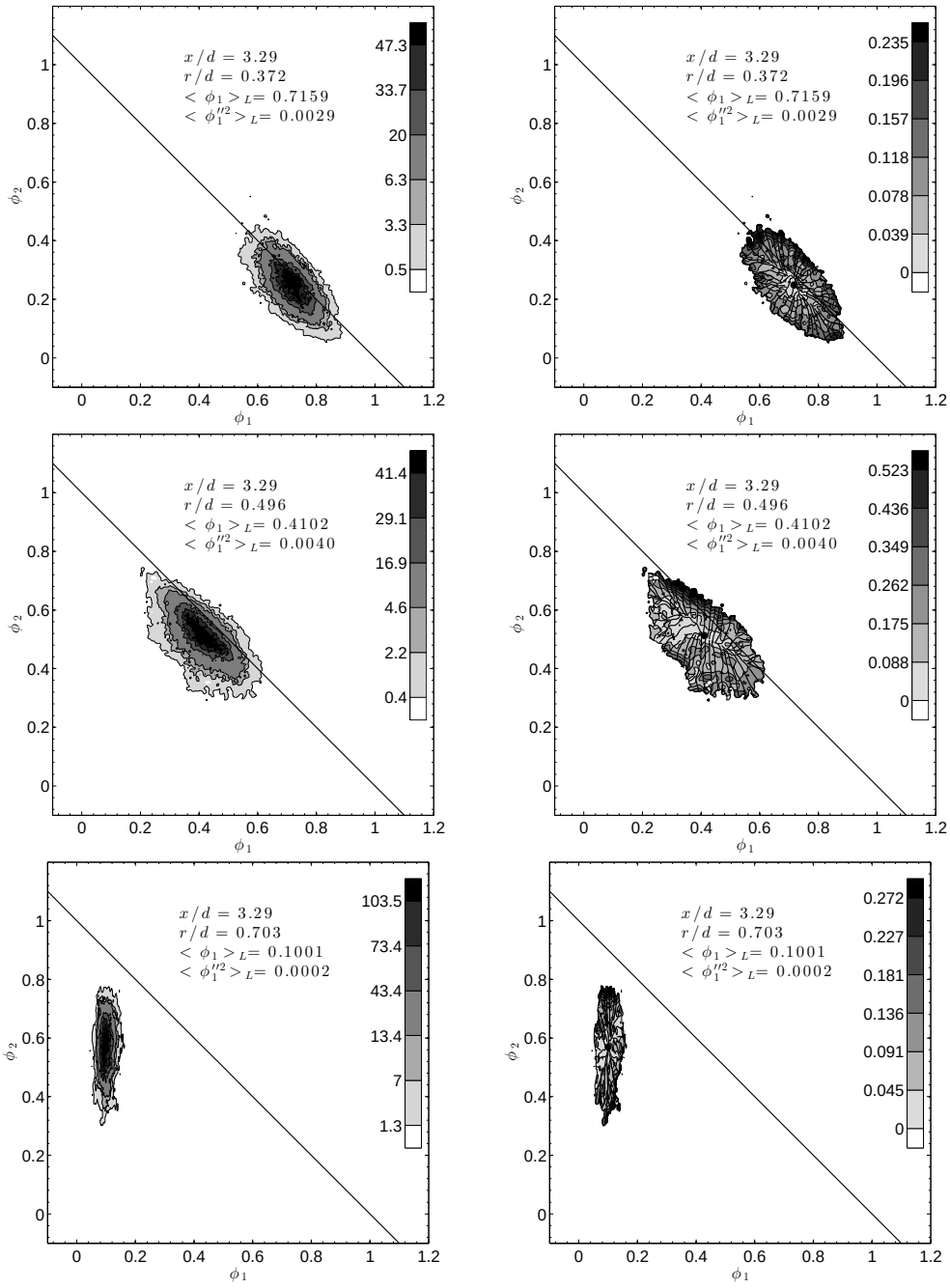

Figure 5.8: FJDF (Left) and conditionally filtered diffusion streamlines (Right) conditional on the small SGS variance at $x/d = 3.29$ for Case I. The filtered scalar values ($\langle\phi_1\rangle_L$, $\langle\langle\phi_2\rangle_L|\langle\phi_1\rangle_L, \langle\phi_1''^2\rangle_L\rangle$) are denoted by a bullet in the streamline figures.

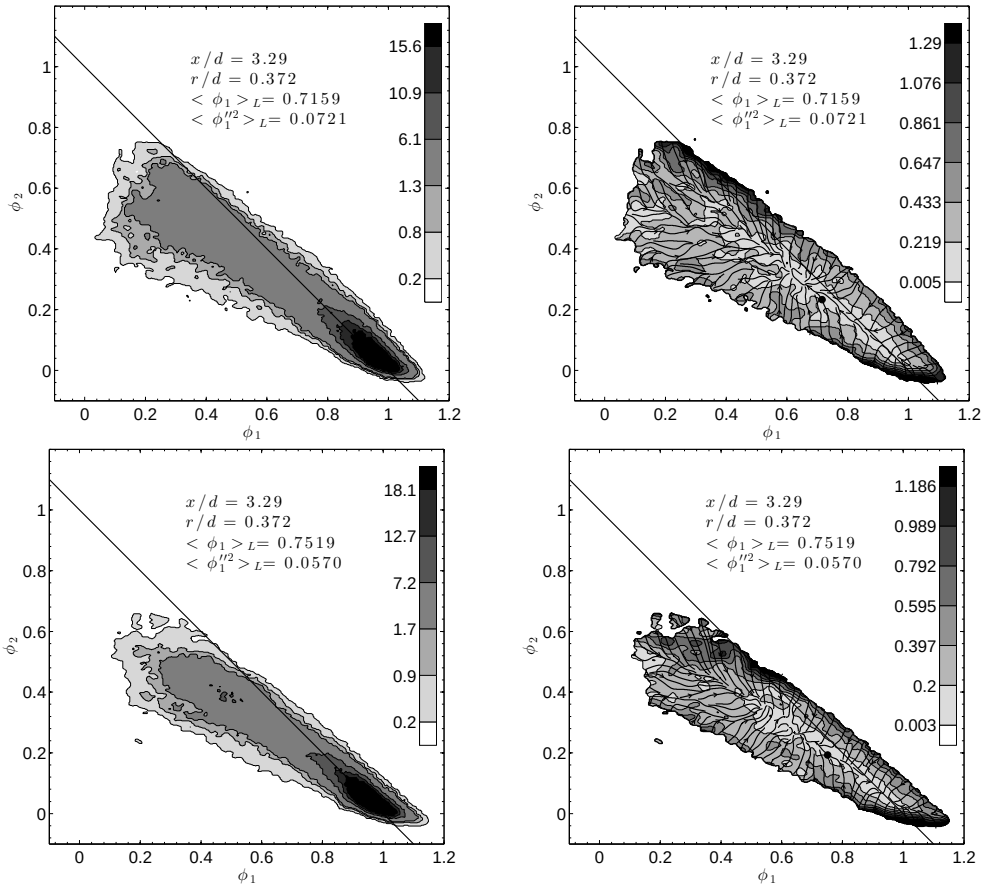

Figure 5.9: FJDF (Left) and conditionally filtered diffusion streamlines (Right) conditional on the large SGS variance at $x/d = 3.29$ and $r/d = 0.372$ for Case I (Top) and Case II (Bottom).

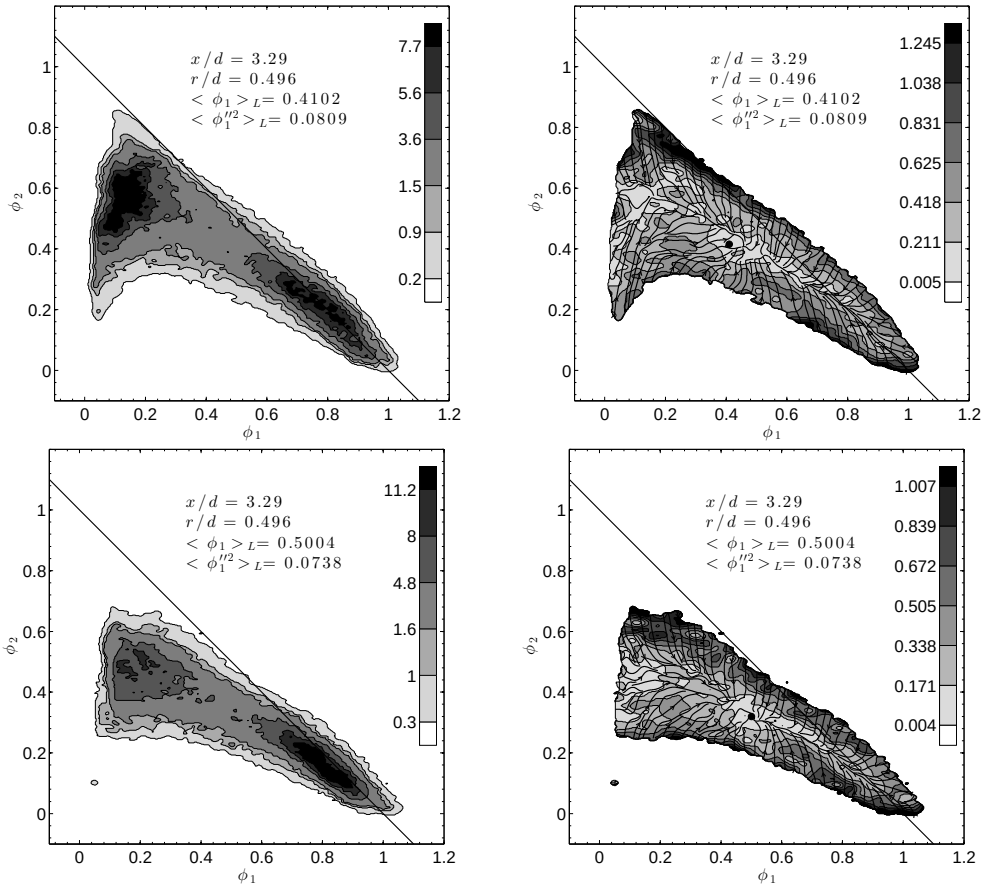

Figure 5.10: FJDF (Left) and conditionally filtered diffusion streamlines (Right) conditional on the large SGS variance at $x/d = 3.29$ and $r/d = 0.496$ for Case I (Top) and Case II (Bottom).

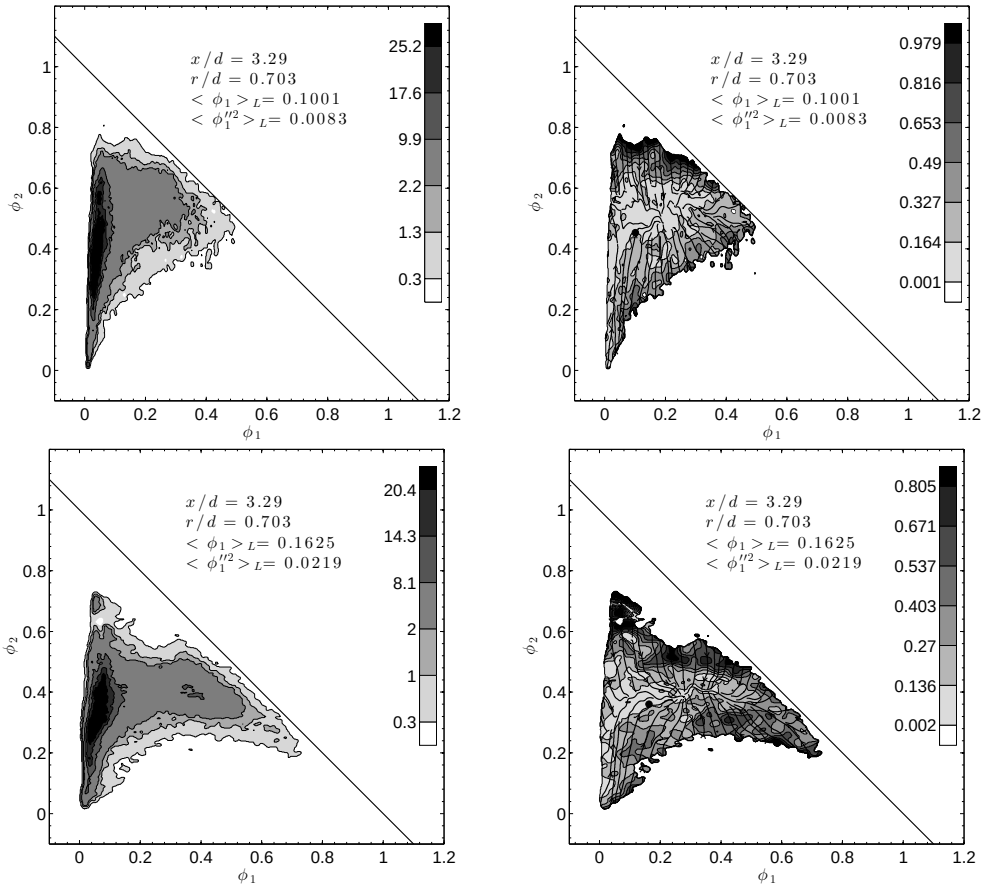

Figure 5.11: FJDF (Left) and conditionally filtered diffusion streamlines (Right) conditional on the large SGS variance at $x/d = 3.29$ and $r/d = 0.703$ for Case I (Top) and Case II (Bottom).

then continue along it to a stagnation point, which is again different from the filtered mean composition. Thus, the SGS scalars for large SGS variance have a structure due to the mixing configuration of the coaxial jet whereas for small SGS variance the three scalars are quite well mixed. The curvature of the manifold appears to be larger for Case I than for Case II. Further away from the centerline, the right peak of the FJDF becomes weaker. At $r/d = 0.703$ (figure 5.11), the right peak completely disappears for Case I whereas a weak right peak still exists for Case II, indicating that the bimodal FJDF exists over a wider range of physical locations for Case II. This trend is different from the cross-stream evolution of JPDF since the JPDF is bimodal at some locations for Case I whereas it is always unimodal for Case II (figure 4.21). The left peak of the FJDF has already moved very close to (0,0) but with a tail bending toward (1,0). The streamlines converge directly to a stagnation point from larger ϕ_1 values (from the right), but appear to move to a manifold first from smaller ϕ_1 values (from the left) and then approach the stagnation point. The FJDF would also become unimodal for Case II further away from the centerline.

Moving downstream to $x/d = 6.99$, some co-flow air has reached the centerline. For small SGS variance, the conditional FJDF (not shown) has a Gaussian-like shape and is concentrated near the filtered mean scalar values. The conditionally filtered diffusion streamlines (also not shown) mostly converge to a stagnation point. The evolution of the FJDF and the diffusion streamlines with increasing r/d values is similar to those at $x/d = 3.29$. The FJDF and the conditionally filtered diffusion again indicate that the SGS scalars are relative well-mixed.

For large SGS variance, the FJDF on the jet centerline (figure 5.4) is still concentrated near (1, 0), but extends further away from it, indicating the penetration of both ϕ_2 and ϕ_3. Moving away from the centerline, the FJDF extends further towards lower ϕ_1 values and bends further toward (0,0). A second peak begins to

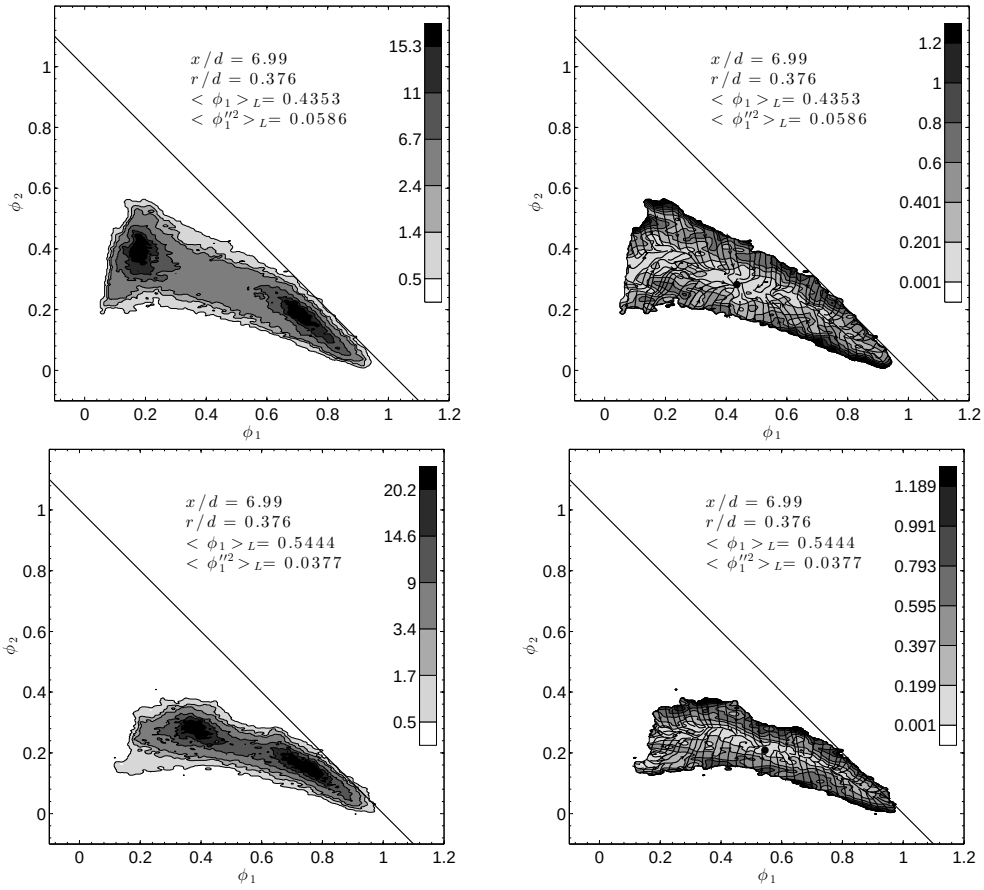

Figure 5.12: FJDF (Left) and conditionally filtered diffusion streamlines (Right) conditional on the large SGS variance at $x/d = 6.99$ and $r/d = 0.376$ for Case I (Top) and Case II (Bottom).

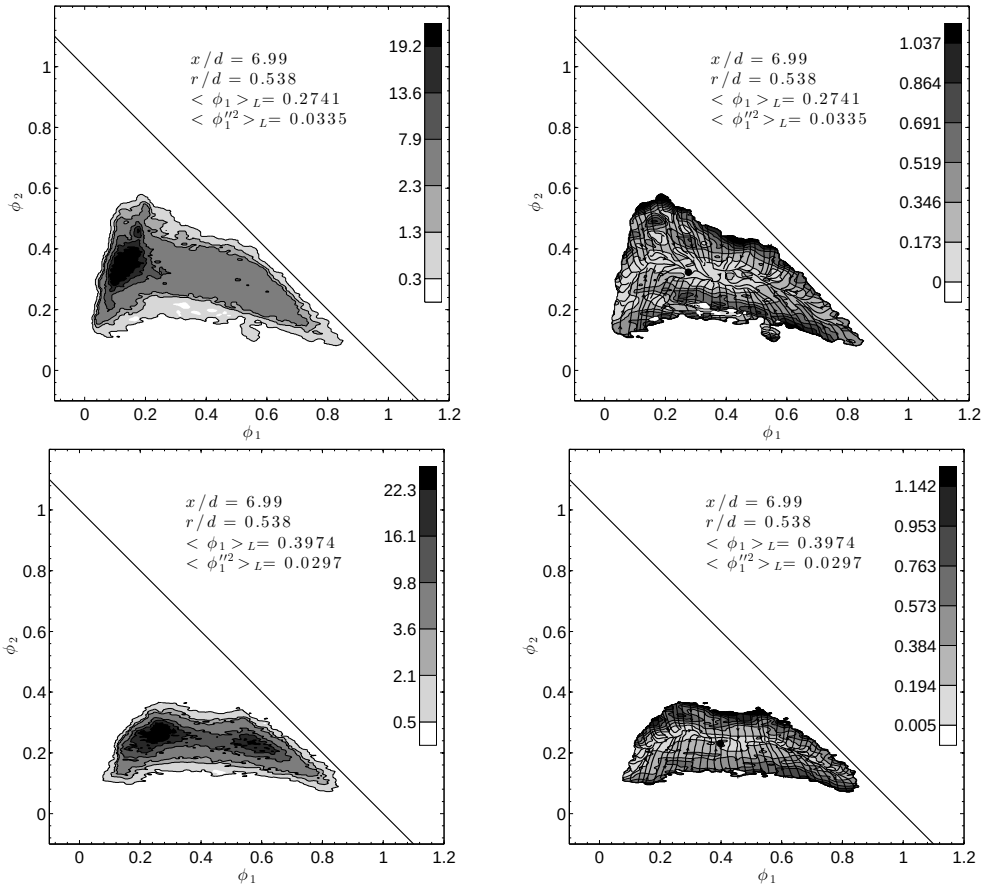

Figure 5.13: FJDF (Left) and conditionally filtered diffusion streamlines (Right) conditional on the large SGS variance at $x/d = 6.99$ and $r/d = 0.538$ for Case I (Top) and Case II (Bottom).

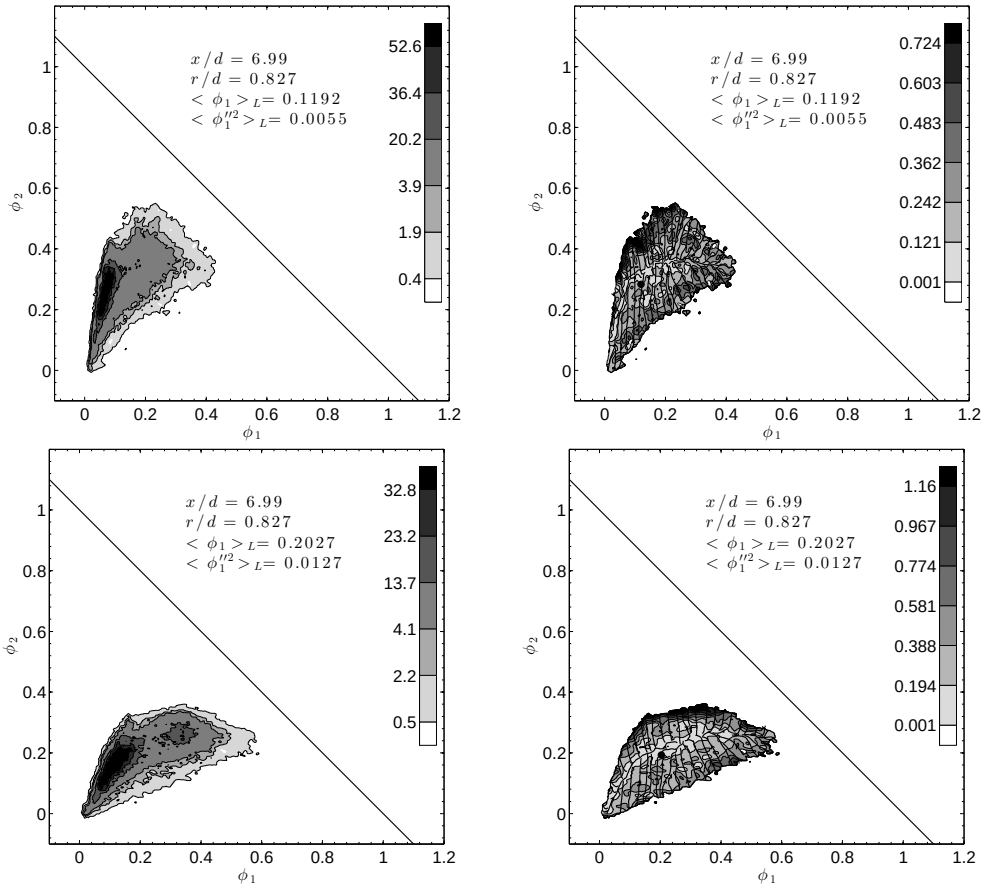

Figure 5.14: FJDF (Left) and conditionally filtered diffusion streamlines (Right) conditional on the large SGS variance at $x/d = 6.99$ and $r/d = 0.827$ for Case I (Top) and Case II (Bottom).

emerge and the FJDF becomes bimodal at $r/d = 0.248$ and $r/d = 0.207$ for Case I and Case II (figures not shown), respectively. At $r/d = 0.376$ (figure 5.12), the FJDF is strongly bimodal for both Cases I and II with ϕ_1'' and ϕ_2'' negatively correlated. The left side of the FJDF bend down toward (0, 0). The right peak is still close to the mixing line, whereas the left peak is well below it, indicating that the SGS field contains predominately the ϕ_1-ϕ_2 mixture and the ϕ_1-ϕ_2-ϕ_3 mixture coming from the two mixing layers. Again the mixtures are segregated with a sharp interface between them. The diffusion streamlines first converge to a manifold, which is close to the ridgeline of the FJDF. They then continue on the manifold at a lower rate toward a stagnation point between the FJDF peaks. Further away from the centerline, the FJDF extends further towards (0, 0). At $r/d = 0.538$ (figure 5.13), the FJDF becomes unimodal for Case I whereas it is still bimodal for Case II, although the SGS variance is again smaller for Case II. There is a well defined curved manifold for the conditional diffusion for each case. Towards the edge of the jet ($r/d = 0.827$), the FJDF is still bimodal for Case II but with ϕ_1'' and ϕ_2'' positively correlated (figure 5.14). The peak of FJDF for Case I and the left peak for Case II are very close to (0,0) but with a tail bending toward (1,0). For Case I, the diffusion streamlines to the left of the stagnation point converge to a manifold, and then to the stagnation point whereas those to the right of it converge to it. For Case II, the curved manifold is better defined. Moving further away from the centerline, the FJDF is also unimodal for Case II (not shown).

For the larger annulus at $x/d = 3.29$ (figure 5.15), the general trends are similar to the smaller annulus cases. The main difference is that the peak of the FJDF evolves along the ϕ_1-ϕ_2 mixing line and reaches (0,1) before bending toward (0,0). At $r/d = 0.331$, the FJDF peak near (1,0) while the ridgeline stay exactly on the ϕ_1-ϕ_2 mixing line. The FJDF is unimodal for Case III whereas a second peak

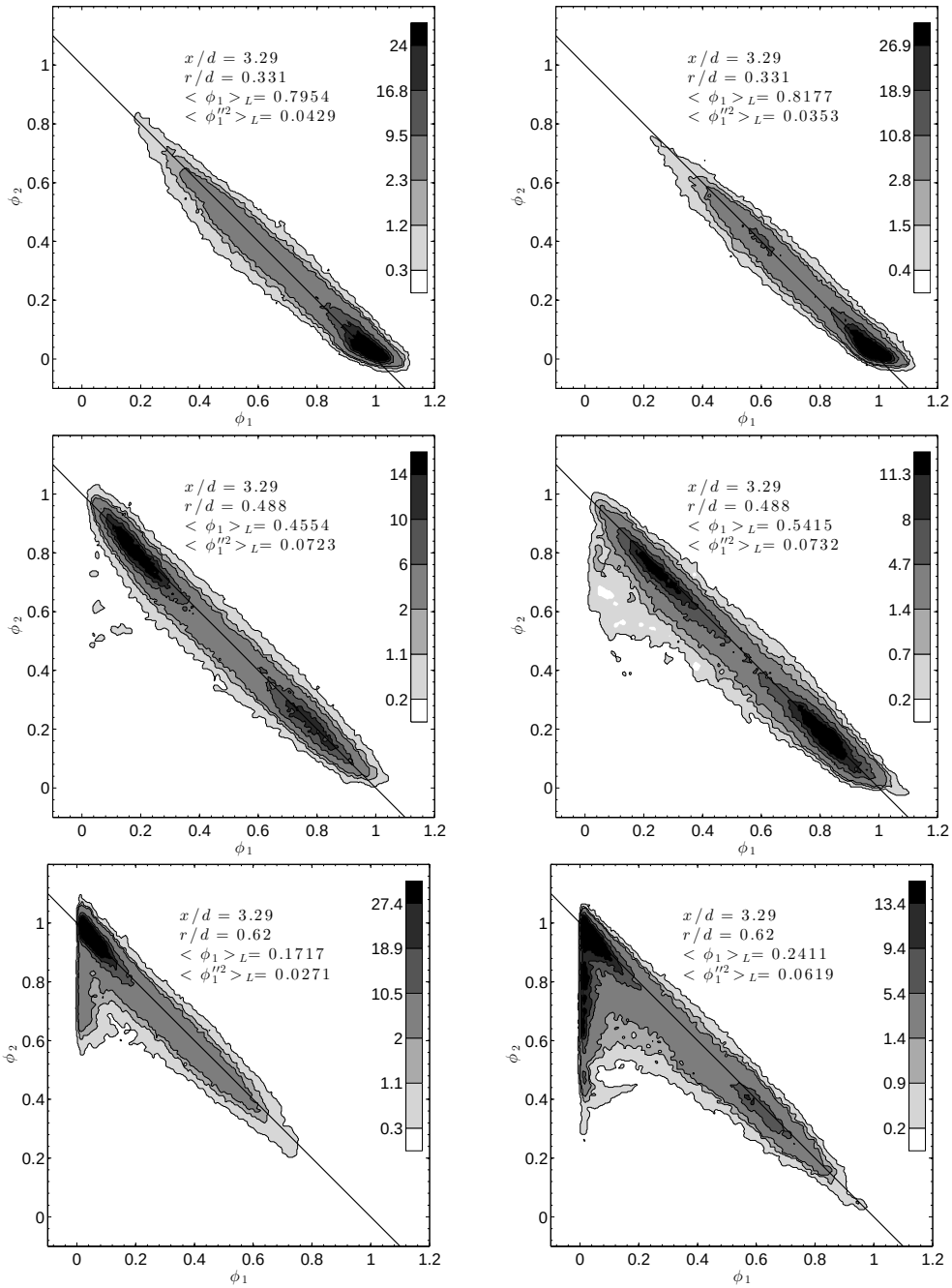

Figure 5.15: FJDF conditional on the larger SGS variance at $x/d = 3.29$ for Case III (Left) and Case IV (Right).

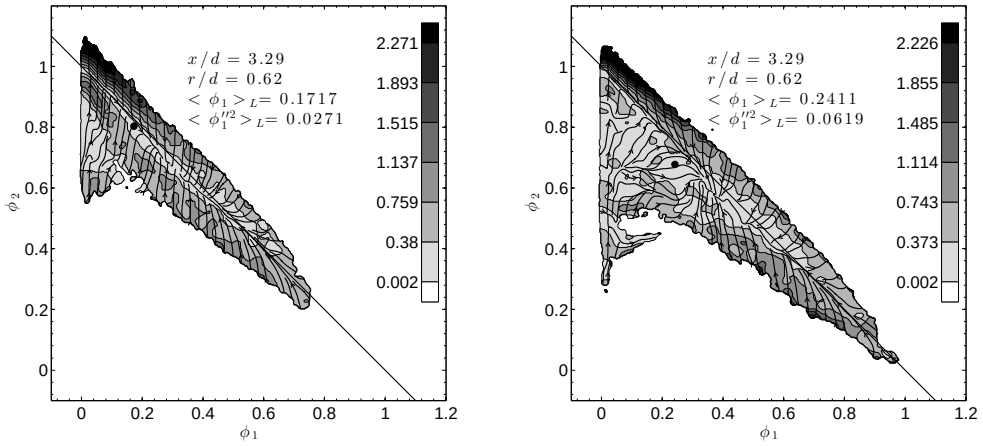

Figure 5.16: Conditionally filtered diffusion streamlines conditional on the large SGS variance at $x/d = 3.29$ and $r/d = 0.62$ for Case III (Left) and Case IV (Right).

begins to emerge on the left for Case IV. It is strongly bimodal for both Cases III and IV at $r/d = 0.488$. The FJDF is symmetric with respect to the ϕ_1-ϕ_2 mixing line for Case III whereas it extends toward (0,0) on the left for Case IV. The right peak disappears for Case III at $r/d = 0.62$ whereas a weak right peak still exists for Case IV. The peak near (0,1) indicates ϕ_1 and ϕ_3 are separated by pure ϕ_2, and there are two separate mostly binary mixing processes. A diffusion manifold begins to emerge for Case IV at $r/d = 0.62$ (figure 5.16), whereas no sign of a curved manifold for Case III. The FJDF would also become unimodal for Case IV moving further away from the centerline.

For the larger annulus at $x/d = 6.99$ (figure 5.17,5.18,5.19), the general trends are again similar to the smaller annulus cases. The bimodal FJDF exist over a wider range of physical locations for Case IV than for Case III, again different from the trend of JPDF. The curvature of the diffusion manifold is also larger for Case III than for Case IV, consistent with better mixing for Case IV.

The above results show that the strongest bimodal FJDF occurs in Cases I

and III at locations near the peaks of the mean SGS variance of ϕ_1. These cases have higher peak mean SGS variance values than Cases II and IV. The strongest bimodal JPDF also occurs (in Cases I and III, which have higher peak scalar variance values) near the peaks of the variance of ϕ_1. Therefore, a higher variance (mean SGS variance) is conducive to a bimodal JPDF (FJDF). On the other hand, the FJDF is bimodal over a wider range of physical locations for Cases II and IV than for Cases I and III, in spite of the weaker bimodality at the location of the peak mean SGS variance. Furthermore, while Cases II and IV have wider SGS variance profiles with higher values toward the edge of the jets than Cases I and III, thereby favoring bimodal FJDF, there are also instances (e.g. at $x/d = 3.29$ and $r/d = 0.372$ for the smaller annulus shown in figure 5.9) where the FJDF is unimodal for Case I (larger mean SGS variance) and is bimodal for Case II (relatively smaller SGS variance). Therefore, the SGS variance is only one important factor determining the bimodality of the FJDF. The other important factor is the length scales of the turbulent fluctuations, which influence the SGS scalar structure. Cases II and IV have two shear layers; therefore, the length scales of the turbulent (both velocity and scalar) fluctuations are smaller than Cases I and III, which have a single shear layer. Therefore, for a given filter width and SGS variance value, the large-scale fluctuations for Cases II and IV have a stronger influence on the SGS structure, and are more likely to result in a bimodal FJDF.

Similar to the conditional diffusion for the JPDF, for large SGS variance the diffusion streamlines first converge to a manifold and then continue along it towards a stagnation point. Thus, there are also two mixing processes in the SGS mixing, one slow and one fast. This phenomenon is related to the structure of the SGS scalars, in which ϕ_1 is dominated by a ramp-cliff structure [63, 67] and ϕ_2 by a Gaussian-like scalar profile, both large-scale structures. Ramp-cliff structures are generated by

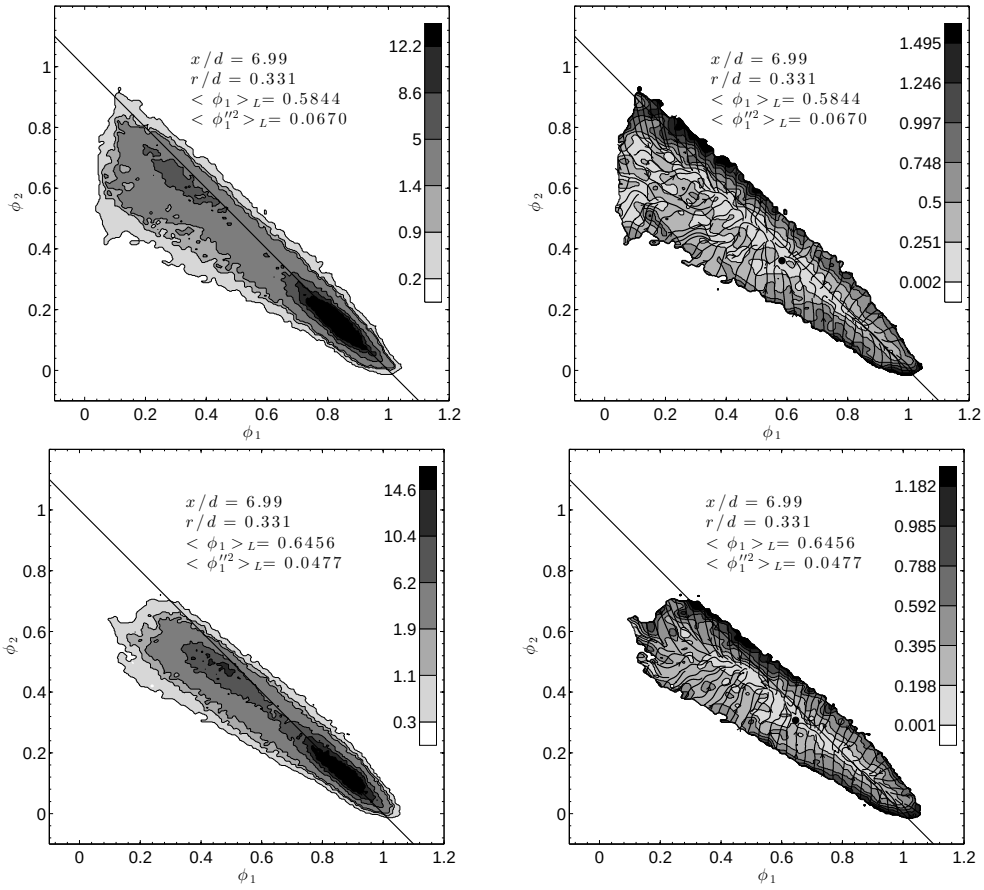

Figure 5.17: FJDF (Left) and conditionally filtered diffusion streamlines (Right) conditional on the large SGS variance at $x/d = 6.99$ and $r/d = 0.331$ for Case III (Top) and Case IV (Bottom).

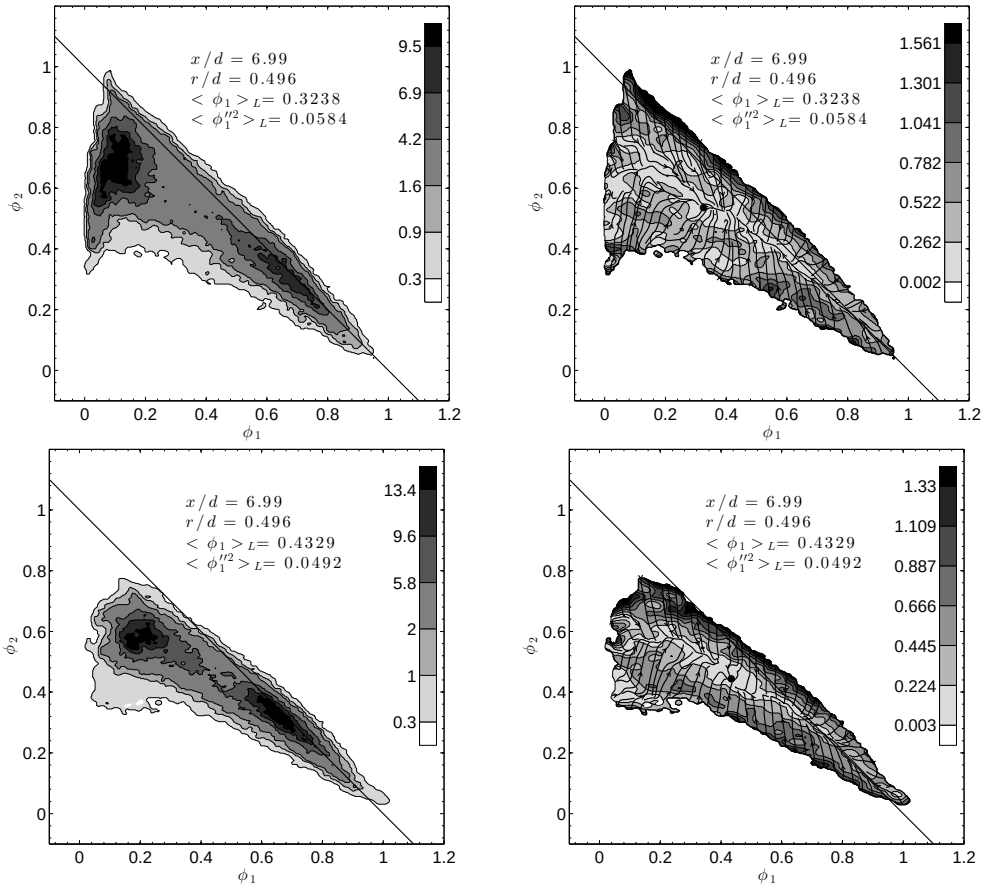

Figure 5.18: FJDF (Left) and conditionally filtered diffusion streamlines (Right) conditional on the large SGS variance at $x/d = 6.99$ and $r/d = 0.496$ for Case III (Top) and Case IV (Bottom).

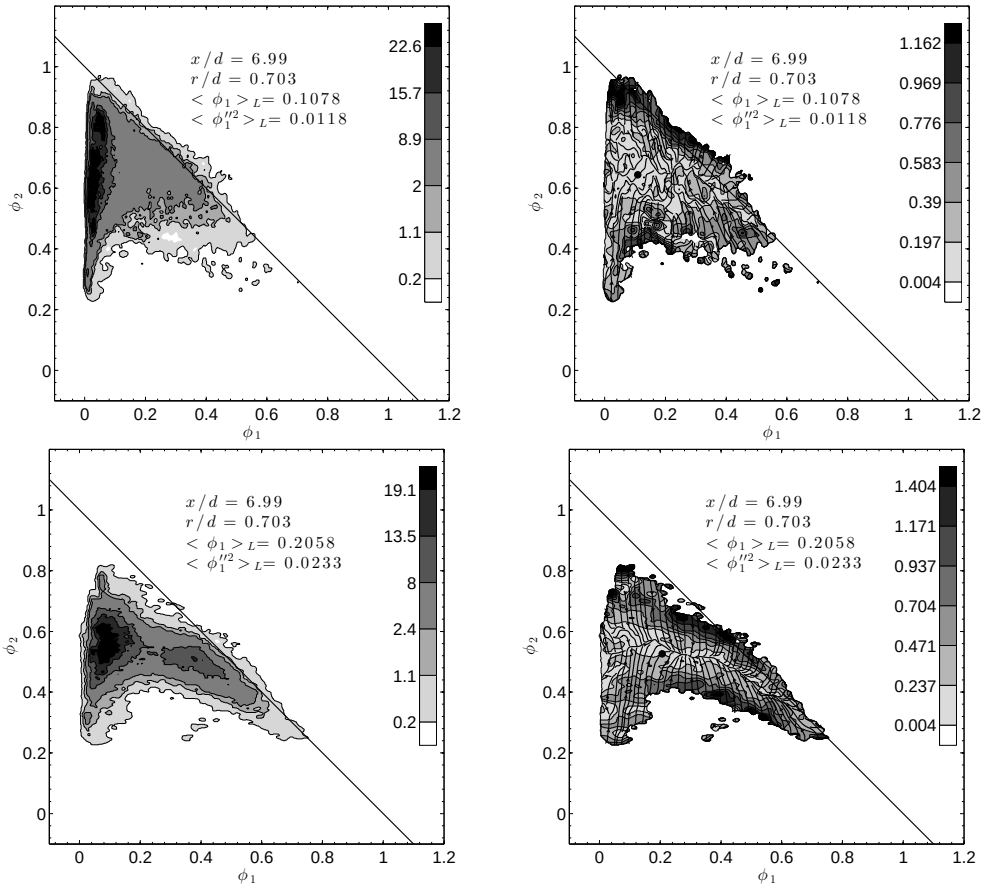

Figure 5.19: FJDF (Left) and conditionally filtered diffusion streamlines (Right) conditional on the large SGS variance at $x/d = 6.99$ and $r/d = 0.703$ for Case III (Top) and Case IV (Bottom).

large-scale convergent-divergent separatrix [20, 64] acting on a mean (or large-scale) scalar gradient. The large-scale scalar structures in ϕ_2 are also likely due to the same reason. Smaller scalar fluctuations can be viewed as being superimposed on these structures. These fluctuations are likely due to mixing of small-scale homogeneous scalar fields by velocity fluctuations of smaller scales. Thus, the scalars diffuse (relax) towards the large structures first before the diffusion of these structures move the streamlines towards the stagnation point. Thus, the slow and fast processes in SGS mixing are likely the results of large- and small- scale velocity fluctuations acting on large- and small-scale scalar gradients respectively. The large-scale scalar structures also form a mixing path in the scalar space along which mixing of ϕ_1 and ϕ_3 occurs.

5.4 Cross-stream conditionally filtered dissipation and cross-dissipation

This section would discuss the conditionally filtered dissipation, which are also given as conditional means, $\langle\langle\chi_i|\hat{\phi}_1,\hat{\phi}_2\rangle_L|\langle\phi_1\rangle_L,\langle\phi_1''^2\rangle_L\rangle$ and $\langle\langle\chi_{12}|\hat{\phi}_1,\hat{\phi}_2\rangle_L|\langle\phi_1\rangle_L,\langle\phi_1''^2\rangle_L\rangle$. For convenience, the conditionally filtered dissipation and cross-dissipation are referred to as $\langle\chi_i|\phi_1,\phi_2\rangle_L$ and $\langle\chi_{12}|\phi_1,\phi_2\rangle_L$ hereafter. The conditionally filtered dissipation rates are non-dimensionized by the maximum ϕ_1 mean dissipation rates at the same x/d location.

For small SGS variance, the conditionally filtered conditional dissipation rates for ϕ_1 and ϕ_2 share a similar pattern close to the centerline (not shown). The dissipation rates are small close to (1, 0) and increase towards (0, 1). These similarities are because there is no co-flow air at this location and the SGS mixing is only between ϕ_1 and ϕ_2. Thus, their fluctuations have equal magnitudes but are anti-correlated,

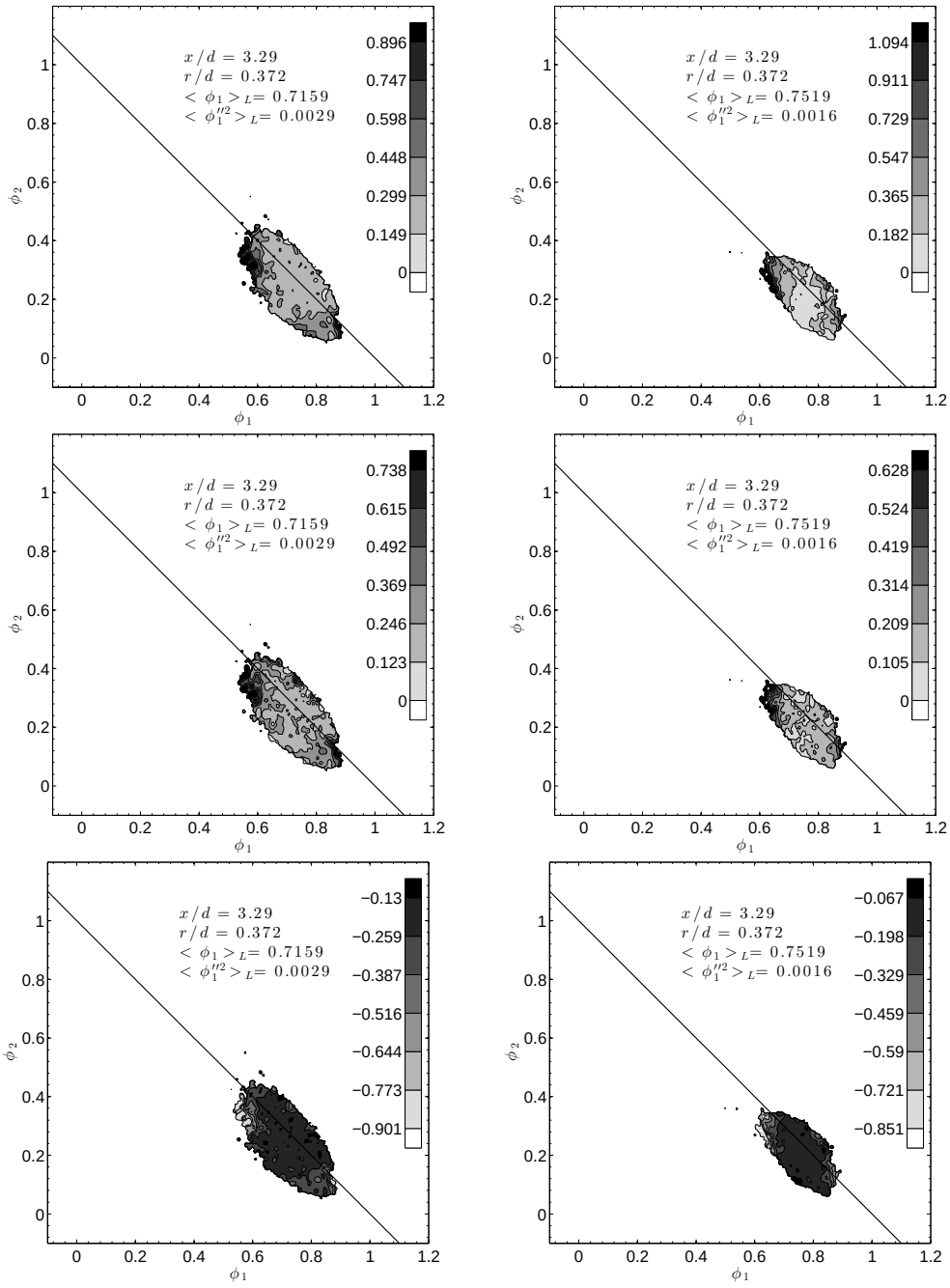

Figure 5.20: Conditionally filtered dissipation conditional on the small SGS variance at $x/d = 3.29$ and $r/d = 0.372$ for Case I (Left) and Case II (Right). The top, middle and bottom rows are for $\langle \chi_1 | \phi_1, \phi_2 \rangle_L$, $\langle \chi_2 | \phi_1, \phi_2 \rangle_L$, and $\langle \chi_{12} | \phi_1, \phi_2 \rangle_L$, respectively.

resulting in similar dissipation rates. The cross dissipation is also similar but has negative values due to the anti-correlation. For Case I at $r/d = 0.347$ (figure 5.20), both $\langle\chi_1|\phi_1,\phi_2\rangle_L$ and $\langle\chi_2|\phi_1,\phi_2\rangle_L$ as well as $\langle\chi_{12}|\phi_1,\phi_2\rangle_L$ are relatively uniform, consistent with the Gaussian-like FJDF since the SGS scalars are well mixed for small SGS variance. The cross-dissipation still has the same trend as $\langle\chi_1|\phi_1,\phi_2\rangle_L$ and $\langle\chi_2|\phi_1,\phi_2\rangle_L$, but with negative values due to the mixing being primarily between ϕ_1 and ϕ_2. The magnitudes are between those of $\langle\chi_1|\phi_1,\phi_2\rangle_L$ and $\langle\chi_2|\phi_1,\phi_2\rangle_L$. Moving toward the edge of the jet (figures not shown), the general trend is opposite to those close to the centerline, with the dissipation rates increasing with ϕ_1. The cross-dissipation also has the same general trend but with positive values.

For large SGS variance, $\langle\chi_1|\phi_1,\phi_2\rangle_L$ and $\langle\chi_2|\phi_1,\phi_2\rangle_L$ are generally higher than for small SGS variances. Close to the centerline (not shown), they are also higher on the mixing line towards (0, 1). They peak at the location in scalar space where the FJDF values are low, indicating that the large dissipation rates are rare events, perhaps a result of strong SGS motions transporting ϕ_2 to this physical location generating sharp interfaces. The cross-dissipation also has the same trend.

At $r/d = 0.372$ (figure 5.21), $\langle\chi_1|\phi_1,\phi_2\rangle_L$ peaks on the lower edge of the FJDF at intermediate ϕ_1 values, due to the SGS mixing of the ϕ_2-ϕ_3 mixture with ϕ_1. On the ϕ_1-ϕ_2 mixing line, both $\langle\chi_1|\phi_1,\phi_2\rangle_L$ and $\langle\chi_2|\phi_1,\phi_2\rangle_L$ are higher for intermediate ϕ_1 and ϕ_2 values because this location is near the mean ϕ_1-ϕ_2 interface. For $\langle\chi_2|\phi_1,\phi_2\rangle_L$ the peak on the mixing line is higher than that of $\langle\chi_1|\phi_1,\phi_2\rangle_L$ due to the higher ethylene diffusivity (the ϕ_1 and ϕ_2 gradients have the same magnitude). The lower edge value of $\langle\chi_2|\phi_1,\phi_2\rangle_L$ is lower than the $\langle\chi_1|\phi_1,\phi_2\rangle_L$ peak because the ϕ_2 values are approximately one half of the ϕ_1 value, hence the smaller ϕ_2 gradient and dissipation. The cross-dissipation has a similar trend with negative values. The strengths of the (negative) peaks are between those of $\langle\chi_1|\phi_1,\phi_2\rangle_L$ and $\langle\chi_2|\phi_1,\phi_2\rangle_L$. The conditionally

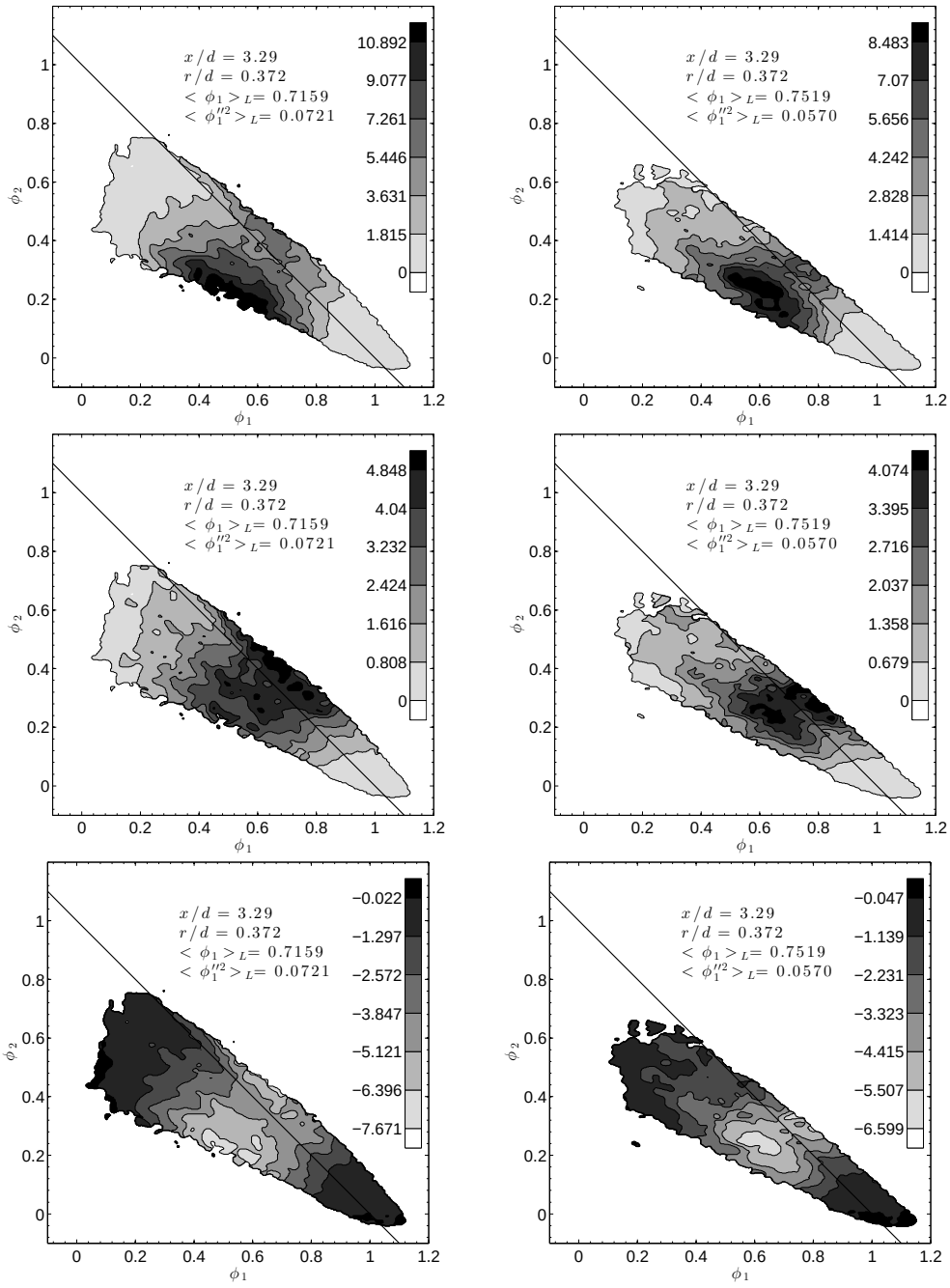

Figure 5.21: Conditionally filtered dissipation conditional on the large SGS variance at $x/d = 3.29$ and $r/d = 0.372$ for Case I (Left) and Case II (Right). The top, middle and bottom rows are for $\langle \chi_1 | \phi_1, \phi_2 \rangle_L$, $\langle \chi_2 | \phi_1, \phi_2 \rangle_L$, and $\langle \chi_{12} | \phi_1, \phi_2 \rangle_L$, respectively.

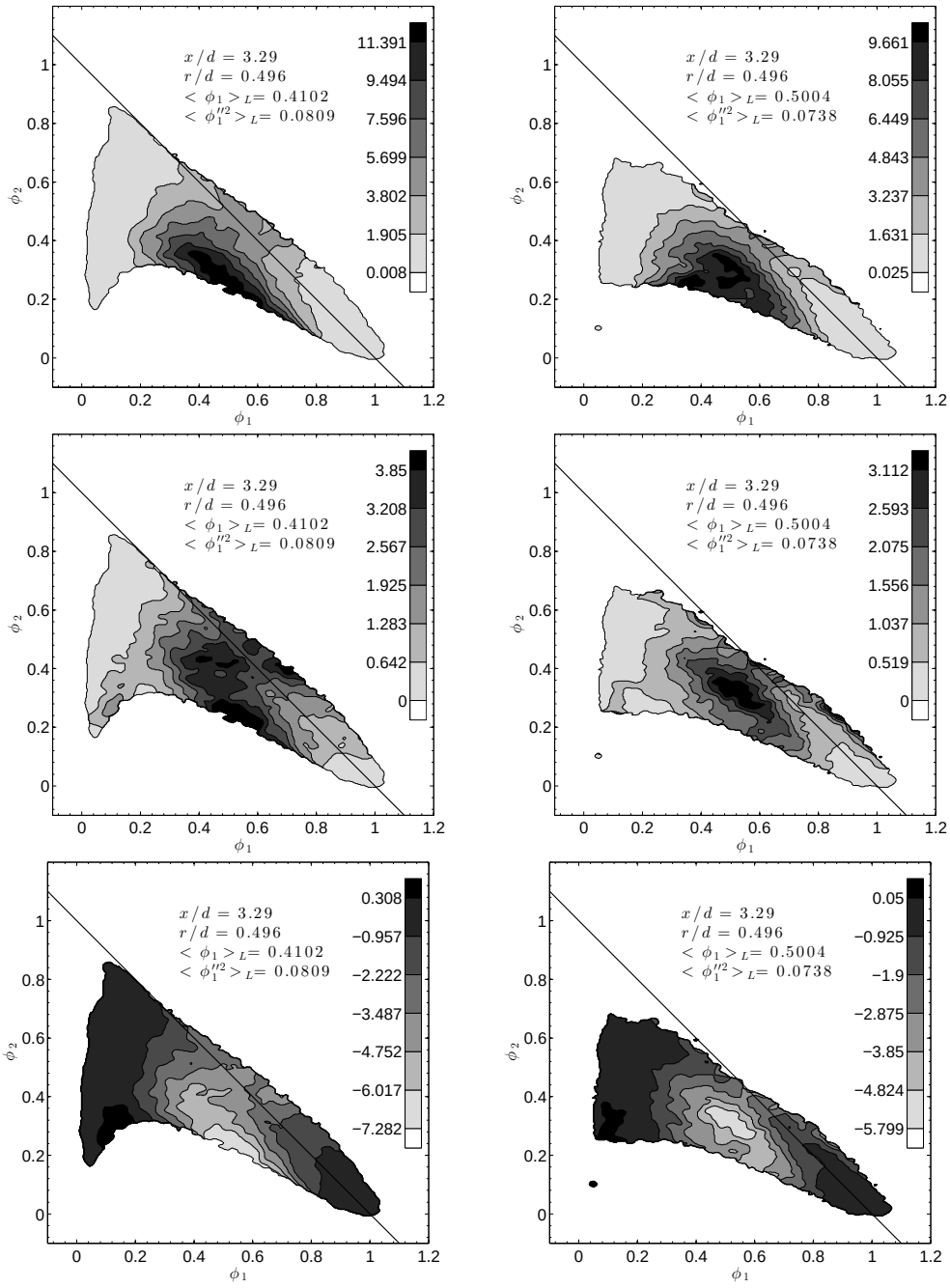

Figure 5.22: Conditionally filtered dissipation conditional on the large SGS variance at $x/d = 3.29$ and $r/d = 0.496$ for Case I (Left) and Case II (Right). The top, middle and bottom rows are for $\langle \chi_1 | \phi_1, \phi_2 \rangle_L$, $\langle \chi_2 | \phi_1, \phi_2 \rangle_L$, and $\langle \chi_{12} | \phi_1, \phi_2 \rangle_L$, respectively.

filtered dissipation rates and cross-dissipation rate for Case II have similar trends. However, the peak locations of both $\langle\chi_1|\phi_1,\phi_2\rangle_L$ and $\langle\chi_2|\phi_1,\phi_2\rangle_L$ for Case II shift to higher ϕ_1 and ϕ_2 values compared to those of Case I.

At $r/d = 0.496$ (figure 5.22), $\langle\chi_1|\phi_1,\phi_2\rangle_L$ still peak at the lower edge for Case I, indicating that the most intense SGS mixing occurs when large velocity fluctuations bringing together mixtures near the centerline ($\phi_1 = 1$) and far from the centerline (both ϕ_1 and ϕ_2 are low), producing a sharp interface, i.e., a ramp-cliff structure. The conditional dissipation, $\langle\chi_1|\phi_1,\phi_2\rangle$ (unfiltered), also has a peak near this location (figure 4.23). The peak of the conditionally filtered dissipation, however is stronger and exists for a wider range of r/d. Previous studies [67] have found that in the far field of turbulent round jets the scalar FDF is bimodal and there is a ramp-cliff structure when the SGS variance is large, even when the scalar PDF is unimodal. Thus, the bimodal FJDF and the peak in the conditionally filtered dissipation is primarily due to the ramp-cliff structure, whereas the bimodal JPDF is partly due to the flapping of ϕ_1 and the ϕ_2-ϕ_3 mixtures. At this location, $\langle\chi_2|\phi_1,\phi_2\rangle_L$ is still large on the mixing line, but with two peaks at the lower edge of the FJDF. These peaks are located on either side of the peak of $\langle\chi_1|\phi_1,\phi_2\rangle_L$ in the scalar space. In physical space the peak ϕ_2 is located approximately in the center part of the ramp-cliff structure, where the ϕ_2 dissipation is small, but on either side of the peak the ϕ_2 gradient is large, resulting in two dissipation peaks. The peaks are located in regions of low ϕ_2 values because for these intense mixing events, the ϕ_2 values are reduced by the co-flow air. The right peak of $\langle\chi_2|\phi_1,\phi_2\rangle_L$ is close to the $\langle\chi_1|\phi_1,\phi_2\rangle_L$ peak as they likely come from the same mixing events. Their locations (the maximum gradient) do not coincide due to the presence of the co-flow air. For Case II the peaks shift to higher ϕ_2 values, due to the shear layer between the ϕ_1-ϕ_2 streams enhancing mixing without transporting large amounts of ϕ_3.

The conditionally filtered cross-dissipation rate at this location has some of the characteristics of both $\langle\chi_1|\phi_1,\phi_2\rangle_L$ and $\langle\chi_2|\phi_1,\phi_2\rangle_L$. It has a negative peak close to that of $\langle\chi_1|\phi_1,\phi_2\rangle_L$, with magnitudes between those of $\langle\chi_1|\phi_1,\phi_2\rangle_L$ and the right peak of $\langle\chi_2|\phi_1,\phi_2\rangle_L$. It has a positive peak close to that of the left peak of $\langle\chi_2|\phi_1,\phi_2\rangle_L$. Here ϕ_1 and ϕ_2 are being mixed with ϕ_3, hence the positive cross-dissipation. The value, however, is much lower because ϕ_1 and $\langle\chi_1|\phi_1,\phi_2\rangle_L$ are low. The left peaks of both $\langle\chi_2|\phi_1,\phi_2\rangle_L$ and $\langle\chi_{12}|\phi_1,\phi_2\rangle_L$ are stronger for Case I than Case II.

Moving further towards the edge of the jet (figure not show), $\langle\chi_1|\phi_1,\phi_2\rangle_L$ and $\langle\chi_2|\phi_1,\phi_2\rangle_L$ have similar trends, each having a peak caused by the ϕ_1-ϕ_2 mixture mixing with ϕ_3. The cross-dissipation has the same trend as $\langle\chi_1|\phi_1,\phi_2\rangle_L$ and $\langle\chi_2|\phi_1,\phi_2\rangle_L$, and has positive values because ϕ_1 and ϕ_2 are well mixed and well correlated at this location.

The general trends for the larger annulus are similar to the smaller annulus. However, the peaks are located at higher ϕ_2 (closer to the ϕ_1-ϕ_2 mixing line) for Case III than for Case IV (e.g. at $x/d = 6.99$ and $r/d = 0.496$ shown in figure 5.23), which is opposite to the relative locations between Case I and Case II.

The results on the conditionally filtered dissipation suggest that there are several SGS mixing scenarios in the near field of the coaxial jets studied. The first involves mixing of ϕ_1 and the ϕ_2-ϕ_3 mixture, which is usually caused by relatively large SGS velocity fluctuations bringing ϕ_1 and ϕ_3 together, producing high dissipation rates. The second scenario involves primarily ϕ_1-ϕ_2 mixing, which generally does not require SGS velocity fluctuations as large as the first scenario. The dissipation rates, therefore, are lower than those in the first scenario. These two scenarios generally occur in most regions of the jet but the probability of their occurrence becomes very small towards the edge. The third scenario involves mixing of the ϕ_1-ϕ_2-ϕ_3 mixture with pure ϕ_3, and occurs primarily towards the edge of the jet.

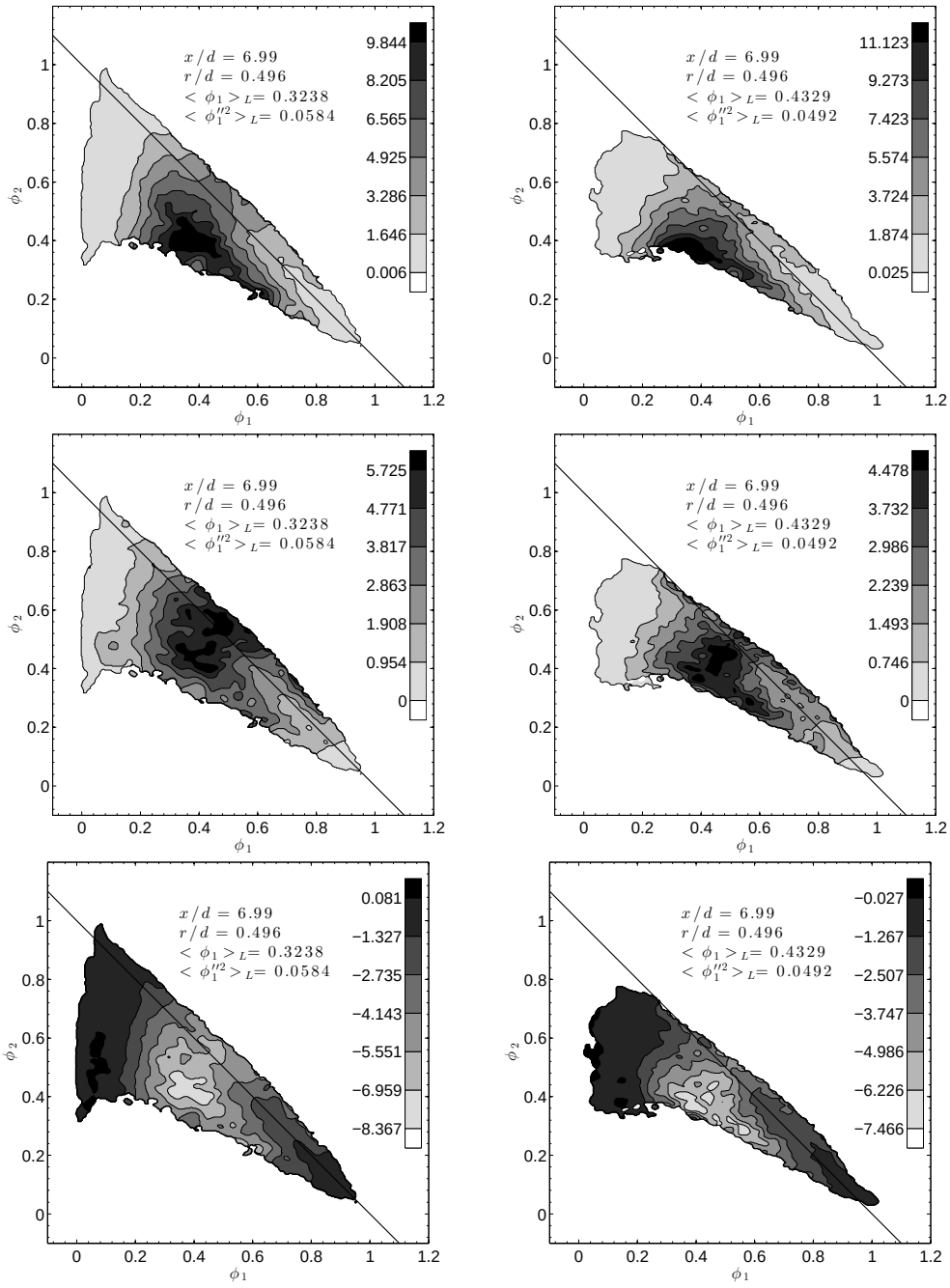

Figure 5.23: Conditionally filtered dissipation conditional on the large SGS variance at $x/d = 6.99$ and $r/d = 0.496$ for Case III (Left) and Case IV (Right). The top, middle and bottom rows are for $\langle \chi_1 | \phi_1, \phi_2 \rangle_L$, $\langle \chi_2 | \phi_1, \phi_2 \rangle_L$, and $\langle \chi_{12} | \phi_1, \phi_2 \rangle_L$, respectively.

While these mixing scenarios occur under general conditions, they manifest themselves more clearly when the SGS variance is large. For small SGS variance, the SGS scalars are relatively well mixed. The dissipation rates and their variations in the scalar space are quite moderate. For large SGS variance, the SGS fields contain the ramp-cliff structure for ϕ_1. The dissipation rates for both ϕ_1 and ϕ_2 are higher. In the first SGS mixing scenario, $\langle \chi_1 | \phi_1, \phi_2 \rangle_L$ has a peak near the center of the cliff and $\langle \chi_2 | \phi_1, \phi_2 \rangle_L$ has two peaks, one on each side of the $\langle \chi_1 | \phi_1, \phi_2 \rangle_L$ peak. These peaks are located in the part of the scalar space with relatively low ϕ_2 values, since a significant amount of air is brought in by the large SGS velocity fluctuations. In the second scenario the cliff for ϕ_1 is not as sharp as in the first scenario. Thus $\langle \chi_1 | \phi_1, \phi_2 \rangle_L$ might not have a peak in the scalar space. The overall pattern of the conditionally filtered dissipation rates are largely determined by the relative probability and the dissipation magnitudes of these SGS mixing scenarios.

The results also show that $\langle \chi_2 | \phi_1, \phi_2 \rangle_L$ is similar to the conditionally filtered temperature dissipation. In the jet there are two $\langle \chi_2 | \phi_1, \phi_2 \rangle_L$ peaks, one on each side of the peak of $\langle \chi_1 | \phi_1, \phi_2 \rangle_L$. These peaks are near the lower edge of the FJDF, due to the large dissipation lowering the ϕ_2 values. In flames, high temperature is generated between mixture fraction values of one (fuel stream, similar to $\phi_1 = 1$) and zero (air stream), thus having a similar mixing configuration as the three scalar mixing in the present turbulent coaxial jet. The temperature dissipation has peaks on both sides of the peak temperature in the scalar space [8]. Due to the heat release generating high temperatures, the locations of peaks relative to the FJDF peaks in the mixture fraction-temperature FJDF domain are much higher than those of the $\langle \chi_2 | \phi_1, \phi_2 \rangle_L$ in the ϕ_1-ϕ_2 FJDF domain. The temperature dissipation for the locally extinguished samples are more similar to $\langle \chi_2 | \phi_1, \phi_2 \rangle_L$ in the present study due to the lack of a temperature source.

Chapter 6

Conclusions

The effects of the velocity ratio (mean shear) and the length scale ratio on three-scalar mixing in turbulent coaxial jets are investigated. The mixing process in this flow closely approximates that in turbulent non-premixed reactive flows. The velocity ratio alters the relative mean shear rates in the mixing layers between the center jet and the annular flow and between the annular flow and the co-flow, modifying the scalar fields through mean-flow advection, turbulent transport, and small-scale mixing. The length scale ratio determines the degree of separation between the center jet and the co-flow.

For the cases with the higher velocity ratio (Cases I and III) the cross-stream mean profiles for ϕ_1 are narrower with the centerline values lower (the gradient is higher, however), primarily due to the smaller mean-flow advection resulting from the wider mean velocity profile and the higher centerline velocity. It is possible that the turbulent convection is also larger, further reducing the centerline value. The peak value of ϕ_2, on the other hand, is larger for these higher velocity ratio cases, due to the faster decrease of the mean streamwise velocity (here turbulent convection tends to lower the mean scalar). The rms scalar fluctuations are larger for both scalars for

Cases I and III, caused by the larger production rates due to the larger mean scalar gradients and the higher turbulent fluxes.

The effects of the velocity ratio and length-scale ratio on the evolution of the JPDF are a result of their altering the interaction among mean-flow advection, (large-scale) turbulent transport, and small-scale mixing. The larger velocity ratio results in stronger turbulent transport of the JPDF, but has opposite effects on the mean-flow advection for ϕ_1 (smaller) and ϕ_2 (larger). It causes decreased and increased mixing rate in the ϕ_1-ϕ_2 and ϕ_2-ϕ_3 mixing layers, respectively. The length scale ratio, on the other hand, delays the progression of the mixing process, but does not alter its qualitative characteristics. The peak location of the scalar JPDF is generally consistent with the mean scalar values, thus is dominated by the mean-flow advection. The shapes of the JPDF indicates that the mixing process is generally slower for Cases I and III. The JPDF for these cases is bimodal at some locations, with one peak having a low ϕ_1 value representing a mixture of ϕ_2 and ϕ_3, which results from the strong shear between these two streams, and the other peak consisting of mostly ϕ_1. The bimodality is due to the poor mixing between ϕ_1 and the ϕ_2-ϕ_3 mixture, a result of the lack of mean shear between the ϕ_1-ϕ_2 streams, and the large-scale turbulent transport (flapping) due to the strong shear between the annular stream and the co-flow. The JPDF is unimodal for cases II and IV, however, indicating that having shear layers on both sides speeds up the mixing process.

The conditional diffusion streamlines in scalar space representing the diffusion velocity generally converge quickly to a manifold, and then continue on the manifold at a lower rate. The fast approach to the manifold is due to local events (small-scale turbulent fluctuations and the molecular diffusion) and the slow process is related to large-scale velocity fluctuations. The streamline patterns have significant differences for the different velocity ratios. The main differences are the curvature of the diffusion

manifold and the location of the manifold in the ϕ_2 direction. For the cases with the larger velocity ratio (I and III), the curvature of the manifold is larger with the mean composition further from it, consistent with the slower progress of the mixing process, since mixing reduces the curvature, eventually leading to a straight-line manifold with the mean composition on it. While the existence of the manifold is a result of the flow configuration of the coaxial jet itself, the different velocity ratios alter the large-scale turbulent motions and small-scale mixing, resulting in different curvatures and location of the manifold.

The results in the present study have implications for turbulent reactive flows and mixing models. Varying the velocity ratio alters the location of the peak $\langle\phi_2\rangle$ value relative to the mean shear, which is analogous to shifting the location of the product, and hence the stoichiometric mixture fraction in a reactive flow. Thus, the results suggest that from the three-scalar mixing point of view, increasing the stoichiometric mixture fraction tends to reduce the mean values of the fuel and product. The bimodal JPDF for the higher velocity ratio cases suggests that such flows are more conducive to flamelets, since there is a large jump in the ϕ_1 value over a relatively thin layer. The mixing path along the manifold for the conditional diffusion presents a challenge for mixing models, which need to predict its shape as well as the dependence of its curvature on the velocity ratio and the annulus width.

The fundamental characteristics of SGS mixing and its dependence on the mean shear and scalar initial length scale were also investigated in detail, using the conditional means of the scalar FJDF and the conditionally filtered scalar diffusion, dissipation, and cross-dissipation. The filtered scalar and the SGS scalar variance of ϕ_1 are used as the conditioning variables. The results show that similar to SGS mixing in the fully developed turbulent scalar fields, there are also two SGS mixing regimes for the three-scalar mixing in turbulent coaxial jets. For small SGS variance

the scalars are well mixed. The FJDF is unimodal and the diffusion streamlines representing the conditionally filtered diffusion approach a stagnation point directly. The conditionally filtered scalar dissipation and cross-dissipation rates are low and their variations are small.

For large SGS variance, the scalars are highly segregated and the scalar structure (mixing configuration) in both scalar space and physical space is similar to the initial scalar structure (configuration), in contrast to the small SGS variance for which the three-scalar mixing configuration is lost. The FJDF is bimodal near the peak location of the mean SGS variance of ϕ_1 for all cases. The bimodal FJDF is a result of two competing effects, the SGS variance and the scalar length scale. For the higher velocity ratio cases a larger SGS variance in the neighborhood of the peak mean SGS variance causes stronger bimodality, while for the smaller velocity ratio cases the smaller scalar length scale and the wider mean SGS variance profile cause bimodal FJDF over a wider range of physical locations. The diffusion streamlines first converge to a manifold in the scalar space and continue on it toward a stagnation point. The manifold provides a mixing path for the center jet scalar and the co-flow air. The curvature of the diffusion manifold is larger for higher velocity ratio cases. The conditionally filtered scalar dissipation rates and cross-dissipation rate are consistent with those produced by the large SGS scalar structures. They also reveal several SGS mixing scenarios in which the largest SGS scales of the velocity field are likely to play a key role. These SGS mixing characteristics present a challenging test for SGS mixing models. The scalar dissipation rate structures for ϕ_1 and ϕ_2 have similarities to those of mixture fraction and temperature in turbulent nonpremixed/partially premixed flames. The results in the present work, therefore, also provide a basis for investigating multiscalar SGS mixing in turbulent flames.

The FJDF studied has relevance to a new LES approach proposed by Fox [16]

and systematically developed by Pope [44]. The approach is based on self-conditioned fields, e.g. the scalar PDF conditioned on a reduced representation of the scalar fields obtainable from the self-conditioned PDF. A scalar FJDF conditioned on the same conditioning variables can be obtained by filtering (averaged over the filter width for a top hat filter) self-conditioned JPDF. The FJDF in the present study is obtained using the filtered scalar and the SGS scalar variance at a point in physical space as the conditioning variables, which are a subset of the filtered scalar field and the SGS scalar variance field. The FJDF, therefore, is the filtered self-conditioned JPDF (or the self-conditioned JPDF solved on a grid size equal to the filter width) with conditions at a single point. Thus, the investigations of the FJDF in the present study provides a basis for studying the self-conditioned JPDF.

Bibliography

[1] M. Antonopoulos-Domis. Large-eddy simulation of a passive scalar in isotropic turbulence. *J. Fluid Mech.*, 104:55–79, 1981.

[2] Cody J.. Brownell and Lester K. Su. Measurements of multiple mole fraction fields in a turbulent jet by simultaneous planar laser-induced fluorescence and planar rayleigh scattering. *Measurement science and technology*, 22:15, 2011.

[3] R.A. Bryant, J.M. Donbar, and J. F. Driscoll. Acetone laser induced fluorescence for low pressure low temperature flow visualization. *Experiments in Fluids*, 28:471–476, 2000.

[4] J. Cai, R. S. Barlow, and C. Karpetis, A. N.and Tong. Conditionally filtered diffusion of mixture fraction and temperature in turbulent partially premixed flames. *Proc. Combust. Inst.*, 33:1505–1513, 2011.

[5] J. Cai, R.S. Barlow, A.N. Karpetis, and C Tong. Noise correction and length scale estimation for scalar dissipation rate measurements in turbulent partially premixed flames. *Flow, Turbulence and Combustion.*, 85:309–332, 2010.

[6] J. Cai, J. M. Dinger, W. Li, D.C. Carter, D. M. Ryan, and C. Tong. Experimental study of three-scalar mixing in a turbulent coaxial jet. *J. Fluid Mech.*, 685:495–531, 2011.

[7] J. Cai and C. Tong. A conditional-sampling-based method for noise and resolution corrections for scalar dissipation rate measurements. *Phys. Fluids*, 21:065104, 2009.

[8] J. Cai, D. Wang, C. Tong, R. S. Barlow, and A. N. Karpetis. Investigation of subgrid-scale mixing of mixture fraction and temperature in turbulent partially premixed flames. *Proc. Combust. Inst.*, 32:1517–1525, 2009.

[9] Jian. Cai. *Investigation of subgrid-scale mixing and turbulence-chemistry interaction in turbulent partially premixed flames using experimental data*. Ph.D. dissertation, Clemson University, Department of Mechanical Engineering, August 2010.

[10] C. M. Cha, S. M. de Bruyn Kops, and M. Mortensen. Direct numerical simulations of the double scalar mixing layer. part i: Passive scalar mixing and dissipation. *Phys. Fluids*, 18:067106, 2006.

[11] Noel T. Clemens. *Flow Imaging*. Encyclopedia of Imaging Science and Technology, 2002.

[12] P. J. Colucci, F. A. Jaberi, P. Givi, and S. B. Pope. Filtered density function for large eddy simulation of turbulent reacting flows. *Phys. Fluids*, 10:499–515, 1998.

[13] John W. Daily. Laser induced fluorescence spectroscopy in flames. *Prog. Eng. Combust. Sci.*, 23:133, 1997.

[14] Alan C. Eckbreth. *Laser Diagnostics for Combustion Temperature and Species*. Taylor & Francis, New York, NY, 1996.

[15] V. Eswaran and S. B. Pope. Direct numerical simulations of the turbulent mixing of a passive scalar. *Phys. Fluids*, 31(3):506–520, 1988.

[16] R.O. Fox. *Computational Models for Turbulent Reactive Flows*. Cambridge University press, Cambridge, England, 2003.

[17] F. Gao. An analytical solution for the scalar probabilty density-function in homogeneous turbulence. *Phys. Fluids A*, 3:511–513, 1991.

[18] L. Y. M. Gicquel, P. Givi, F. A. Jaberi, and S. B. Pope. Velocity filtered density function for large eddy simulation of turbulent flows. *Phys. Fluids*, 14:1196–1213, 2002.

[19] P. Hall. Using the bootstrap to estimate mean squared error and select smoothing parameter in nonparametric problems. *Journal of Multivariate Analysis*, 32:177–203, 1990.

[20] M. Holzer and E. D. Siggia. Turbulent mixing of a passive scalar. *Phys. Fluids*, 6:1820–1837, 1994.

[21] F. A. Jaberi, P. J. Colucci, S. James, P. Givi, and S. B. Pope. Filtered mass density function for large eddy simulation of turbulent reacting flows. *J. Fluid Mech.*, 401:85–121, 1999.

[22] F. A. Jaberi, R. S. Miller, and P. Givi. Conditional statistics in turbulent scalar mixing and reaction. *AIChE J.*, 42:1149–1152, 1996.

[23] Jayesh and Z. Warhaft. Probability-distribution of a passive scalar in grid-generated turbulence. *Phys. Rev. Lett.*, 67:3503–3506, 1991.

[24] Jayesh and Z. Warhaft. Probability distribution, conditional dissipation, and transport of passive temperature fluctuations in grid-generated turbulence. *Phys. Fluids A*, 4:2292–2307, 1992.

[25] A. Juneja and S. B. Pope. A dns study of turbulent mixing of two passive scalars. *Phys. Fluids*, 8:2161–2184, 1996.

[26] P. Kailasnath, K. R. Sreenivasan, and J. R. Saylor. Conditional scalar dissipation rates in turbulent wakes, jets, and boundary layers. *Phys. Fluids*, 5:3207–3215, 1993.

[27] C. K. Law. *Combustion Physics*. Cambridge University Press, New York, NY, 2006.

[28] A. D. Leonard and J. C. Hill. Scalar dissipation and mixing in turbulent reacting flows. *Phys. Fluids A*, 3:1286–1299, 1991.

[29] S. Liu and C. Tong. Subgrid-scale mixing of mixture fraction, temperature, and species mass fractions in turbulent partially premixed flames. *Proc. Combust. Inst.*, 34:12311239, 2013.

[30] A. Lozano. *Laser-excited luminescent tracers for planar concentration measurements in gasous jets*. Ph.D. dissertation, Stanford University, Department of Mechanical Engineering, August 1992.

[31] B. Ma and Z. Warhaft. Some aspects of the thermal mixing layer in grid turbulence. *Phys. Fluids*, 29:3114–3120, 1986.

[32] A. R. Masri, R. W. Dibble, and R. S. Barlow. The structure of turbulent nonpremixed flames revealed by raman-rayleigh-lif measurements,. *Prog. Eng. Combust. Sci.*, 22:307, 1996.

[33] J. Mi, R. A. Antonia, and F. Anselmet. Joint statistics between temperature and its dissipation rate components in a round jet. *Phys. Fluids*, 7:1665–1673, 1995.

[34] Richard B. Miles, Walter R. Lempert, and Joseph N. Forkey. Laser rayleigh scattering. *Measurement science and technology*, 12:33, 2001.

[35] R. S. Miller, S. H. Frankel, C. K. Madnia, and P. Givi. Johnson-edgeworth translation for probability modeling of binary mixing in turbulent flows. *Combust. Sci. Tech.*, 91:21–52, 1993.

[36] E. E. O'Brien and T. L. Jiang. The conditional dissipation rate of an initially binary scalar in homogeneous turbulence. *Phys. Fluids A*, 3:3121–3123, 1991.

[37] M. R. Overholt and S. B. Pope. Direct numerical simulation of a passive scalar with imposed mean gradient in isotropic turbulence. *Phys. Fluids*, 8:3128–3148, 1996.

[38] N. R. Panchapakesan and J. L. Lumley. Turbulence measurements in axisymmetric jet of air and helium. part 2. helium jet. *J. Fluid Mech.*, 246:225–247, 1993.

[39] N. Peters. Laminar diffusion flamelet models in non-premixed turbulent combustion. *Prog. Eng. Combust. Sci.*, 10:319–339, 1984.

[40] N. Peters. *Turbulent Combustion*. Cambridge University press, Cambridge, England, 2000.

[41] S. B. Pope. Pdf methods for turbulent reacting flows. *Prog. Eng. Combust. Sci*, 11:119–192, 1985.

[42] S. B. Pope. *Turbulent Flows*. Cambridge University press, Cambridge, England, 2000.

[43] S. B. Pope and E. Ching. Stationary probability density function in turbulence. *Phys. Fluids A*, 5:1529–1531, 1993.

[44] S.B. Pope. Self-conditioned fields for large-eddy simulations of turbulent flows. *J. Fluid Mech.*, 652:139–169, 2010.

[45] Stephen. B. Pope. Simple models of turbulent flows. *Physics of fluids.*, 23:011301, 2011.

[46] J.M. Prausnitz, B.E. Poling, and J.P. O'Connell. *The Properties of Gases and Liquids*. McGraw Hill, Boston, Massachusetts, 2001.

[47] A. G. Rajagopalan and C. Tong. Experimental investigation of scalar-scalar-dissipation filtered joint density function and its transport equation. *Phys. Fluids*, 15:227–244, 2003.

[48] V. Raman, H. Pitsch, and O. R. Fox. Hybrid large-eddy simulation/lagrangian filtered-density-function approach for simulating turbulent combustion. *Combust. Flame*, 143:56–78, 2005.

[49] R.C. Reid, J.M. Prausnitz, and B.E. Poling. *The Properties of Gases and Liquids*. McGraw Hill, Boston, Massachusetts, 1989.

[50] D. H. Rowinski and S. B. Pope. An investigation of mixing in a three-stream turbulent jet. *Phys. Fluids*, 25:105105, 2013.

[51] D. Ruppert. Empirical-bias bandwidths for local polynomial nonparametric regression and density estimatio. *J.Amer. Statist. Assoc.*, 92:1049–1062, 1997.

[52] V. A. Sabel'nikov. Asymptotic solution of the equation for the probability distribution of a passive scalar in grid turbulence with a uniform mean scalar gradient. *Phys. Fluids*, 10:743–755, 1998.

[53] A. Sahay and E. E. O'Brien. Uniform mean scalar gradient in grid turbulence: Conditioned dissipation and production. *Phys. Fluids A*, 5:1076–1078, 1993.

[54] M. R. H. Sheikhi, T. G. Drozda, P. Givi, and S. B. Pope. Velocity-scalar filtered density function for large eddy simulation of turbulent flows. *Phys. Fluids*, 15:2321–2337, 2003.

[55] M.R.H. Sheikhi, T.G. Drozda, P. Givi., F.A. Jaberi, and S.B. Pope. Large eddy simulation of a turbulent nonpremixed piloted methane jet flame (sandia flame d). *Proc. Combust. Inst.*, 30:549–556, 2005.

[56] D. A. Shetty, A.J. Chandy, and S.H. Frankel. A new fractal interaction by exchange with the mean mixing model for large eddy simulation/filtered mass density function applied to a multiscalar three-stream turbulent jet. *Phys. Fluids*, 22:025102, 2010.

[57] Y. G. Sinai and V. Yahkot. Limiting probability distribution of a passive scalar in a random velocity field. *Phys. Rev. lett.*, 63:1962–1964, 1989.

[58] A. Sirivat and Z. Warhaft. The mixing of passive helium and temperature fluctuations in grid turbulence. *J. Fluid Mech.*, 120:475–504, 1982.

[59] K. R. Sreenivasan, S. Tavoularis, R. Henry, and S. Corrsin. Temperature fluctuations and scales in grid-generated turbulence. *J. Fluid Mech.*, 100:597–621, 1980.

[60] A. M. K. P. Taylor. *Instrumentation for flows with combustion.* Academic Press, 1993.

[61] H. Tennekes and J. L. Lumley. *A First Course in Turbulence.* MIT press, Cambridge, MA, 1972.

[62] Mark C. Thurber. *Acetone Laser-Induced Fluorescence for Temperature and Multiparameter Imaging in Gaseous Flows.* Ph.D. dissertation, Stanford University, Department of Mechanical Engineering, March 1999.

[63] C. Tong. Measurements of conserved scalar filtered density function in a turbulent jet. *Phys. Fluids*, 13:2923–2937, 2001.

[64] C. Tong and Z. Warhaft. On passive scalar derivative statistics in grid turbulence. *Phys. Fluids*, 6:2165–2176, 1994.

[65] C. Tong and Z. Warhaft. Passive scalar dispersion and mixing in a turbulent jet. *J. Fluid Mech.*, 292:1–38, 1995.

[66] M. P. Wand and M. C. Jones. *Kernel Smoothing*. Chapman & Hall, 1995.

[67] D. Wang and C. Tong. Conditionally filtered scalar dissipation, scalar diffusion, and velocity in a turbulent jet. *Phys. Fluids*, 14:2170–2185, 2002.

[68] D. Wang and C. Tong. Experimental study of velocity-scalar filtered joint density function for les of turbulent combustion. *Proc. Combust. Inst.*, 30:567–574, 2005.

[69] D. Wang, C. Tong, R. S. Barlow, and A. N. Karpetis. Experimental study of scalar filtered mass density function in turbulent partially premixed flames. *Proc. Combust. Inst.*, 31:1533–1541, 2007.

[70] G. H. Wang and N. T. Clemens. Effects of imaging system blur on measurements of flow scalars and scalar gradients. *Exp. Fluids*, 37:194–205, 2004.

[71] G.-H. Wang, N. T. Clemens, R. S. Barlow, and P. L. Varghese. A system model for assessing scalar dissipation measurement accuracy in turbulent flows. *Meas. Sci. Tech.*, 18:1287–1303, 2007.

[72] Z. Warhaft. The use of dual heat injection to infer scalar covariance decay in grid turbulence. *J. Fluid Mech.*, 104:93–109, 1981.

[73] Z. Warhaft. The interference of thermal fields from line sources in grid turbulence. *J. Fluid Mech.*, 144:363–387, 1984.

[74] Z. Warhaft and J. L. Lumley. An experimental study of the decay of temperature fluctuations in grid-generated tubulence. *J. Fluid Mech.*, 88:659–684, 1978.

[75] P. K. Yeung. Correlations and conditional statistics in differential diffusion: Scalars with uniform mean gradients. *Phys. Fluids*, 10:2621–2635, 1998.